Low-dimensional van der Waals Material Based Electronics and Optoelectronics

By

Tianjiao Wang

Dissertation Submitted to the Faculty of the

Graduate School of Vanderbilt University

in partial fulfillment of the requirements

for the degree of

DOCTOR OF PHILOSOPHY

In

Electrical Engineering

October 31, 2020

Nashville, Tennessee

To be approved:

Yaqiong Xu, Ph.D.

Daniel M. Fleetwood, Ph.D.

Ronald D. Schrimpf, Ph.D.

Sharon M. Weiss, Ph.D.

Deyu Li, Ph.D.

To my beloved mom and dad

ACKNOWLEDGEMENTS

First and foremost, I would like to express my deepest gratitude to my advisor Professor Dr. Yaqiong Xu. I feel so fortunate to work under her guidance throughout the past years. She impressed me with her sharp instinct, critical thinking and unlimited creativity. I really enjoy every discussion with her and she is always patient in listening to all my experiment details, continuously offers insightful, constructive suggestions and constantly motivates me with brilliant new ideas. I learned a lot from her, not only the skills in dealing with the research difficulties, but also the altitudes when I face failure and feel lost. My Ph.D. project cannot be completed without the support from her.

I also feel deeply grateful to my Ph.D. dissertation committee: Dr. Daniel Fleetwood, Dr. Deyu Li, Dr. Ronald Schrimpf and Dr. Sharon Weiss for their time, support and suggestions taking time regarding my research, dissertation and career path.

I would like to give many thanks to my lab mates, past and present. I appreciate all help and suggestions from them and treasure the times we spent together and the sweet memories we shared. I specifically would like to thank Dr. Hong Tu, who mentored me when I was a novice and confused about research. Dr. Rui Wang, who provided me with plenty of help during my graduate study. Xuyang Ge, Yuchen Zhang, Xuyi Luo, Thayer Walmsley, Ornelas Christian and Xiaosi Zhang, who offer me friendly assistance and care.

I would like to thank all collaborators. First, I owe special thanks to Dr. Zhixian Zhou, Dr. Bhim Chamlagain and Kraig Andrews, Arthur Bowman from Wayne State University for our collaborated project of high performance two-dimensional (2D) material based devices. Also, I would like to express thanks to Dr. Sharon Weiss, Dr. Shuren Hu, Vijayashree Parsi Sreenivas and

Tengfei Cao who work with me on the waveguide integrated 2D material based devices and offer me advice about photonic crystals. Then I would like to thanks Dr. Qi Zhang, Dr. Kristina Kitko and Dr. Mingjian Shi for helping me with the biological related researches. Next, I would like to thank Dr. Enxia Zhang, Dr. Rong Jiang and Dr. Pan Wang for radiation effect measurements. Also, I would like to give thanks to Dr. Deyu Li, Dr. Qian Zhang, Dr. Lin Yang, Yang Zhao and Zhiliang Pan for thermal related experiments for nanowires. Finally, I would like to thanks Dr. Zhiqiang Mao and Yanglin Zhu from Pennsylvania State University for providing nanowire materials.

I would like to thank staff members of Vanderbilt Institute of Nanoscale Science and Engineering (VINSE): Dr. Kurt Heinrich, Dr. Anthony Hmelo, Dr. Bo Choi, Dr. Ben Schmidt, Dr. Dmitry Koktysh, Dr. Alice Leach and Dr. William Martinez for training and supporting me to use VINSE facilities. I would also like to thank the staff members of the Center for Nanophase Materials Sciences (CNMS) at Oak Ridge National Laboratory, especially our host Dr. Ivan Kravchenko, as well as staff members at the Cornell NanoScale Science Technology Facility (CNF).

I would like to thank all my friends at Vanderbilt, Wenyi Wang, Wei Li, Zhihua Zhu, Huiqi Gong, Mengya Li and Hangfang Zhang, who also offer me many helps for research and support me in difficult times.

Last but not least, I would like to give great thanks to my parents, for their love, understanding, encouragement, and most importantly, eternal support during my long, challenging graduate study.

TABLE OF CONTENTS

Page

ACKNOWLEDGEMENTS iii

TABLE OF CONTENTS v

LIST OF FIGURES viii

LIST OF TABLES x

LIST OF PUBLICATIONS xi

Chapter 1 Introduction to Low-dimensional van der Waals Materials 1

1.1 Low-dimensional Van der Waals materials 1
1.2 Low-dimensional vdW material based optoelectronics 5
1.3 Heterostructures built from vdW materials 7
1.4 Low-dimensional vdW materials for photodetection 8
Photodetector structures 8
Photodetection mechanisms 10
Photodetectors figure-of-merit 13
1.5 Scanning photocurrent microscopy 15

Chapter 2 High Performance WSe_2 Photodetectors with 2D/2D Ohmic Contacts 18

2.1 Ohmic contacts 18
2.2 Engineering MS contacts for TMDC based phototransistor 20
2.3 WSe_2 phototransistor with 2D/2D Ohmic Contact 20
2.4 Scanning photocurrent mapping and response spectrum 23
2.5 Bias-dependent scanning photocurrent mapping 25
2.6 Photodetection performances 26
2.7 Photoresponse dynamics 28
2.8 Photocurrent generation mechanisms 29
2.9 Conclusion 32
2.10 Methods 32

Materials Synthesis 32
Chapter 3 Visualizing Light Scattering in Silicon Waveguides with Few-layer BP Photodetectors 34
3.1 Black phosphorus 34
3.2 Photonic structure - low dimensional material optoelectronics system 35
Modulator 35
Photodetector 38
3.3 Visualizing light scattering in silicon waveguides with BP photodetectors 39
3.4 Polarization-dependent photocurrent mapping 41
3.5 Wavelength-dependent photocurrent mapping 43
3.6 Photocurrent generation mechanism 45
3.7 Conclusion 47
3.8 Methods 48
Device Fabrication 48
FDTD Simulations 48
Chapter 4 Tunneling Effect between Crossed van der Waals $Ta_2Pt_3Se_8$ and $Ta_2Pd_3Se_8$ Nanoribbon Junctions 50
4.1 $Ta_2Pt_3Se_8$ and $Ta_2Pd_3Se_8$ 50
4.2 Low-dimensional material transfer methods 52
4.3 *p-n* junction between $Ta_2Pt_3Se_8$ and $Ta_2Pd_3Se_8$ nanoribbons 56
4.4 Tunneling effect 58
4.5 Polarization-dependent photoresponse 60
4.6 Bias-dependent photoresponse 62
4.7 Photoresponse spectrum for nanowire with various thickness 63
4.8 Conclusion 64
Chapter 5 Laser Induced Charge Density Wave Melting in Suspended $NbSe_3$ Nanowires 66
5.1 Charge density wave in $NbSe_3$ 66
5.2 Raman spectrum and resistance characteristics of $NbSe_3$ 66
5.3 Anisotropic photocurrent along the nanowire 68
5.4 Laser induced CDW melting 69
Chapter 6 Summary and outlook 74

6.1 Summary 74
6.2 Challenges and Outlook 75
2D photonic crystal integrated 2D material based photodetectors 75
SWNT based detection platform for DNA 77
APPENDIX Instructions for Transfer 81
SiO_2/Si chip preparation 81
Metal electrode fabrication and release 81
Pick up and transfer 81
Window opening 82
References 83

LIST OF FIGURES

Page

Figure 1.1 Lattice structures and band structures of 2D vdW materials: Monolayer and bilayer graphene, hBN and TMDs. 3

Figure 1.2 Layered and chain-like lattice structures for the TMTCs. 4

Figure 1.3 Electromagnetic spectrum and optoelectrical applications of 2D vdW materials. 6

Figure 1.4 VdW heterostructures built from low-dimensional materials: 0D quantum dots nanoparticle, 1D nanowires, 1.5D nanoribbons and 3D bulk materials. 7

Figure 1.5 Photodetector structures: photodiode and photoconductor. 9

Figure 1.6 Schematic representation of photocurrent-generation mechanisms in semiconducting 2D materials: PVE, PTE, PBE and hot electron injection. 11

Figure 1.7 Overview of performance metrics of standard and low-dimensional material based photodetector technologies. 15

Figure 1.8 Scanning photocurrent microscopy: schematic layout and scanning photocurrent mapping of a SWNT. 16

Figure 2.1 MS contacts: Schottky contacts versus ohmic contacts. 19

Figure 2.2 Structure and electronic characteristics of WSe_2 phototransistors with 2D/2D ohmic contact. 22

Figure 2.3 Scanning photocurrent mapping and wavelength dependent photoresponse. 23

Figure 2.4 Electronic and optoelectronic characteristics for a typical WSe_2 phototransistor with degenerately p-doped MoS_2 as source/drain contacts. 24

Figure 2.5 Bias dependent scanning photocurrent mapping. 26

Figure 2.6 Photoresponse as a function of source-drain bias voltage under various back-gate voltages and at various values of the optical power intensities. 27

Figure 2.7 Experimental setup for photoresponse dynamics and ultrafast photorsponse. 29

Figure 2.8 Gate-dependence photoresponse and photocurrent generation mechanisms. 31

Figure 3.1 Crystal lattice and layer-depended bandgap of BP. 34

Figure 3.2 Photonic structure - low dimensional material electronics/optoelectronics hybrid system as modulator and photodetector. 37

Figure 3.3 Photonic silicon waveguide integrated BP photodetector. 41

Figure 3.4 Polarization-dependent scanning photocurrent mappings and corresponding FDTD simulations. 42

Figure 3.5 Wavelength-dependent scanning photocurrent mappings and corresponding FDTD simulations. 44

Figure 3.6 Photocurrent generation mechanisms: electron/hole injection from silicon to BP. ... 46

Figure 4.1 TPdS: crystal structure, SEM and AFM images. 51

Figure 4.2 Low dimensional material transfer methords. 53

Figure 4.3 Comparasion between transferred metals and evaporated metals. 55

Figure 4.4 Schematic and electronic characteristics of the TPtS-TPdS junction. 57

Figure 4.5 polarization-dependent photoresponse of the TPtS-TPdS junction. 61

Figure 4.6 Bias-dependent photocurrent of the TPtS-TPdS junction. 62

Figure 4.7 Photoresponse spectrum for nanowire with various thickness. 64

Figure 5.1 Crystal structure, Raman spectrum, and resistance characteristics of $NbSe_3$. 67

Figure 5.2 Anisotropic photocurrent of the $NbSe_3$ nanowire. 68

Figure 5.3 Temperature-dependent photoconductivity and photovoltage of the $NbSe_3$ nanowire. 70

Figure 5.4 Photoexcitation processes. 71

Figure 6.1 Absorption spectrum of a 2D photonic crystal with bowtie unit cell. 76

Figure 6.2 Schematic of a SWNT transistor combined with dual-trap optical tweezers. 78

Figure 6.3 Overstretching dsDNA to dsDNA-ssDNA hybrid to ssDNA. 79

LIST OF TABLES

Page

Table 1.1 Photodetectors figure-of-merit 14

Table 3.1 Photonic structure integrated 2D material optoelectronics 36

LIST OF PUBLICATIONS

Portions of this dissertation have been drawn from the following publications and manuscripts:

1. **Tianjiao Wang** and Ya-Qiong Xu, "Photonic Structure Integrated Two-dimensional Material Optoelectronics," Electronics 5, 93 (2016)

2. **Tianjiao Wang**, Kraig Andrews, Arthur Bowman, Tu Hong, Michael Koehler, Jiaqiang Yan, David Mandrus, Zhixian Zhou, and Ya-Qiong Xu, "High Performance WSe_2 Phototransistors with 2D/2D Ohmic Contacts," Nano Letters 18, 2766 (2018)

3. **Tianjiao Wang**, Shuren Hu, Bhim Chamlagain, Tu Hong, Zhixian Zhou, Sharon M. Weiss, and Ya-Qiong Xu, "Visualizing Light Scattering in Silicon Waveguides with Black Phosphorous Photodetectors," Advanced Materials 28, 7162 (2016)

4. **Tianjiao Wang**, Yanglin Zhu, Zhiqiang Mao, and Ya-Qiong Xu, " Tunneling Effect between Crossed van der Waals $Ta_2Pt_3Se_8$ and $Ta_2Pd_3Se_8$ Nanoribbon Junctions," Manuscript ready to be submitted.

5. **Tianjiao Wang**, Zhiliang Pan, Zhiqiang Mao, Deyu Li and Ya-Qiong Xu, "Laser Induced Charge density wave Melting in Suspended $NbSe_3$ Nanowires," Manuscript under preparation.

Other publications that are related but not directly covered by this dissertation:

6. Tu Hong, **Tianjiao Wang**, and Ya-Qiong Xu, "Direct Measurement of π Coupling at the Single-Molecule Level using a Carbon Nanotube Force Sensor," Nano Letters 18, 7883 (2018)

7. Tu Hong, Bhim Chamlagain, **Tianjiao Wang**, Hsun-Jen Chuang, Zhixian Zhou, and Ya-Qiong Xu, "Anisotropic Photocurrent Response at Black Phosphorous-MoS_2 p-n Heterojunctions," Nanoscale 7, 18537 (2015)

8. Rui Wang, **Tianjiao Wang**, Tu Hong, and Ya-Qiong Xu, "Probing Photoresponse of Aligned Single-Walled Carbon Nanotube Doped Ultrathin MoS_2," Nanotechnology 29, 345205 (2018)

9. Xuyi Luo, Kraig Andrews, **Tianjiao Wang**, Arthur Bowman, Zhixian Zhou, and Ya-Qiong Xu, "Reversible photo-induced doping in WSe_2 Field effect transistors," Nanoscale 11, 7358 (2019)

10. Thayer S. Walmsley, Kraig Andrews, **Tianjiao Wang**, Upendra Rijal, Arthur Bowman, Amanda Haglund, David Mandrus, Zhixian Zhou, and Ya-Qiong Xu, "Near-infrared optical transitions in $PdSe_2$ phototransistors," Nanoscale 11, 14410 (2019)

Chapter 1 Introduction to Low-dimensional van der Waals Materials

1.1 Low-dimensional Van der Waals materials

Van der Waals (vdW) material (layered materials) are characterized by extended crystalline planar structures held together by strong in-plane covalent bonds and weak out-of-plane vdW forces. The vdW bonds can be easily broken with little damage to the in-plane layer, offering the possibility to obtain high-quality films or ribbons with thickness down to the nanometer scale. The first demonstration is graphene, a stable, single-atom layer, honeycomb carbon, which was exfoliated from the bulk graphite with adhesive tape by two researchers Geim and Novoselov at The University of Manchester in 2014.[1] This mechanical exfoliated method was then widely used to obtain nanometer-thin layers from other vdW materials. Compared with other methods, such as chemical vapor deposition (CVD), epitaxial growth and chemical exfoliation, mechanical exfoliation offers a cost-efficient, facile and versatile approach to achieve vdW thin films or thin ribbons with high quality and intrinsic properties.[2, 3] The great success of graphene inspires researchers to re-discover and re-examine other two-dimensional (2D) or one-dimensional (1D) vdW materials from their bulk crystals.

Graphene is the most widely learned 2D vdW material. 2D materials are substances with a thickness down to the nanometer scale. Since both charge and heat transport are restricted in the direction that perpendicular to the 2D plane, 2D materials have been predicted to possess many novel properties compared to their three-dimensional (3D) crystals. Over the last 15 years, graphene has been demonstrated to be one of the most attractive 2D vdW materials because of its unique band structure and exceptionally high carrier mobility. As shown in Figure 1.1a, the valence

and conduction bands of graphene meet in conical valleys at the Brillouin-zone corners, marked K and K', which is protected by the symmetry of its honeycomb lattice. This band structure allows the emergence of many fascinating electronic properties, such as a half-integer shift in the quantum Hall effect, Klein tunneling across an arbitrarily large potential barrier and nontrivial Berry phase.[4] Other fundamental studies of graphene yielded access to a large number of unique merits: the highest mechanical strength (Young's modulus of 1TPa),[5] outstanding thermal conductivity (> 3,000 $W \cdot m^{-1} \cdot K^{-1}$),[6] a quantized optical absorption coefficient (~ 2.3%)[7] and zero bandgap, enabling it to be a promising candidate for mechanical, thermal and optical applications. Especially, Graphene displays remarkable electron mobility at room temperature, with reported values in excess of 15,000 $cm^2 \cdot V^{-1} \cdot s^{-1}$,[1] showing great potential for high-speed transistor.[8] However, the large dark current that results from its gapless nature severely limits the overall performance. Great efforts have been paid to open a considerable and tunable bandgap in graphene at room temperature while retaining its outstanding properties, via chemical (change the pristine graphene lattice) or physical (keep the atomic structure intact and apply an external method). [9-11]

Compare to monolayer graphene, bilayer graphene (Figure 1.1b), where two graphene single-atom sheet stack together to form a staggered honeycomb lattice, the energy dispersion becomes parabolic but still meet at K and K' due to the inversion symmetry. To further lift the degeneracy, for example, in hexagonal boron nitride (hBN) (Figure 1.1c), the inversion is broken by replacing two carbon atoms in the graphene with boron and nitrogen, resulting in a large energy gap, presenting insulator properties.

Transition metal dichalcogenides (TMDs or TMDCs) are a particularly interesting and well-studied class of 2D vdW materials. TMDCs have a general chemical formula of MX_2, where M is a transition metal atom from group IV, V and VI (eg. Mo, W), and X is a chalcogen atom (eg.

S, Se, Te). The variety of elements and layer-dependence enable TMDCs to present a wide range of electrical and optical properties.[12, 13] Their semiconducting nature makes them great candidates for 2D electronics and optoelectronics with low off and dark current.[14-17] Furthermore, the broken in-plane inversion symmetry in monolayer gives rise to valley-dependent behaviors.[18, 19] In recent years, black phosphorus (BP) has occupied an important position in 2D vdW material fields. Its layer-dependent bandgap, anisotropic nature, high mobility and good light-matter interactions generated huge interests in the possible implementations of BP in a myriad of devices and make it a promising 2D vdW material beyond graphene and 2D TMDCs.[20-22]

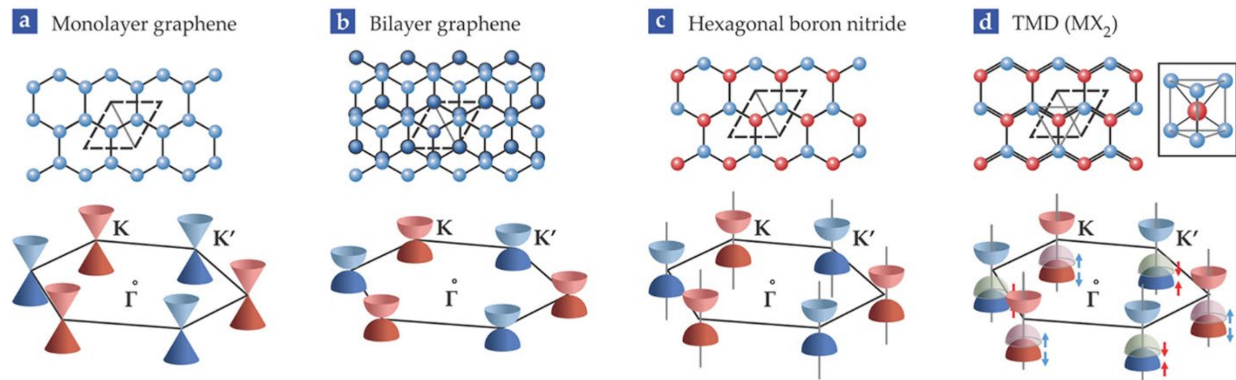

Figure 1.1 *Lattice structures and band structures of 2D vdW materials: Monolayer and bilayer graphene, hBN and TMDs.Lattice structures and band structures at the corners of the first Brillouin zone for (a) monolayer graphene, (b) bilayer graphene, (c) hexagonal boron nitride and (d) the TMDs. The dashed lines in the lattice diagrams indicate unit cells. The TMDs' valence band is split into two spin-polarized bands, marked by the red and blue arrows. Reproduced from ref. [23], with the permission of the American Institute of Physics.*

The extension of exfoliation from 2D vdW materials to 1D gives rise to 1D or quasi-1D vdW nanowires or nanoribbons. Similar to 2D vdW materials mentioned before, which layered structures are bonded by relatively weak inter-layer vdW forces, 1D vdW materials involves a chain-like structure that bonded by relatively weak inter-chain forces (can be weak covalent forces

or vdW forces), showing potential to be mechanically exfoliated to become nanowires or nanoribbons. Many 1D vdW materials have been reported in previous studies and one of the most well-known groups is the IV-V transition metal trichalcogenides (TMTCs). As shown in Figure 1.2a, the typical class of TMTCs, MX_3 are composed of transition metal atoms M (IVB group: Ti, Zr, Hf or VB group: Nb, Ta) and chalcogen atoms X (VIA group: S, Se, Te), which is the 1D counterpart to TMDCs. Take titanium trisulfide (TiS_3) for an example, the basic structure for these materials consists of covalently bonded layers, which are bonded through vdW forces (Figure 1.2b). For a single layer, MX_3 chains are covalently bonded within the a-b plane (Figure 1.2c), and the ends of chains are shown by the transmission electron microscopy (TEM) image (Figure 1.2d).

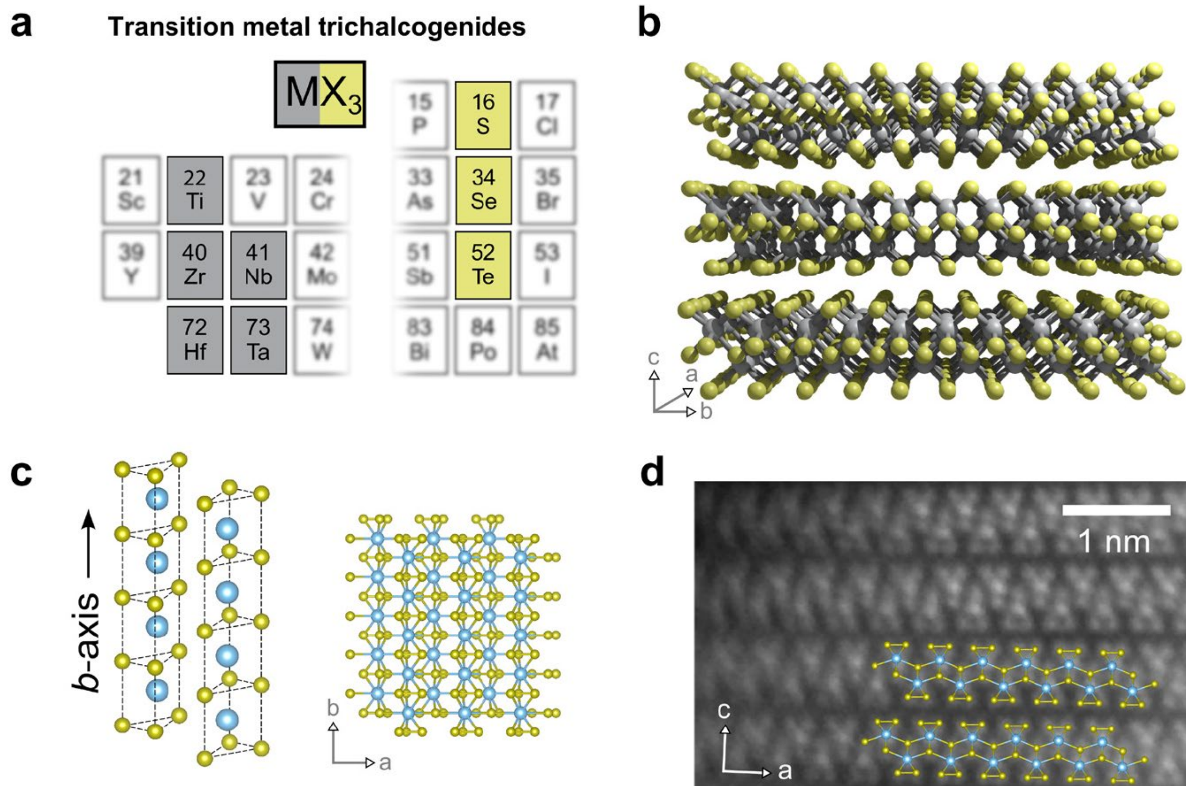

Figure 1.2 *Layered and chain-like lattice structures for the TMTCs.(a) Elements that make up the group IV-V TMTCs. (b) 3D model of the crystal structure of* TiS_3*. (c) b-axis chains that lead to the quasi-1D properties of the TMTCs. a-b plane of the crystal structure showing the covalent bonding of the b-axis chains in a single layer of* TiS_3*. (d) TEM of the cross-section of a* TiS_3 *sample showing the layered structure and the ends of the b-axis chains. Reproduced with permission from ref. [24], with the permission of the IOP Publishing.*

There are some other groups that can also be viewed as 1D vdW material, for example, the binary tetradymite M_2X_3 (M = Sb, Bi; X = S, Se), the ternary chalcogenides $M_2X_3Y_8$ (M = Ta, Nb; X = Ni, Pd, Pt; Y = S, Se) and more. The reduced in-plane structural symmetry can give those materials strong anisotropies in their electrical and optical properties. On the other hand, 1D vdW materials are expected to inherit some features from 2D ones, such as strong light-matter interactions, thickness-dependent energy bandgaps, and the capability of forming vdW heterostructures. Researchers have demonstrated 1D vdW materials' unique thermal, electrical and optical properties, including partially ballistic heat transport and high anisotropy ratios in conductivity and optical absorption/emission.[24-28] For example, partially ballistic phonon transport has been detected in suspended $Ta_2Pd_3Se_8$ (TPdS) nanoribbons that can persist over 13 μm along the chain-axis at room temperature. TiS_3 has been predicted to have electron mobility as high as 10,000 $cm^2 \cdot V^{-1} \cdot s^{-1}$ and has been demonstrated to own strong electrical and optical anisotropy.[29-32] Exceptionally high breakdown current density and low noise have been observed for zirconium tritelluride ($ZrTe_3$) and $TaSe_3$ nanoribbons.[33-35] Furthermore, the energy bandgaps of these materials range from 0.2 eV to 2 eV,[24] making them ideal candidates for high performance field-effect transistors (FETs) and broadband optoelectronics.

1.2 Low-dimensional vdW material based optoelectronics

Low-dimensional vdW materials present several advantages over conventional 3D materials for optoelectronics. First, although the innate thinness renders these materials almost transparent, their strong light-matter interactions enable decent single-pass absorption. For example, single-layer graphene absorbs 2.3% of vertically incident white light.[7] Monolayer molybdenum disulfide (MoS_2) absorbs around 10% at excitonic resonances.[36]

Moreover, low-dimensional vdW materials cover a wide response spectral range from microwave to ultraviolet wavelengths, allowing applications in multiple fields. Take 2D vdW material as an example, as shown in Figure 1.3, the zero bandgap makes graphene a potential candidate for optical applications over a broad spectral range.[37, 38] TMDCs possess relatively larger bandgaps, enabling excellent on/off ratio, but limiting their performance in telecom-wavelength.[12] BP has a layer-tunable direct bandgap ranging from 0.3 eV in bulk to 1.8-2.0 eV in monolayer,[22] which covers from visible to mid-infrared spectral regions.

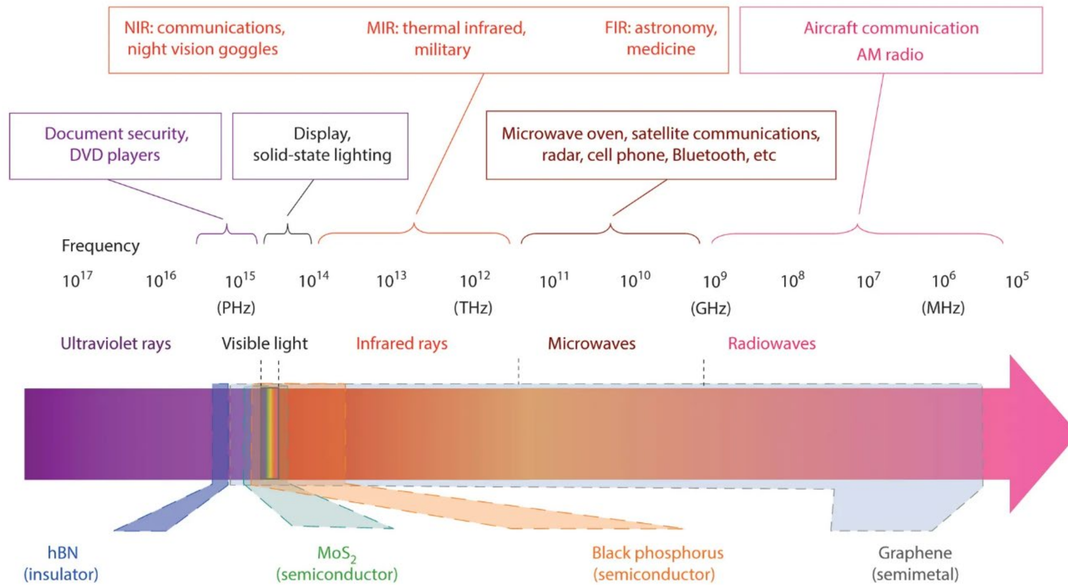

Figure 1.3 *Electromagnetic spectrum and optoelectrical applications of 2D vdW materials.Applications that utilize the different spectral ranges are presented in the top portion of the panel. NIR, MIR and FIR indicate near-, mid- and far-infrared, respectively. The possible spectral ranges covered by hBN, MoS_2, BP and Graphene are indicated using colored polygon at the bottom of the panel, respectively. Reproduced with permission from ref. [39], with the permission of the Springer Nature.*

Finally, the absence of dangling bonds makes low-dimensional vdW materials easy to be integrated with photonic structures or stacked together to form vdW heterostructures.[40] The large low-dimensional vdW materials family allows their heterostructures with a far greater

number of combinations, which make it possible to observe numerous exciting physical phenomena and to yields a range of possible applications.[41-43]

1.3 Heterostructures built from vdW materials

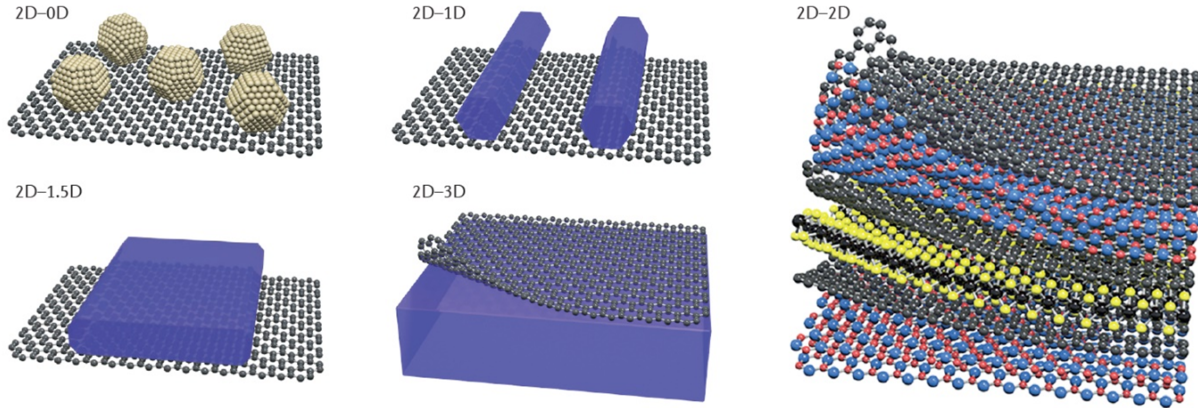

Figure 1.4 *VdW heterostructures built from low-dimensional materials: 0D quantum dots nanoparticle, 1D nanowires, 1.5D nanoribbons and 3D bulk materials.vdW heterostructures formed by integrating the dangling-bond-free 0D nanoparticles or quantum dots, 1D nanowires, 1.5D nanoribbons, 3D bulk materials and 2D nanosheets. Reproduced with permission from ref. [42] with permission from Springer Nature.*

As mentioned in the above discussions, vdW materials possess fully saturated chemical bonds on the surface, facilitate the integration of highly disparate atomic layers to create a wide range of vdW heterostructures without the constraints of lattice matching and processing compatibility. As illustrated in Figure 1.4, various heterostructures can be built by stacking different low dimensional semiconducting crystals on top of each other as the vdW force provide the interlayer bond.[42] Those heterostructures are expected to show the combined functionality of the individual layer and new phenomena at the interface. For example, A maximum photodetection responsivity of 418 mA/W at the wavelength of 633 nm has been achieved by stacking *p*-type BP with *n*-type MoS_2 to form ultrathin *PN* diodes.[44] The photocurrent signals at the *PN* junction dominate the photocurrent generation, which is much stronger than photoresponse

at the metal-semiconductor contacts due to the large band mismatch at the interface. The polarization direction of the photoresponse at the junction is affected by either BP or MoS_2 channel, depending on the illumination conditions.[45] Moreover, 2D vdW material based heterostructures allow the possibility to obtain high-quality devices by encapsulating a 2D vdW material thin film with 2D vdW insulators such as hBN sheets to form a sandwich-like structure. The hBN sheets provide an ultra-smooth surface for the inner graphene film and protect the graphene film from direct exposure to air or contact with substrates. These devices exhibit room-temperature mobility up to 140,000 $cm^2 \cdot V^{-1} \cdot s^{-1}$ which is near the theoretical phonon-scattering limit.[46, 47]

1.4 Low-dimensional vdW materials for photodetection

Photodetectors, which transduce optical signals into electrical signals are one of the key components in various optoelectronic devices. Photodetectors with different spectral selectivity, speed, response spectra and sensitivity are required for a large diversity of applications in our daily life. The introduce of novel low-dimensional materials to the photodetecting system is one accessible and promising solution to overcome the existing limitation in traditional photodetectors based on silicon and III-V materials. Over the past decades, 2D vdW materials such as: Graphene, TMDCs, BP and their hybrid systems all have been demonstrated to exhibit outstanding performances for photodetection.[48-52] 1D vdW materials have also attracted a lot of attentions due to their outstanding performances, especially for the anisotropic photodetection and photodetection where wire-like geometry is pursued.

Photodetector structures

Photodiodes and photoconductors are two classic photodetectors types (Figure 1.4), where the former typically form a *PN* or *PIN* junction between semiconductors of oppositely doping. The

built-in electric field at the junction drives the separation of photo-excited electron-hole pairs (EHPs) and therefore allows photodetection.

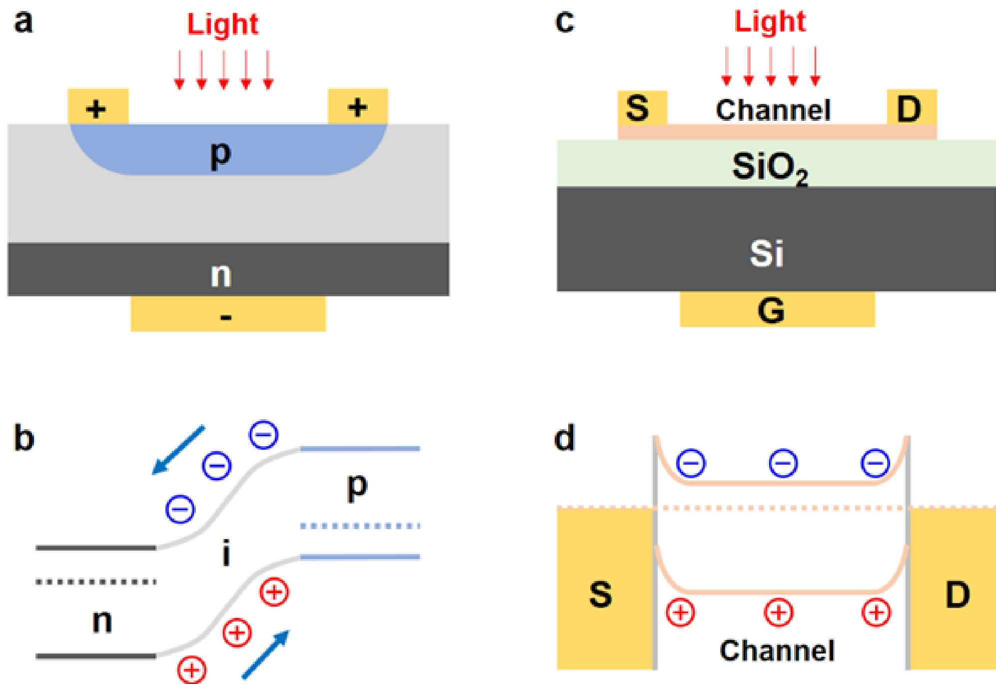

Figure 1.5 *Photodetector structures: photodiode and photoconductor.Schematic for (a) photodiode and (c) photoconductor. Band diagram for (b) photodiode and (d) photoconductor. + and – indicate cathode and anode. p, n and i indicate p-type, n-type and instinct semiconducting materials. S, D and G indicate source, drain and gate contacts.*

The photoconductor structure usually consists of a semiconductor channel with two metal contacts, namely a metal-semiconductor-metal (MSM) lateral structure. Here, photo-excited EHPs are separated by the external bias applied, and thus add an extra photoconductance to the devices. The most common structure of low-dimensional material-based photodetectors consists a MSM lateral structure and a gate electrode isolated from the channel by a thin dielectric film to control the electrical behaviors of the channel material, which is similar to the structure of the traditional FET. This photodetector architecture provides great advantages for semiconducting 2D materials

like TMDCs, where their moderately large direct bandgaps allow efficient field-effect modulation, and thus ultralow dark current can be achieved by fully depleting the thin TMDC channel.

Photodetection mechanisms

Generally, the photodetection of a low-dimensional material-based device can be attributed to more than one mechanism especially for the photoconductor structure-based photodetector, considering various bias/gate voltage applied and light illumination conditions. In order to have an in-depth understanding of low-dimensional material based photodetectors, it is necessary to first know the several widely studied physical mechanisms for photodetection. Figure 1.6 summarizes those mechanisms (take 2D material based photodetectors for example), which include photovoltaic effect (PVE), photo-thermoelectric effect (PTE), photo-bolometric effect (PBE), and hot electron injection.

At metal-semiconductor Schottky barriers or *PN* junctions, the Fermi level alignment led to build-in electric fields and thus force the photo-excited EHPs to be separated. This phenomenon is known as PVE, which has been elaborated in traditional 3D semiconductor device.[53, 54] Here we note that photocurrent is defined to be $\Delta I_{pc} = I_{ds,illumination} - I_{ds,dark}$. As shown in Figure 1.6a, when the photon energy of the light is larger than the bandgap of 2D materials, electrons in the valence band can be excited to the conduction band, producing photo-excited EHPs. Driven by the build-in electric fields, those excess electrons and holes will be separated to opposite directions, leading to a light-generated current I_L. Especially, when the circuit is open, the accumulation of carriers induces a voltage (open circuit voltage V_{oc}), which lowers the potential barrier and generates a forward bias diffusion current that balances the light-generated current. If the external bias is set to be zero, the photo-excited EHPs will be collected, generating a photocurrent (short circuit current I_{sc}).

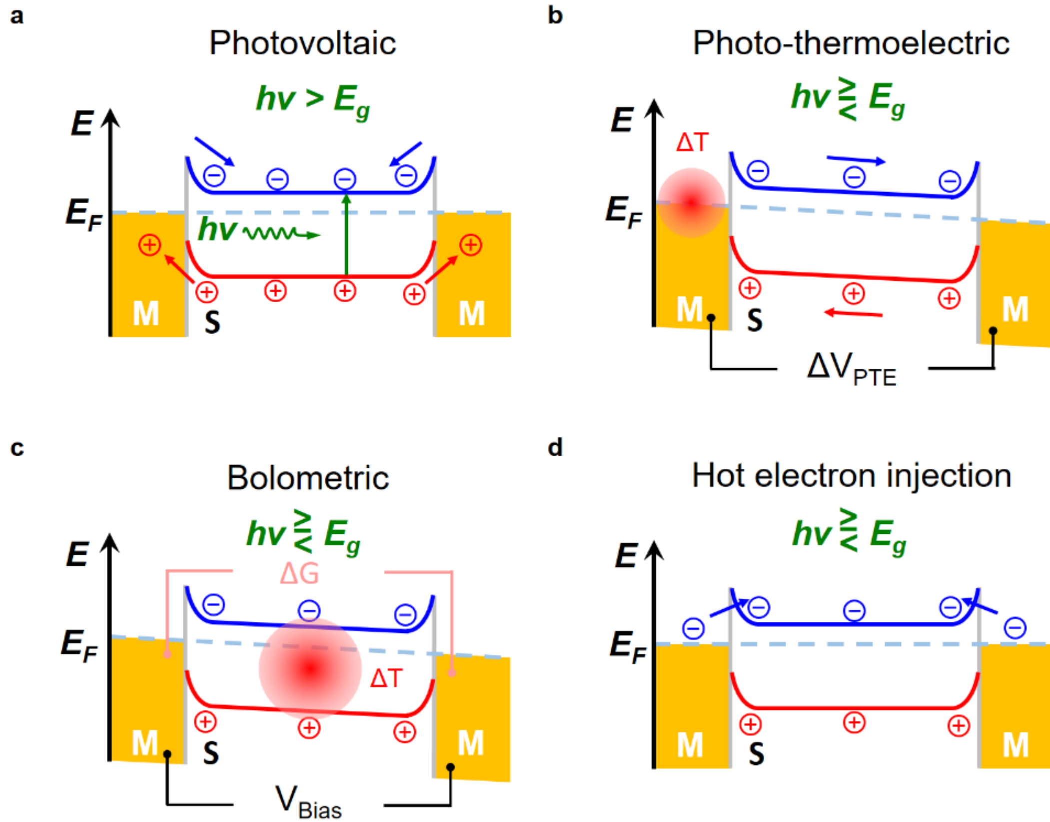

Figure 1.6 *Schematic representation of photocurrent-generation mechanisms in semiconducting 2D materials: PVE, PTE, PBE and hot electron injection.M and S indicate metal electrode contacts and 2D semiconductor channels, respectively. (a) Photon-excited EHPs separated by internal electric fields near the metal-semiconductor Schottky barriers. Red shaded areas indicate an elevated temperature* ΔT *induced by laser heating, leading to (b) A voltage difference* ΔV_{PTE} *or (c) overall conductance change* ΔG *across the channel. (d) Carriers are injected from metal electrodes into a 2D material channel. Reproduced with permission from ref.[55] with permission from MDPI.*

Photocurrent generation can also attribute to thermal mechanisms. Both PTE and PBE have been demonstrated to generate photocurrent by inducing a non-uniform heating and an overall conductance change of the 2D material channel when the light shines on certain region of the device or the whole device. Seebeck coefficient defines as the ability to induce thermoelectric voltage in response to a temperature difference across the material and can usually be expressed through the Mott relation:[56, 57]

$$S = \frac{\pi^2 {k_B}^2 T}{3e} \frac{1}{G} \frac{dG}{dE}\bigg|_{E=E_F} \tag{1.1}$$

where k_B is the Boltzmann constant, G is conductance, e is the electron charge, and E_F is Fermi energy. For a semiconductor channel that is connected to two metal electrodes, the light-induced temperature increase (ΔT) at the metal electrodes will generate a photo-thermoelectric voltage across the channel as displayed in Figure 1.6b. PTE drives a current through the junction even without applying an external bias, and the current value is directly related to the channel conductance and the photo-thermoelectric voltage, which is determined by the Seebeck coefficient difference between the semiconductor channel and the metal electrodes, and the temperature change:

$$\Delta V_{PTE} = (S_{semiconductor} - S_{metal})\Delta T \tag{1.2}$$

The Seebeck coefficients of pure metals are typically in the order of 1 μV/K. However, for 2D materials (such as graphene, MoS_2 and BP), the Seebeck coefficient ranges from several μV/K to thousands μV/K depending on the layer number and external gate voltage that applied.[58-62]

On the other hand, as shown in Figure 1.6c, the local heat up induced by photon absorption can modify the resistance of the channel. This light-induced conductance will lead to photocurrent under an external bias by PBE.[63, 64] The PBE induced photocurrent can be presented by the following equation:

$$I_{PBE} = \Delta G V_D \tag{1.3}$$

where ΔG is the conductance change and V_D is the external bias. From equation (1.3), we find that the PBE-induced photocurrent is predicted to present a linear relationship to the applied bias.

Hot electron injection is a novel photocurrent-generation mechanism that has been demonstrated in recent years.[65] It is well-known that photon-excited hot electrons in metal electrodes can cross over the Schottky barrier and be injected into the semiconductor channel. The injection yield of electrons Y follows the Fowler equation:

$$\boldsymbol{Y} \sim \frac{\mathbf{1}}{\mathbf{8}\boldsymbol{E_F}}\frac{(\boldsymbol{\hbar\omega} - \boldsymbol{\phi_B})^2}{\boldsymbol{\hbar\omega}} \tag{1.4}$$

where E_F is the Fermi energy, $\hbar$ is the reduced plank constant, ω is the incident light frequency, and ϕ_B is the Schottky barrier.

Photodetectors figure-of-merit

A set of Figures-of-merit facilitates the comparison between photodetectors working with different mechanisms and based on different materials and structures. In Table 1.1, I briefly summarize the figure-of-merit that is frequently used to characterize a photodetector.[66, 67]

Those performance indicators enable the comparison of low-dimensional material based photodetectors with silicon (CMO based), III-V InGaAs or HgCdTe photodetection system. Silicon photodetectors dominate the market in view of their high performance, low cost, maturity and high level of integration with electronics. Photodetection beyond silicon's bandgap, are currently relying on the aforementioned exotic semiconductors. Albeit offering high performance, those infrared photodetectors suffer from severe manufacturing costs and integration issues, and therefore are limited only to niche low-volume, high-value markets.

Low-dimensional materials need to prove their ability to achieve a form factor that cannot be implemented in the current photodetector technology landscape, or provide devices with less cost but maintain performance compactivity. Due to their high mobility and strong light interactions, several cases based on graphene and TMDC photodetectors have been demonstrated

to exhibit high modulation frequencies (for data communication), or high sensitivity (relevant for imaging and remote sensing).[49, 50]

Table 1.1 *Photodetectors figure-of-merit*

Figure-of-Merit	Unit	Equation	Definition
Wavelength range	nm		The electromagnetic spectrum that can be detected.
Responsivity (R)	A/W	$\frac{I_{photo}}{P}$	Photocurrent generated I_{photo} over incident light power P.
External quantum efficiency (EQE)		$\frac{n_e}{n_{photo}^{total}} = R \cdot \frac{hc}{e\lambda}$	the number of photo-excited carriers circulating through a given photodetector per incident photon, where h is the Plank constant, λ is the frequency of the incident laser, and e is the electron charge.
Internal quantum efficiency (IQE)		$\frac{n_e}{n_{photo}^{absorb}}$	the number of photo-excited carriers circulating through a given photodetector per absorbed photon.
Time response (t)	s	$t_{90\%} - t_{10\%}$	Time that measured between 10% and 90% of the generated signal under modulated excitation intensity, either on raising or decaying edge.
Bandwidth (B)	Hz	$f_H - f_L \cong f_H$	The modulation frequency the incoming light excitation at which the intensity of the detector signal is 3 dB lower than under continuous illumination.
Detectivity (D^*)	$cm\sqrt{(Hz)}/W$ or $Jones$	$\frac{\sqrt{A \triangle f}R}{i_n}$	A is the effective area of the detector in cm^2, $\triangle f$ is the electrical bandwidth in Hz and i_n is the noise current.
Noise quivalent power (NEP)	W	$\frac{i_n}{R}$	The minimum impinging optical power that a detector can distinguish from the noise.

To further compare those photodetectors, we first consider the most essential and straightforward performance indicators, responsivity. Many literatures have reported the achievement of ultrahigh gain and consequently record high responsivity values. However, those high values are often overestimated for the cases where photodetector speed is limited. The photodetector speed (can also be evaluated with response time) is of paramount importance, especially for the real-time image. For example, at least video frame rates ~30-60 Hz are required to enable taking high-quality video and the detector itself should be even faster than that in order to allow for other processing in image sensor arrays. Thus, the responsivity needs to be considered with response time, not itself. Figure 1.7a summarize the responsivity and time response of various

photodetector technologies and illustrates the path that needs to be followed for competitive emerging technologies.

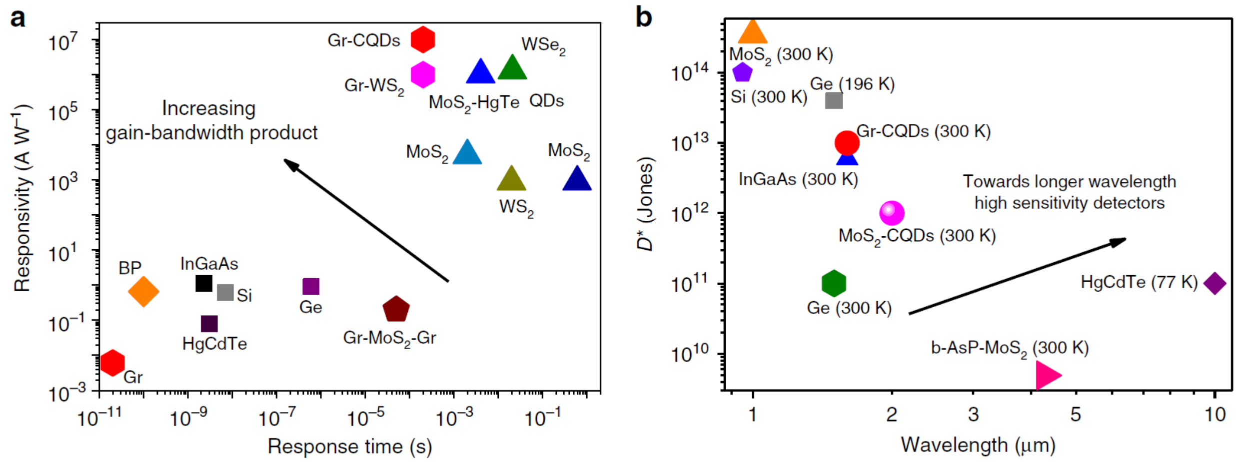

Figure 1.7 *Overview of performance metrics of standard and low-dimensional material based photodetector technologies.(a) Various photodetector technologies plotted against their corresponding responsivity and response time. The top left region corresponds to high gain-bandwidth-product detectors and should be the ultimate performance target of future photodetectors. (b) A plot of the specific detectivity D* of various photodetector technologies versus their absorption onset (bandgap). Low-dimensional material based photodetectors have the potential to address the grand challenge in photodetection towards low-cost, high sensitivity infrared detectors. Reproduced with permission from ref.[68] with permission from Springer Nature.*

On the other hand, sensitivity, which evaluates the ability to detect weak signals from detector noise, is another key performance indicator. Combine the responsivity and noise current, sensitivity performance can be quantified by specific detectivity D*. Figure 1.7b plots specific detectivity versus wavelength of different photodetectors, especially focus on long wavelength range where a cheaper photodetector is desired.

1.5 Scanning photocurrent microscopy

Scanning photocurrent microscopy is a versatile method for investigating optoelectronic properties of nanoelectronic devices. As illustrated in Figure 1.8a, a laser beam is expanded and

focused by a 40X Olympus objective into a diffraction-limited spot and raster scans over the target device by a piezo-controlled scan mirror with nanometer-scale spatial resolution (see Figure 1.8a). Both reflection and photocurrent signals were collected as a function of the position. By correlating the reflection mapping with the optical mapping of the device, the positions of photocurrent signals ($I_{pc} = I_{laser} - I_{dark}$) can be precisely located. Here a single wall carbon nanotube (SWNT) that bridge between Pt electrodes is shown as the target device. As shown in Figure 1.8b, after the laser scans over the SWNT, all mappings obtained can be carefully aligned to each other, precisely showing reflection and photocurrent signals at each position. For the SWNT, strong photocurrent responses are observed along the tube, under the assumption that the photocurrent is proportional to the local potential gradient.

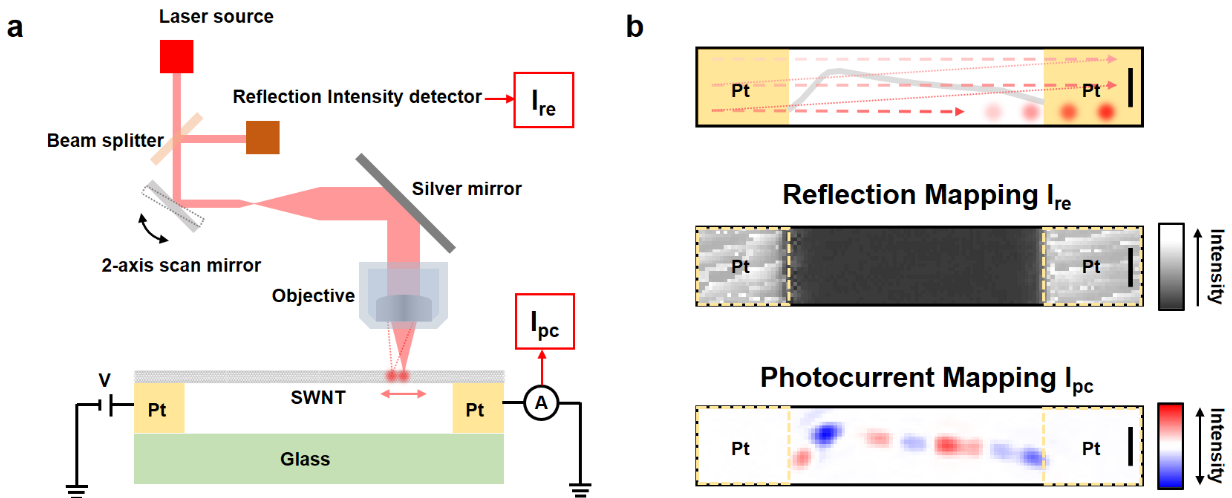

Figure 1.8 *Scanning photocurrent microscopy: schematic layout and scanning photocurrent mapping of a SWNT.(a) An illustration diagram of the experimental setup for scanning photocurrent measurement. A suspended single wall carbon nanotube device is shown as an example. (b) Top: device top view, which shows the scanning area. Red arrows indicate scanning direction. Middle and bottom: corresponding reflection (greyscale, white is the maximum) and photocurrent mapping (red and blue color represent positive and negative current while white color shows zero photocurrent). Light gold dash boxes indicate Pt electrodes. The scale bar is 1 μm.*

For most of our scanning photocurrent measurements, the laser source is a continuous wave laser beam form NKT Photonics SuperK Supercontinuum Laser, which offers single-mode output with bandwidth 1-5 nm and could cover wavelength range from 450 to 2000 nm (1nm step) with power up to several hundred micro watts for each wavelength. Depending on the size of the device, objective from Olympus with various magnification can be used (40X, numerical aperture NA = 0.6; 10X, NA = 0.4; 4X, NA = 0.1). The size of the focused laser beam, which determines the spatial resolution of the mapping can be various, since the diffraction-limited is related to both NA and laser wavelength λ ($d = \frac{\lambda}{2NA}$) . Therefore, for a certain objective, shorter wavelength will offer mapping with higher resolution and also note that shorter wavelength photon will carrier more energy considering Planck–Einstein relation ($E = \frac{hc}{\lambda}$, h is the plank constant and c is the speed of light). Furthermore, the laser from the source device is free space and linear polarized. By adding a half-wave plate followed by a polarizer to the laser path, the polarization direction of the laser spot can be easily adjusted to any direction. The laser power can be precisely controlled by tuning the laser source or can be attenuated by applying a neutral-density filter. In summary, the scanning photocurrent microscopy provides a versatile platform for photoelectronic measurements, where the laser position, wavelength, power and polarization direction can be flexibly controlled to meet various experiment requirements.

Chapter 2 High Performance WSe_2 Photodetectors with 2D/2D Ohmic Contacts

2.1 Ohmic contacts

In traditional silicon based FET, heavily doped silicon buffer layers are existed between the lightly doped silicon channel and the metal electrodes to achieve ohmic contacts. In details, as shown in Figure 2.1a, for a metal and an *p*-type semiconductor, a rectifying Schottky contact is formed when $W_m<W_s$ (Similarly, for a metal and an *n*-type semiconductor, the contacts will be rectifying Schottky when $W_m>W_s$). Here W_M and W_S denote work function for metal and semiconductor as the work function is defined as the energy difference between the Fermi energy and the vacuum level. Also, here we consider the ideal metal-semiconductor (MS) contacts with following assumptions: i. both materials are infinitely pure; ii. no interaction between the two materials; iii. no interfacial layer.

For Schottky contacts, a barrier exists between the metal and semiconductor, leading to a large exponentially increased current with forward bias and a small constant current at reversed bias (Figure 2.1b). Theoretically, non-rectifying, or ohmic contacts can be achieved by choosing different metals to match the work function of the semiconductors ($W_m<W_s$ for *n*-type semiconductor and $W_m>W_s$ for *p*-type semiconductor). However, in reality, it's challenging due to the pin effect that caused by semiconductor surface states. To account for pin effects, the metal-semiconductor contacts can be treated as if it contained an intermediate region sandwiched between the metal and the semiconductor. This layer contains the added interface states, and therefore, the MS contacts will depend on the metal and the interface layer rather than metal and semiconductor especially if the state density becomes very large.

As a result, in practice, ohmic contacts is accomplished by adding a heavily doped layer between the semiconductor channel and the metal (Figure 2.1c). The contact barrier width X_d can be solved by following equation:[69]

$$X_d = \sqrt{\frac{2\epsilon_{s\phi_i}}{qN_d}} \quad (2.1)$$

where ϵ_s is the permittivity of the semiconductor, ϕ_i=W_s-W_m is the built-in voltage, N_d is the donor atomic density and q is the electronic charge**.** therefore, the contact barrier narrows as N_d increases. When the barrier width approaches a few nanometers tunneling through the barrier can take place. Electrons are available to tunnel from semiconductor to metal or metal to semiconductor and current rise very rapidly as bias is applied regardless of the polarity of the bias. Hence, a MS contact at which tunneling is possible has a very small resistance, virtually an ohmic contact.

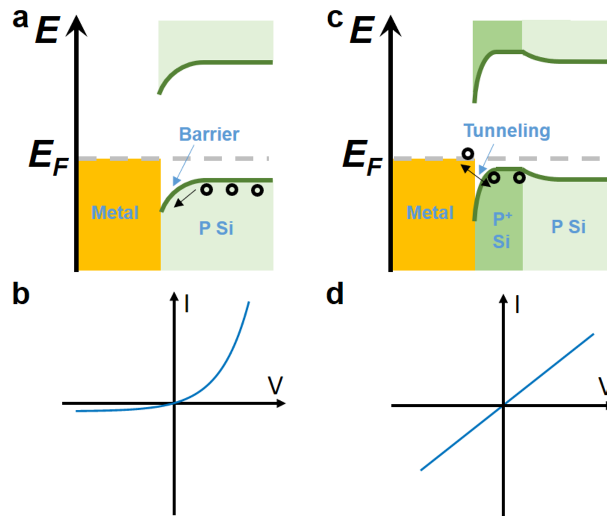

Figure 2.1 *MS contacts: Schottky contacts versus ohmic contacts. Band alignment between MS system with (a) Schottky contacts and (c) ohmic contacts. (c) Rectifying output curve for Schottky contacts and (d) linear output curve for ohmic contacts.*

2.2 Engineering MS contacts for TMDC based phototransistor

The performance of a phototransistor depends on both the optical properties of the channel material and the electrical behaviors of the device, where the former dictates the spectral coverage and quantum efficiency of the phototransistor and the latter governs the charge density, the dark current, and the efficiency of charge separation and collection upon illumination. It is well-known that the photocurrent responses of TMDC based phototransistors are mainly attributed to the separation of photo-excited EHPs driven by built-in electric fields near the Schottky-barriers between 2D materials and metal contacts.[17, 51, 70]

Numerous efforts have been made to engineer the TMDC-metal contacts to enhance the photoresponsivity and reduce the response time since the Schottky-barriers between the TMDC channel and metal contacts play an important role for conventional photodetectors based on the MSM structure.[17, 65, 71-75] A recent study has reported that the photoresponse of WSe_2 phototransistors can be enhanced by reducing the Schottky-barrier between WSe_2 channels and metal contacts, but these phototransistors display very slow response speed in ambient air (> 5 s), severely limiting their performance as photodetectors.[74] In fact, it remains a major challenge to design a novel TMDC based phototransistor architecture that simultaneously yields a high photoresponsivity and a short response time. While it is well established that the photoresponse of TMDC phototransistors is sensitive to their electrical contacts, WSe_2 phototransistors with truly ohmic contacts have not been reported to the best of our knowledge because WSe_2 tends to form a substantial Schottky barrier with most metals commonly used for making electrical contracts, which can be partially attributed to Fermi level pinning.

2.3 WSe_2 phototransistor with 2D/2D Ohmic Contact

Here we report a new approach to fabricate high performance WSe_2 based phototransistors by using degenerately *p*-doped 2D TMDCs as the drain/source contacts and 2D WSe_2 with no intentional doping as the channel to form 2D/2D ohmic contacts. Metal interconnects were subsequently fabricated to connect the degenerately *p*-doped WSe_2 drain/source contacts for electrical and photocurrent measurements. Because the degenerately *p*-doped WSe_2 is a highly conductive version of the channel material, it forms low-resistance contacts with both the WSe_2 channel and the metal interconnects. As demonstrated in the previous report, the 2D/2D contacts allow low contact resistance, and the degenerately *p*-doped WSe_2/metal contacts also show negligible contact resistance due to tunneling effect through an extremely narrow (~ 1 nm) depletion region.[76]

Figure 2.2a illustrates the schematic diagram of a WSe_2 phototransistor, where an undoped 2D WSe_2 channel was in contact with two degenerately *p*-doped WSe_2 ($Nb_{0.005}W_{0.995}Se_2$) thin films as the drain and source contacts, which were connected to metal electrodes. To provide a smooth substrate with minimum dangling bonds and charge traps, a thin hBN flake was placed between the WSe_2 phototransistor and the degenerately-doped Si substrate covered with a 280-nm-thick thermal SiO_2 layer.[46] Both WSe_2 and hBN flakes were mechanically exfoliated from their bulk crystals. The thicknesses of the cleaved flakes were 10-30 nm for hBN and 3-10 nm for the undoped WSe_2 as identified by atomic force microscopy (AFM). Using a dry transfer method, two degenerately *p*-doped WSe_2 flakes were artificially stacked atop an undoped WSe_2 flake to form 2D/2D contacts. Metal electrodes were then fabricated on top of the degenerately *p*-doped WSe_2 drain/source contact regions by standard electron beam lithography (EBL) and subsequent deposition of 5/50 nm Ti/Au. Figure 2.2b presents the optical image of a typical device with an 8.3 nm thick WSe_2 channel, where all TMDC flakes and Au electrodes are outlined by colored

dashed lines. Back-gate biases were applied to the WSe_2 channel through a dielectric stack consisting of 280 nm SiO_2 and a 30 nm thick hBN flake. Both electrical and optoelectronic properties of the device were characterized under high vacuum (~10^{-6} Torr).

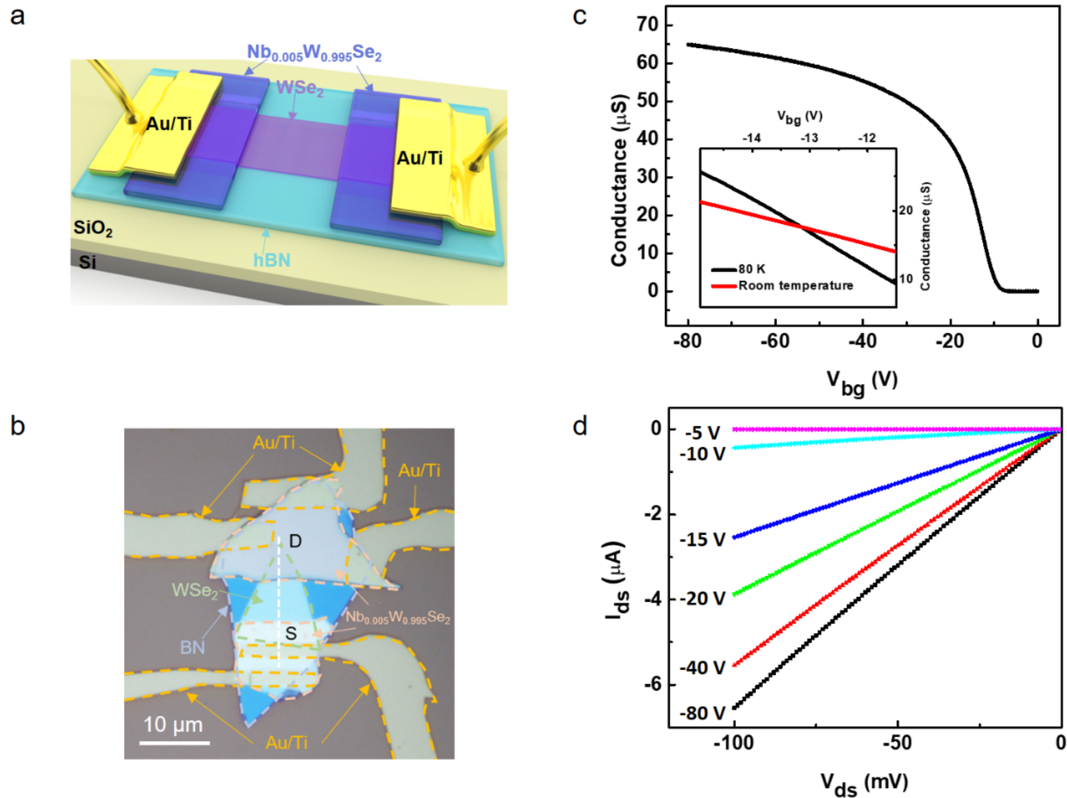

***Figure 2.2** Structure and electronic characteristics of WSe_2 phototransistors with 2D/2D ohmic contact.(a) A schematic illustrating the layout of a typical WSe_2 phototransistor. (b) Optical micrograph of the device. S and D indicate source and drain contacts, respectively. The gold dashed lines mark the position of the metal electrodes. The blue dashed line outlines the hBN thin film. The pink and green dashed lines represent the outlines of the Nb-doped WSe_2 contacts and undoped WSe_2 channel, respectively. (c) Gate-dependent transport characteristics of the device. Inset: linear region for mobility calculation at 80 K and room temperature, respectively. (d) Ids-Vds characteristics at various back-gate voltages at 80 K. Reproduced with permission from ref.[77], with permission from American Chemical Society*

Figure 2.2c displays the transfer characteristics of the device. *P*-type behaviors are observed with a field-effect hole mobility of ~150 $cm^2 \cdot V^{-1} \cdot s^{-1}$ at room temperature, which increases to ~300 $cm^2 V^{-1} s^{-1}$ at 80 K calculated from the linear region (inset of Figure 2.2c) of the

transfer curves by using the expression $\boldsymbol{\mu_{FET}} = \left(\frac{1}{C_{bg}}\right) \cdot \left(\frac{L}{W}\right) \cdot \left(\frac{d\sigma}{dV_{bg}}\right)$. Here, L and W are the length and width of the channel, and C_{bg} is the back-gate capacitance of the 280 nm thick SiO_2 in series of a 30 nm hBN flake. Figure 2.2d shows linear output characteristics of the WSe_2 phototransistor with 2D/2D contacts when various back-gate voltages were applied at 80 K, indicating ohmic behaviors of the device. To understand the critical role of heavily *p*-doped TMDC contacts in the superior electronic and optoelectronic performances of WSe_2 devices with 2D/2D contacts, we also fabricated few-layer WSe_2 transistors on hBN substrates with Ti/Au contacts. The output characteristics of few-layer WSe_2 transistors with Ti/Au contacts are non-linear and asymmetric, which can be attributed to the presence of a Schottky barrier at the contacts.

2.4 Scanning photocurrent mapping and response spectrum

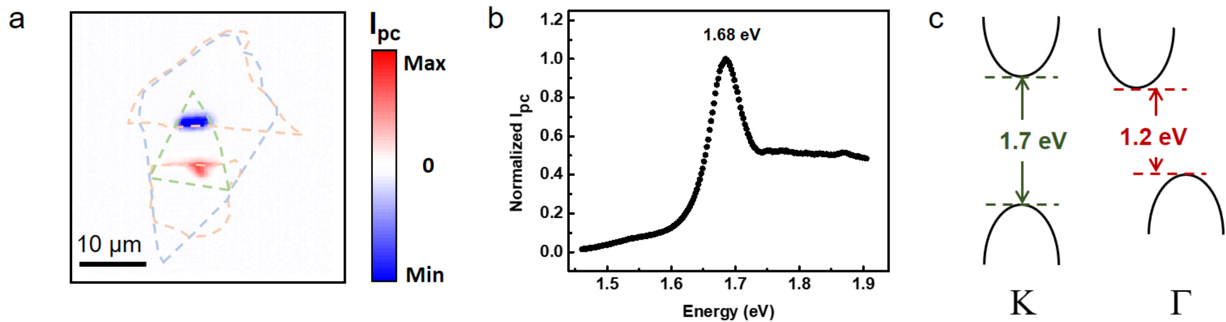

Figure 2.3 *Scanning photocurrent mapping and wavelength dependent photoresponse. (a) Scanning photocurrent image of the device (measured between S and D) and (b) normalized wavelength dependence of the photocurrent signals under a zero source-drain bias with V_{bg} = 0 V. (c) Illustration of direct and indirect bandgaps in few-layer WSe_2. Reproduced with permission from ref.[77], with permission from American Chemical Society*

To investigate the photoresponse of the WSe_2 phototransistor with 2D/2D contacts, we performed spatially-resolved scanning photocurrent measurements on the device in a Janis ST-500 microscopy cryostat at 80 K. As shown in Figure 2.3a. Remarkable photocurrent signals were

detected at the 2D/2D interfaces between the undoped WSe_2 channel and degenerately *p*-doped WSe_2 contacts, where the built-in electric fields can separate photo-excited EPHs to opposite directions and induce photocurrent signals through the PVE. However, the photocurrent signals at the degenerately-doped-WSe_2/metal junctions were negligible due to the near absence of a depletion region at these interfaces.[76]

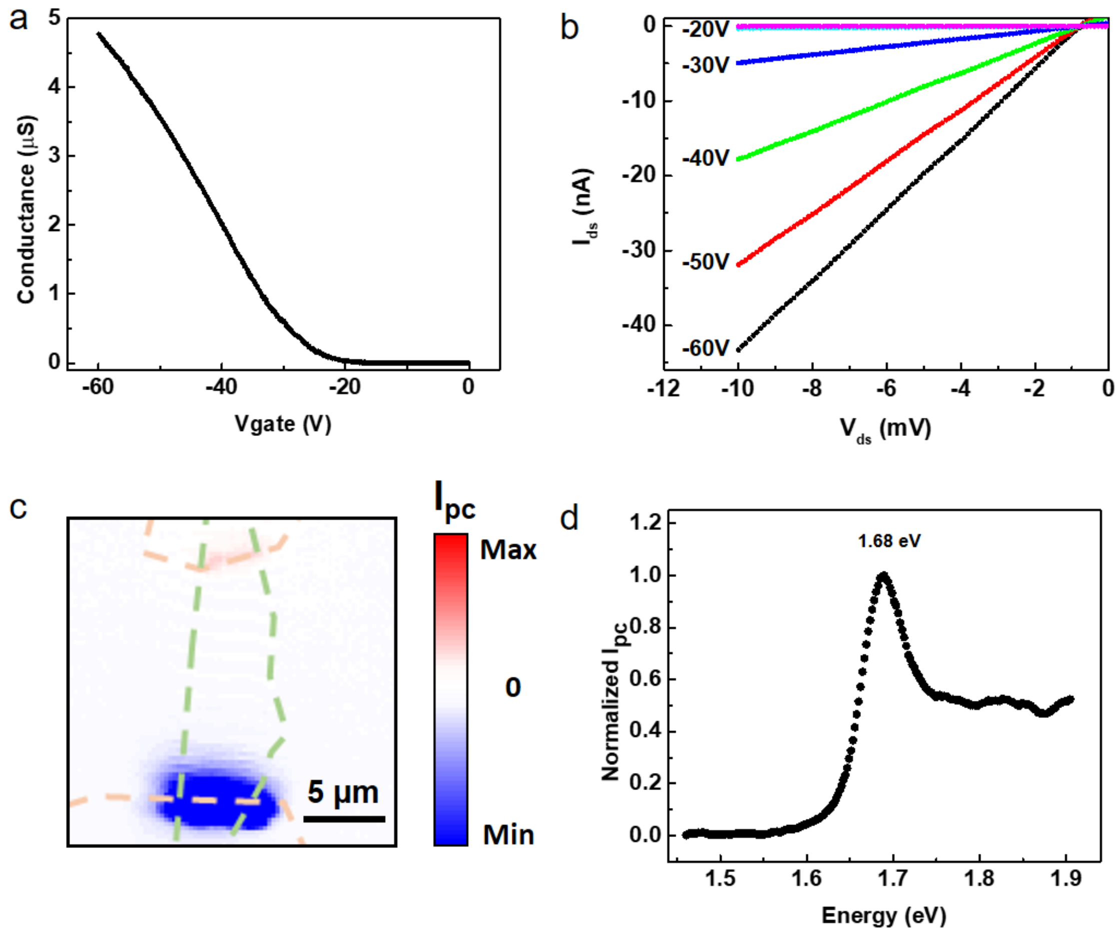

Figure 2.4 *Electronic and optoelectronic characteristics for a typical WSe_2 phototransistor with degenerately p-doped MoS_2 as source/drain contacts. (a) Gate-dependent transport characteristics at 80 K and (b) I_{ds}-V_{ds} characteristics at various back-gate voltages at 80 K. (c) scanning photocurrent image of the device. The pink and green dashed lines represent the outlines of the Nb-doped MoS_2 contacts and undoped WSe_2 channel, respectively. (d) Normalized wavelength dependence of the photocurrent signals under a zero source-drain bias with V_{bg} = 0 V. Reproduced with permission from ref.[77], with permission from American Chemical Society*

Wavelength-dependent photocurrent measurements were further conducted to elaborate the photocurrent generation mechanisms at the 2D/2D contacts. As shown in Figure 2.3b, maximum photocurrent responses of the WSe_2 phototransistor with degenerately *p*-doped WSe_2 drain/source contacts were observed when the incident photon energy was ~ 1.68 eV, close to the reported direct bandgap of few-layer WSe_2.[12, 13, 19, 78-81] To clarify the photoresponse contribution at 2D/2D contacts, we also tested WSe_2 FETs with degenerately *p*-doped MoS_2 as the drain/source contacts. As shown in Figure 2.4a, WSe_2 devices with doped MoS_2 as source/drain contacts have shown similar *p*-type behaviors. Moreover, their linear output characteristics suggest low resistance ohmic contacts (Figure 2.4b). We have also found that strong photocurrent signals locate at the 2D/2D interfaces between the undoped WSe_2 channel and degenerately *p*-doped MoS_2 contacts (Figure 2.4c). Interestingly, their maximum photoresponses also occurred when the excitation laser energy approached the direct bandgap of WSe_2, suggesting that the photocurrent generation mainly results from the direct transition in undoped WSe_2 channels (Figure 2.3c). Moreover, the photoresponsivity drops dramatically when the wavelength of the incident laser is longer than 750 nm (~ 1.65 eV), indicating that the contribution from the indirect transition (~ 1.2 eV) in WSe_2 is negligible.

2.5 Bias-dependent scanning photocurrent mapping

The entire WSe_2 channel can absorb the incident light and generate EHPs. Without external source-drain bias, the WSe_2 flake in the central channel region is uniform, resulting in a flat band diagram. Both electrons and holes can move freely to any direction, contributing to a zero net current. When an external electric field is applied to the WSe_2 channel, the photoresponse will occur in the central channel region. While the intrinsic lifetime for 2D TMDCs were reported in the range from picoseconds to nanoseconds depending on either the thickness or the

temperature.[82-84] As a result, much fewer photo-excited EHPs are expected to be collected by source/drain electrodes before recombination, leading to small photocurrent signals in comparison with that generated at the 2D/2D interfaces (Figure 2.3a). On the other hand, the built-in electric fields at the 2D/2D interfaces between the undoped WSe_2 channel and degenerately *p*-doped WSe_2 contacts can separate photo-excited EHPs to opposite directions, leading to a current that travels from the undoped channel to *p*-doped contacts. When the drain-source bias sweeps from -1 V to 1V, the intensity of positive (negative) photocurrent signals increases (decreases, Figure 2.5), suggesting that the photocurrent response is mainly attributed to the PVE. Similar results have also been reported previously.[85, 86]

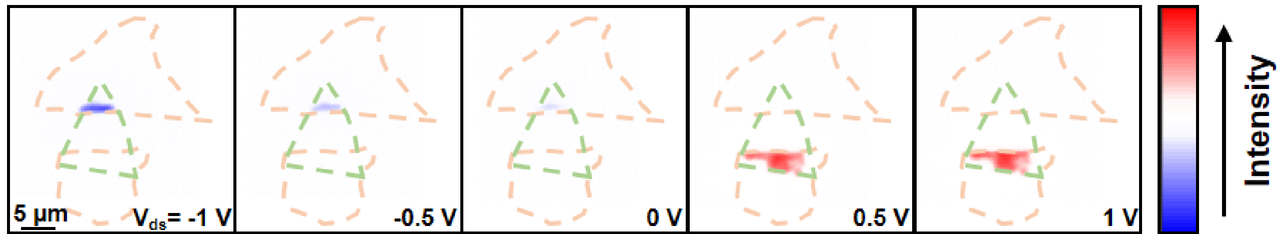

Figure 2.5 *Bias dependent scanning photocurrent mapping. Scanning photocurrent images of a typical WSe_2 phototransistor when the drain–source bias voltages ranging from -1 V to +1 V with a 0.5 V step. Red/blue color corresponds to the positive/negative photocurrent response, respectively. Reproduced with permission from ref.[77], with permission from American Chemical Society*

2.6 Photodetection performances

We then evaluated the performance of the WSe_2 phototransistor at V_{bg} = 0 V, where the device is in the OFF state with a negligible dark current (~ 10^{-14} A). A laser spot (~ 50 µm in diameter) that was large enough to cover the whole device was used as the illumination source. As shown in Figure 2.6a, photocurrent signals were recorded as a function of drain-source bias from 0 V to +1 V under various laser illumination intensities, displaying a nonlinear dependence on V_{ds},

which is similar to previous reported 2D photodetectors.[51, 86] In addition, higher photoresponsivities were observed at larger positive drain-source bias because the bias enhances local band bending in one of the 2D/2D contact regions while eliminating the band bending in the other, and also generates an electric field in the channel, which consequently facilitates the more efficient separation and collection of the photo-excited EHPs. Figure 2.6a plots the photocurrent generated by the phototransistor (V_{ds} = 1 V) at various laser illumination intensities. A photoresponsivity R ($R = I_{pc}/p$, where p is the power of the incident laser) of 320 mA/W was observed at a zero back-gate voltage, which is independent of the incident laser power as illustrated by the linear relationship between the photocurrent and laser power (Figure 2.6b). The nearly linear dependence of the photocurrent on the absorbed photo flux strongly indicates that the measured photocurrent signals primarily result from the absorption of the WSe_2 channel instead of the thermionic and tunneling currents.[74, 87]

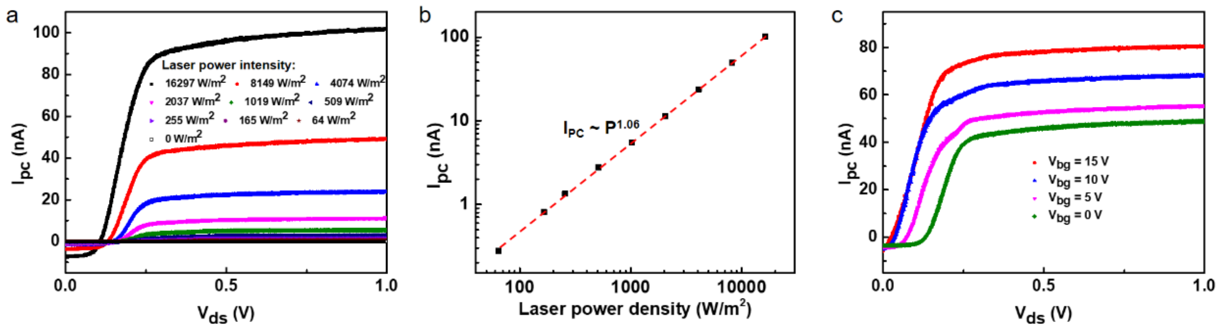

Figure 2.6 *Photoresponse as a function of source-drain bias voltage under various back-gate voltages and at various values of the optical power intensities.(a) Photocurrent I_{pc} as a function of source-drain bias voltage V_{ds} under zero back-gate voltage and at various values of the optical power intensities (wavelength λ = 735 nm). (b) Power dependence at V_{ds} = 1 V. (c) Photocurrent I_{pc} as a function of source-drain bias voltage V_{ds} under back-gate voltages varying from 0 to 15 V with a 5 V step. 735 nm laser illumination was used with a power intensity of 8149 W/m^2. Reproduced with permission from ref.[77], with permission from American Chemical Society*

To further enhance the photoresponsivity, we measured photocurrent signals as a function of external back-gate voltages with a laser power of ~ 8149 W/m^2 (Figure 2.6c). Photoresponsivity was enhanced when back-gate voltage raised in the positive direction, where the long depletion region with high voltage drop can efficiently separate the photo-excited EHPs, resulting in high photoresponsivity and fast response time.[74] A photoresponsivity of ~ 600 mA/W was achieved at V_{bg} = 15 V, which almost doubled from that at a zero gate voltage. A large external quantum efficiency (EQE) close to 100% was also observed for the OFF state of the device. Here EQE is defined as the number of photo-excited carriers circulating through a given photodetector per absorbed photon, $\eta = Rhv/e$, where h is the Plank constant, v is the frequency of the incident laser, and e is the electron charge. Another important parameter of a photodetector is its specific detectivity D^* that is related to its signal-to-noise ratio. The specific detectivity is given by $D^* = RA^{\frac{1}{2}}/(2eI_{dark})^{\frac{1}{2}} \sim 10^{13}\ Jones$ for our device in the OFF state, where A is the area of the detector. The values of photoresponsivity, EQE, and specific detectivity of our device obtained in the OFF state in high vacuum are comparable or higher than those of WSe_2 photodetectors in previous reports,[52, 74, 75, 88] as well as those of commercial silicon (500 - 600 mA·W^{-1}, 80%, ~ 10^{12} Jones) and InGaAs (700 - 900 mA·W^{-1}, 60%, 10^{12}-10^{13} Jones) photodetectors.[89]

2.7 Photoresponse dynamics

Temporal response is another critical figure-of-merit for photodetectors. To study the photoresponse dynamics of WSe_2 phototransistors, we applied ON/OFF light modulation by adding an optical chopper into the system and measured the rise and decay time constants. Figure 2.7a shows a schematic of the experimental setup, where photocurrent signals were collected as a function of time with the laser turning ON and OFF. The rectangular excitation pulse generated by the chopper has a width of ~ 80 μs with a rise time of ~ 100 ns, which is much faster than the

timing resolution of our current preamplifier used in our measurements (~ 8 μs). By applying a single exponential function to fit the rising and decaying region of the curve, a typical response time constant of $\tau_{rise} = \tau_{decay} = 8\ \mu s$ was obtained (Figure 2.7b), which has already reached the limit of the measurement circuit. Therefore, the time constant is expected to be short than 8 μs if time-resolved measurements of improved accuracy at low current level are accessible. Both the rise and decay times of our device are faster than previously-reported TMDC-based photodetectors.[17, 51, 74, 90-92]

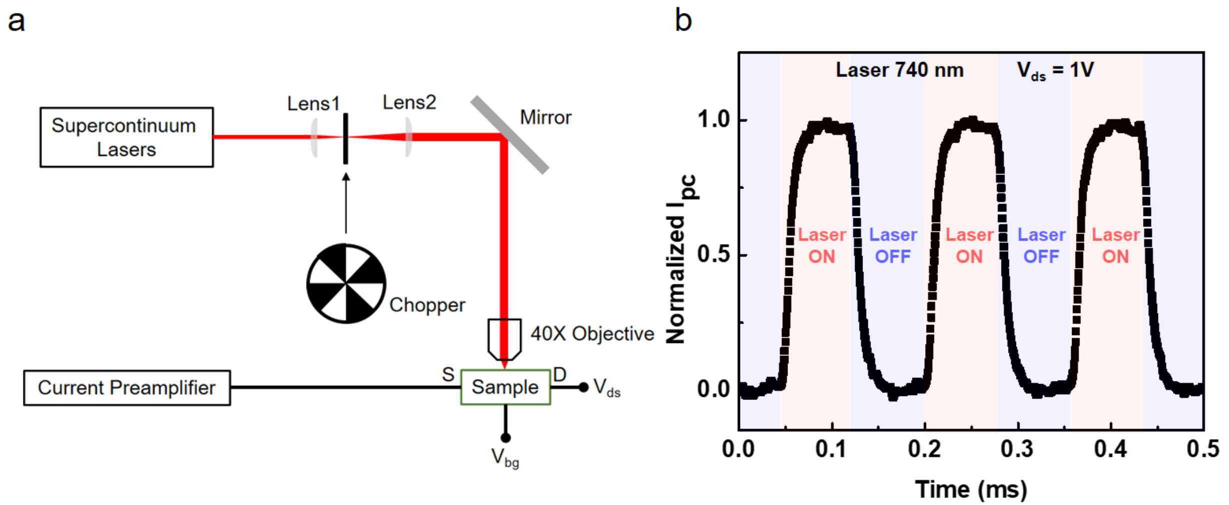

Figure 2.7 *Experimental setup for photoresponse dynamics and ultrafast photorsponse.(a) A schematic diagram of the experimental setup for measuring time dependent photoresponse. (b) Photocurrent signals as a function of time under 740 nm laser illumination with a modulation frequency ~ 6.4K Hz. The laser power was 0.46 μW and photocurrent signals were collected at* V_{ds} *= 1V.* Reproduced with permission from ref.[77], with permission from American Chemical Society

2.8 Photocurrent generation mechanisms

To further elucidate the photoresponse generation mechanisms of our WSe_2 high performance phototransistor, gate-dependent scanning photocurrent measurements were subsequently performed by sweeping the gate voltage from 0 V to -11 V while recording the

photocurrent along the channel direction of the WSe_2 photodetector (dashed line in Figure 2.2b). As shown in Figure 2.8a, the photocurrent signals at the 2D/2D contacts of the WSe_2 phototransistor gradually decrease when the back-gate voltage was swept from 0 V (OFF state) in the negative direction. The pronounced photocurrent observed in the OFF state (V_{bg} = 0 V, Figure 2.8b) can be explained by a band offset at the degenerately *p*-doped/undoped WSe_2 junction, where the Fermi level of the WSe_2 channel is above its valence band and the conduction/valence band of the undoped WSe_2 channel bends upward owing to Fermi level alignment, leading to a built-in electric field from the channel to the contact. As a result, photo-excited EHPs at the band bending area can be easily separated to the opposite directions, contributing to photocurrents that flow from the undoped WSe_2 channel to the degenerately *p*-doped WSe_2 contact.

When we swept the back-gate voltage in the negative direction, the Fermi level approaches the valence band of the undoped WSe_2 channel, reducing the band mismatch. A flat band structure is reached in the undoped WSe_2 channel at $V_{bg} \sim -11$ V, (Figure 2.8c), making it difficult to separate the photo-excited EHPs. Therefore, negligible photocurrent signals were detected near flat band voltage $V_{FB} = -11$V. Interestingly, the flat band voltage determined by the photocurrent measurement is nearly identical to the threshold voltage observed in the transfer characteristic of the device (see Figure 2.2c), suggesting that the 2D/2D contacts in our WSe_2 phototransistors are nearly free of a Schottky barrier because the presence of a finite Schottky barrier usually leads to a notable discrepancy between the flat band and the threshold voltages.[86] This is consistent with our previous electrical transport characterization that 2D/2D contacts between doped and undoped WSe_2 are ohmic,[76] which also likely contributes to the fast and efficient photoresponse of our device.

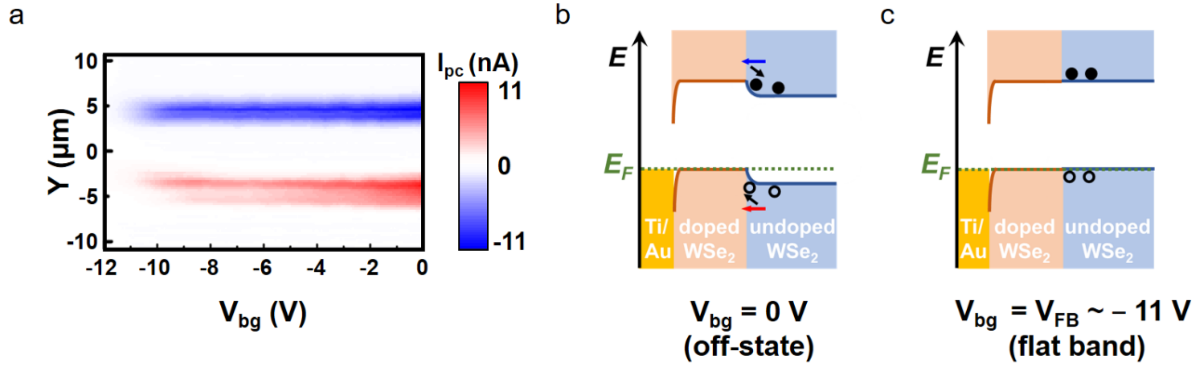

Figure 2.8 *Gate-dependence photoresponse and photocurrent generation mechanisms.(*(a) Gate-dependence of the photocurrent signals without source-drain bias. Band profiles of the device at (b) $V_{bg} = 0$ V and (c) $V_{bg} = V_{FB} = -11$ V, respectively. Reproduced with permission from ref.[77], with permission from American Chemical Society

Two important factors that limit the response time of a photodetector are RC time constant and carrier transit time.[93] For a WSe_2 phototransistor, the total resistance includes both the contact and the channel resistances. 2D/2D ohmic contacts have small contact resistances, reducing the RC time constant and thus facilitate the fast response of the detector. Moreover, under illumination the photo-excited carriers will travel cross the high-field region and then be collected by the electrodes. therefore, the carrier transit time between the source and drain electrodes will also influence the response time of a detector. The mobility of our device is much higher than other WSe_2 phototransistors due to the 2D/2D ohmic contact, which can reduce the carrier transit time and then the response time of the detector. The high mobility also leads to high photoresponsivity $R \propto I_{pc} \propto ne\mu$, where n is the photo-excited carrier concentration and μ is the carrier mobility. In addition, the outside environment near the device surface may also play an important role in their photocurrent generation dynamics, so further improvements could be realized by encapsulating the device with a thin hBN flake on the top so the devices are fully sealed and the influence of environmental factors are minimized.[47, 51]

2.9 Conclusion

In summary, we report high performance WSe_2 photodetectors with 2D/2D ohmic contacts. The 2D/2D ohmic contacts enable outstanding electrical transport behaviors of the WSe_2 phototransistors with a field-effect hole mobility of ~300 $cm^2 \cdot V^{-1} \cdot s^{-1}$, leading to a high photoresponsivity of ~ 600 mA/W with a high external quantum efficiency up to 100% and a response time (both rise and decay times) shorter than 8 μs. More importantly, our WSe_2 phototransistor exhibits a high specific detectivity (~10^{13} Jones) in vacuum, comparable or higher than commercial Si and InGaAs based photodetector. Photocurrent signals are detected at the 2D/2D interface and show maximum photoresponsivity when the illumination energy of laser is close to the direct bandgap of the undoped WSe_2 channel. Gate-dependent photocurrent measurements reveal that the high photoresponsivity and short response time are mainly attributed to the lack of Schottky barriers at the 2D/2D contacts, which can reduce the carrier transit time and improve the photo-excited EHP collection. Our work provides an in-depth understanding of the photocurrent generation mechanisms in 2D TMDC based phototransistors and offers a new direction to improve the performance of 2D material photodetectors through a truly ohmic contact between doped/undoped TMDCs.

2.10 Methods

Materials Synthesis

$Nb_{0.005}W_{0.995}Se_2$ crystals were synthesized from polycrystalline powders and iodine as a transport agent by chemical vapor transport in sealed silica tubes. The polycrystalline $Nb_{0.005}W_{0.995}Se_2$ powders were first prepared from stoichiometric mixtures of W (99.999%), Se (99.999%), and 0.5% of Nb (99.99%) was used as substituent atoms for *p*-doping. The mesh size was -22 for W, -200 for Se, and -325 for Nb. The starting materials were sealed in silica tubes

under vacuum, and then slowly heated to 900 ºC. The ampoules remained at 900 ºC for seven days, and then were allowed to furnace cool to room temperature. Phase purity is confirmed with powder x-ray diffraction. Single crystals of $Nb_{0.005}W_{0.995}Se_2$ were then grown using the polycrystals as starting material and iodine as a transport agent (~17.5 mg/cm^3 of iodine). The silica tubes containing phase-pure powder and iodine were sealed under vacuum and placed in a tube furnace with a 50 ºC temperature gradient from the hotter end of the tube containing the charge (1035 ºC) to the colder end where growth occurs at 985 ºC. Crystals in the form of shiny silver plates with typical size 5 × 5 × 0.1 mm^3 grew over the course of 5 days. The as-grown crystals were phase-pure as determined by x-ray diffraction. Elemental analysis was performed using wavelength dispersive spectrometry (WDS) on a Camec SX100 electron microprobe. An accelerating voltage of 20 kV and a beam current of 40 nA are used in a spot size of 5 μm. $CaWO_4$, CdSe, and $SnBaNb_4O_{10}$ were used as standards for quantification. The detection limit of the spectrometer is around 0.03 wt %. A quantitative analysis of $NbxW_{1-x}Se_2$ reveals an actual dopant concentration of x = 0.40 at. %.

Chapter 3 Visualizing Light Scattering in Silicon Waveguides with Few-layer BP Photodetectors

3.1 Black phosphorus

Black phosphorus (BP) is a relatively new addition to 2D vdW material family, which consists of only phosphorus atoms. The semiconducting puckered orthorhombic BP has reduced symmetry compared with its group IV counterparts (such as graphene). As displayed in Figure 3.1a, along with the out-of-plane direction, each phosphorus atom is covalently bonded with three adjacent phosphorus atoms o form a puckered honeycomb structure. From the front side view, the single-layer BP includes two atomic layers and the covalent P–P bonds can be classified into two kinds. Two shorter bonds connect the nearest P atoms in the same plane, and one longer bond connects P atoms between the top and bottom of a single layer. Each BP layer bond together by vdW force with spacing around 5 Å.

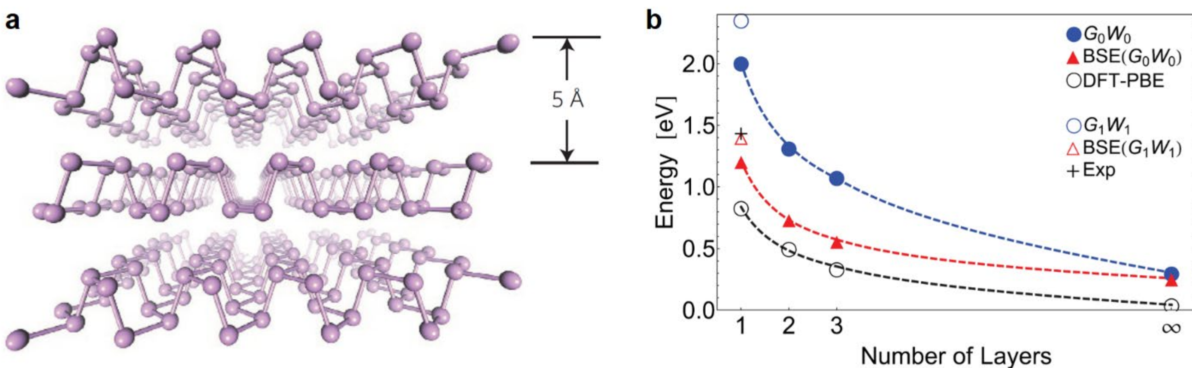

Figure 3.1 *Crystal lattice and layer-depended bandgap of BP. (a) Atomic structure of black phosphorus. Reproduced with permission from ref[13], with permission from Springer Nature (b) The evolution of band gap calculated by different methods and optical absorption peak according to the stacking layer number of few-layer phosphorene. The power-law fitting curves are presented by dashed lines. The experimental optical peak position is read from Ref.[94]. Reproduced with permission from ref.[67], with permission from American Physical Society*

Few-layer BP has been demonstrated to show outstanding electrical and optical properties, such as mobility up to 1,000 $cm^2 \cdot V^{-1} \cdot s^{-1}$ in field-effect transistors and photoresponsivity up to 4.8 mA/W in photodetectors.[21, 44, 86, 95-97] Moreover, BP has a layer-tunable direct bandgap ranging from 0.3 eV in bulk to 1.8-2.0 eV for the monolayer as shown in Figure 3.1b which bridges the zero bandgap graphene and relatively large bandgap TMDCs and thus makes BP an ideal candidate for broadband optoelectronic applications from visible to the mid-infrared spectral range.[98-101] Moreover, anisotropic in-plane lattice structure allows BP to possess anisotropic electrical conductance as well as anisotropic light interactions.

3.2 Photonic structure - low dimensional material optoelectronics system

Integrating external photonic structures with 2D material based optoelectronics is a novel strategy to broaden the horizon of applications for both 2D materials optoelectronics and photonic structures. Those metallic and dielectric photonic or nanophotonic structures can be precisely sculpted into various architectures so that light can be scattered, confined, refracted and processed in controllable ways.[102-104] We summarize their performance parameters of photonic structure integrated 2D material optoelectronics in Table 3.1. First, the introduction of photonic structures into 2D optoelectronics can significantly enhance the photoresponsbility. On the other hand, by electrostatically tuning the Fermi level of 2D material, with which photonic structures like waveguides, resonators and cavities are integrated, improved modulation performance can be achieved.

Modulator

Achieving high performance electro-optic modulator by electrostatically tuning 2D materials is one of the motivations to integrate external photonic structures like waveguides,

resonators or cavities with low dimensional material based optoelectronics.[105-108] For example, a graphene based broadband optical modulator is fabricated by placing a 250 nm-thick Si bus waveguide underneath a graphene sheet as illustrated in Figure 3.2b.[106] A 7 nm-thick Al_2O_3 spacer is placed between Si and graphene. The integration introduces several performance improvements: graphene provides strong light-matter interactions and broadband response covering telecommunication bandwidth, as well as mid- and far-infrared spectral regions. Furthermore, modulation of the guided light at frequencies over 1GHz is demonstrated by electrically tuning the Fermi level of the graphene. Ring shape silicon microring resonators and photonic crystals cavities and other photonic crystal – low dimensional material hybrid systems are also reported in previous literatures.[105, 107, 108]

Table 3.1 *Photonic structure integrated 2D material optoelectronics*

Application	**Photonic structure**	**Material**	**Photonic structure detail**	**Photodetection/Modulation**	**Ref**
Modulator	Waveguide	Graphene	Si bus waveguide	Modulation: > 1 GHz 1.35 to 1.6 μm	[106]
			Si Microring Resonator	Modulation depth: 12.5 dB	[105]
	Photonic Crystal		Nanocavity	Modulation depth: 6 dB	[108]
				Modulation depth: 10 dB	[107]
Photodetector	Plasmonic nano-structure	MoS_2	Au antenna array	Photoresponsivity: 5.2 $A \cdot W^{-1}$	[109]
		Graphene	Au partical	EQE: 1500%	[110]
			Ti/Au nanostructures	2000% enhancement	[111]
	Waveguide	BP	Si bus waveguide	Photoresponsivity: 657 $mA \cdot W^{-1}$ response rate: 3GHz	[48]
		Graphene		Photoresponsivity: 0.1 $A \cdot W^{-1}$, response rate: 20 GHz	[38]
				All optical communication bands	[112]
			Suspended Si membrane waveguide	Photoresponsivity: 0.13 $A \cdot W^{-1}$	[113]

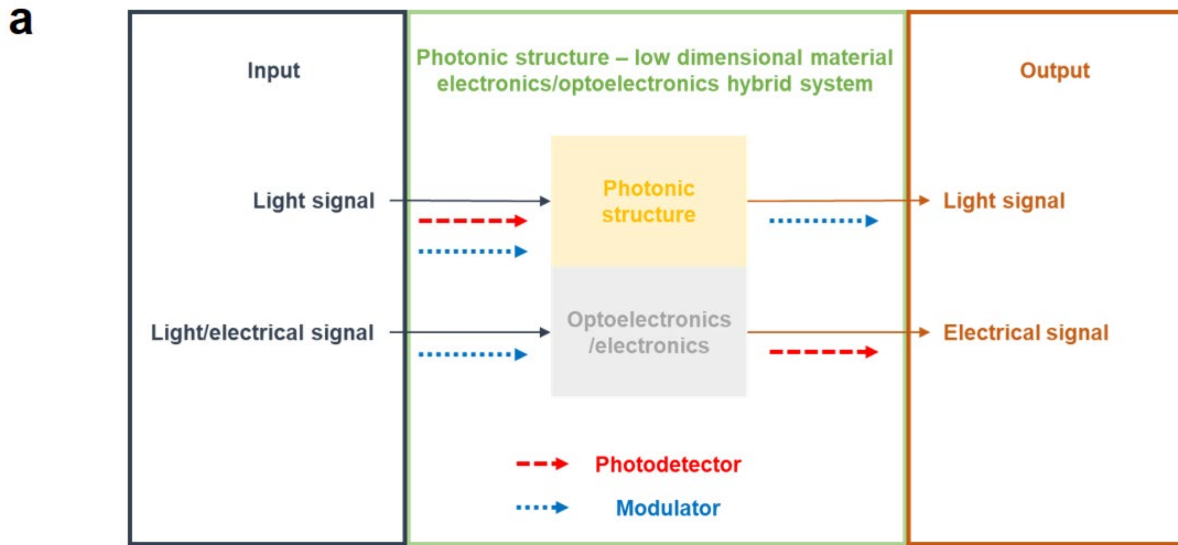

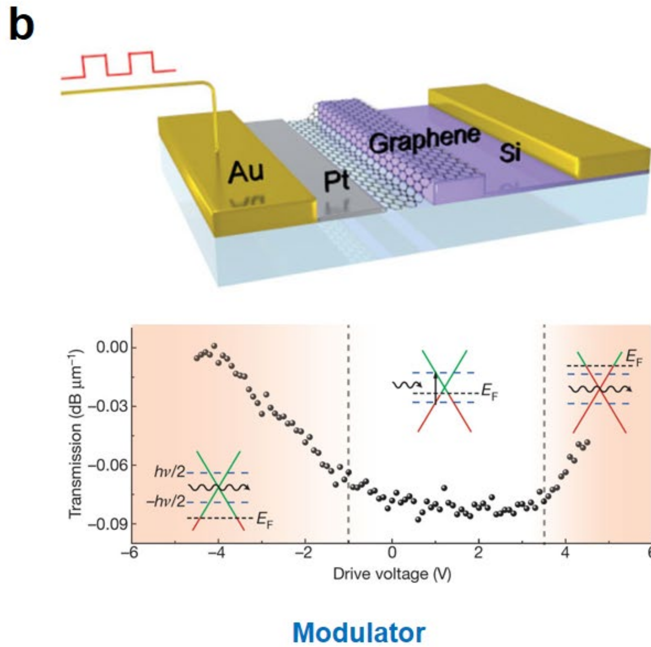

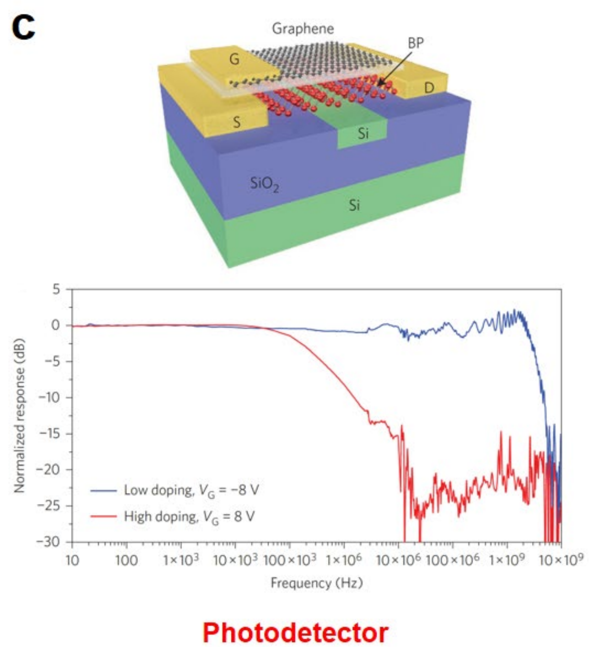

Figure 3.2 *Photonic structure - low dimensional material electronics/optoelectronics hybrid system as modulator and photodetector. (b) Schematic of a high-bandwidth graphene integrated silicon waveguide modulator. Underneath (top) and the modulation depth, normalized to the device length (40 μm), at different drive voltages (V_D)(bottom). Reproduced with permission from ref.[106], with permission from American Physical Society Nature Publishing Group (c) 3D illustration of a silicon waveguide integrated BP photodetector, featuring a few-layer graphene top-gate (top) and broadband frequency response of the BP photodetector with low or high doping (bottom).). Reproduced with permission from ref.[48], with permission from American Physical Society Nature Publishing Group*

Photodetector

Another motivation for integrating external photonic structures with low dimensional material, especially 2D material based photodetectors is to enhance the light absorption in 2D materials. It is known to us that 2D material can have remarkably high single-pass absorption.[7, 36] However, most light will still transmit through the thin layers as the total thickness is below tens of nanometers. Therefore, the light-matter interactions must be further enhanced before it can be used in practical applications, especially for light detection. The combinations of plasmonic nanostructures with 2D materials are first studied to enhance light-matter interactions. Placing metallic objects by an ordered array with dimension and pitch in the order of the excitation wavelength is a classic way to form plasmonic nanostructures. Either stacking 2D materials on top of those plasmonic nanostructures, or patterning plasmonic nanostructures on top of 2D materials can increase the light absorption at certain wavelengths.[110, 111, 114-118] On the other hand, a direct contact between 2D materials and metals enables hot electron injection over Schottky barriers.[109]

Photonic waveguides are another type of photonic structures that have been extensively studied to be combined with 2D optoelectronics to achieve high performance photodetectors. Instead of top coupling, the incident light can be guided into the 2D photodetector by a waveguide through side coupling in order to achieve high responsibility and fast response rate. In a recent report, a silicon waveguide integrated BP phosphorus photodetector has been demonstrated.[48] Compared with graphene, the narrow bandgap nature allows BP operating in the near-infrared band and at the same time preserving low dark current. As shown in Figure 3.2c, a silicon waveguide is planarized by SiO_2 to accept an exfoliated BP thin layer. A graphene gate is then fabricated to control the doping of BP to optimize the device performance. The 11.5 nm thick BP

device has obtained an intrinsic responsivity up to 135 mA/W, and an even higher responsivity up to 657 A/W has been observed for 100 nm thick BP. Also, a high response speed ~ 3GHz has been achieved while the dark current is limited to 220 nA. Graphene - silicon waveguide hybrid systems have also been demonstrated to present high responsivity exceeding 0.1 A/W with response rates exceeding 20 GHz,[38] or to present ultra-wideband response covering all optical communication band with a high speed ~18 GHz.[112] Moreover, the silicon waveguides membrane can be further suspended to improve the performance of silicon waveguide integrated 2D material based photodetector.[113]

3.3 Visualizing light scattering in silicon waveguides with BP photodetectors

Although overall high performances are demonstrated in these photonic structures integrated photodetector systems, few details about the light-matter interactions are comprehensively studied. With the assistance of scanning photocurrent imaging, 2D material-based photodetectors can provide a spatial-resolved mapping of the photoresponse, and thus make it possible to visualize how the local light is affected by the photonic structures.

Here we integrate a few-layer BP photodetector on top of a silicon waveguide to investigate its light-scattering patterns. The silicon waveguide was fabricated by electron-beam lithography on a silicon-on-insulator (SOI) wafer with a 3 μm buried oxide layer and a 220 nm silicon layer. A few-layer BP flake was mechanically exfoliated from its bulk crystal and then transferred onto the silicon waveguide (Figure 3.3a). A composite scanning electron microscopy (SEM) image of half of the silicon waveguide before (left) and after (right) integration with the BP photodetector are displayed in Figure 3.3b to present the zoom-in detail of the waveguide. An array of 40 circular air holes with various radii from 100–125 nm perforates the 700 nm wide ridge waveguide. For our device, the two holes in the center have a 125 nm radius, the holes on both their left and right

sides linearly taper to 100 nm over ten holes, and the final ten adjacent holes on each side maintain the 100 nm radius. The pitch between each hole is 350 nm, and the length of the entire hole array is ~ 14 μm. The thickness of the BP flake was determined to be 9.2 nm by a Park-Systems XE-70 noncontact atomic force microscopy. An encapsulating layer of 200 nm poly(methyl methacrylate) (PMMA) was then coated to minimize the effect of crystal degradation. Source and drain contacts were fabricated by electron-beam lithography and the subsequent deposition of 5 nm Ti and 40 nm Au. Figure 3.1c presents the optical image of the device, in which the position of the air-hole array is marked by a white dashed rectangle.

In order to learning the local light-matter interactions in this BP-silicon waveguide system, scanning photocurrent microscopy was utilized to record the photocurrent signals as a function of position. Figure 3.3d shows the reflection image of the device under 650 nm illumination. By correlating the metal edges in the reflection image to those in the corresponding optical image (Figure 3.3c), the position of the air-hole array on the silicon waveguide was precisely located (outlined by green dashed line in Figure 3.3d). Note that x and y denote the directions parallel and perpendicular to the edge of the waveguide, respectively (Figure 3.3c), where the origin corresponds to the array center.

When the polarization direction of the incident laser was along the x direction as shown in Figure 3.3e, strong photocurrent signals are observed in the positions where the reflection signals are weak, indicating an enhancement of light absorption. Here, all experiments were performed in high vacuum (1×10^{-5} Torr). By aligning and comparing the photocurrent signals with the SEM image, we notice that within the air-hole array region, both photocurrent and reflection signals vary significantly along the waveguide; however, these signals become relatively stable in the region without the holes. As a result, the two edges of the air-hole array can be easily identified in

the photocurrent mapping at $x = \pm 7$ μm. Our experimental results suggest that the reflection and photocurrent signals of the BP flake may be closely related to the light-scattering patterns of the waveguide, which are strongly modified by the circular air-hole array on the nanobeam. Note that while light is traditionally coupled into photonic crystal nanobeams by edge-coupling, our results show that there is light-matter interaction in the nanobeam when laser light is incident from the top and that photocurrent signals from the BP flake can help to map out this interaction.

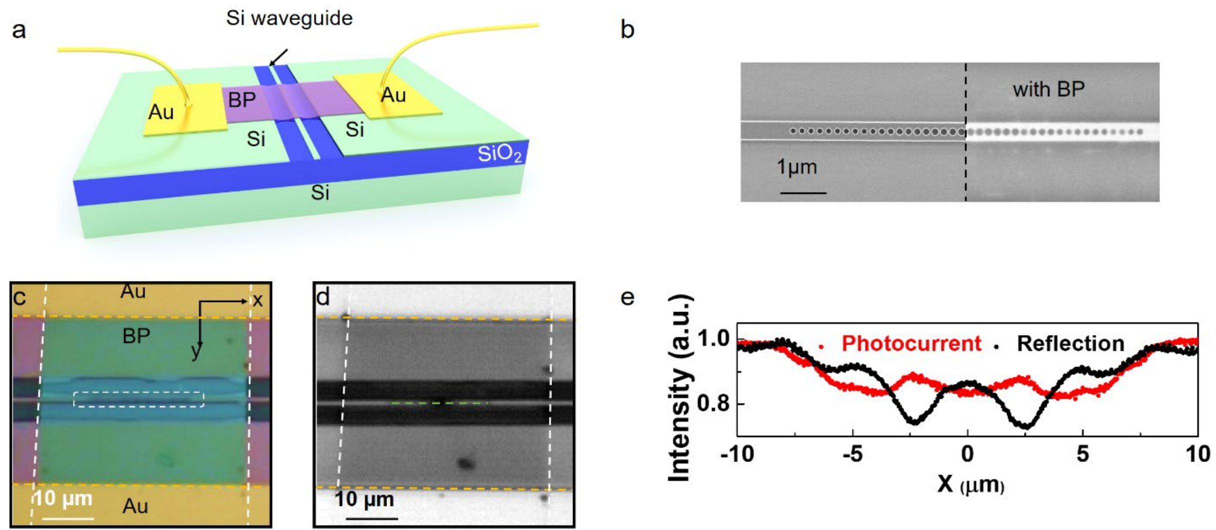

Figure 3.3 *Photonic silicon waveguide integrated BP photodetector. (a) Three-dimensional illustration of the device configuration. (b) SEM image of the silicon waveguide before (left panel) and after (right panel) integrated with the BP photodetector. (c) Optical image of the complete device, where the edges of gold electrodes and the few-layer BP flake are outlined by gold and white dashed lines, respectively. X and y denote the directions parallel and perpendicular to the waveguide, respectively. (d) Reflection image of the device under 650 nm illumination, where the gold electrodes and BP flake are outlined by gold and white dashed lines, respectively. (e) Reflection (black) and photocurrent (red) signals along the green cut line in (d), when the incident laser polarization follows x direction. Reproduced with permission from ref.[119], with permission from John Wiley and Sons*

3.4 Polarization-dependent photocurrent mapping

To elucidate various light-scattering patterns of the silicon waveguide, we performed polarization-dependent photo current measurements under 650 nm illumination. As shown in

Figure 3.4, when the polarization direction of the incident laser changes from the *y* direction (90°) to the *x* direction (0°), the broad photocurrent peak in the middle region of the waveguide splits into four separated peaks along the waveguide. We have found that the scanning photocurrent response measured by the BP photodetector is similar to the electric field intensity distribution of the waveguide predicted by finite-difference time-domain (FDTD) simulations, in which the electric field intensity in the middle region of the waveguide becomes stronger when the incident laser polarization changes from the *x* direction to the *y* direction (Figure 3.4, left and right panels). Our results indicate that the local light scattering patterns induced by the silicon waveguide can be visualized through the BP photodetector as photocurrent signals.

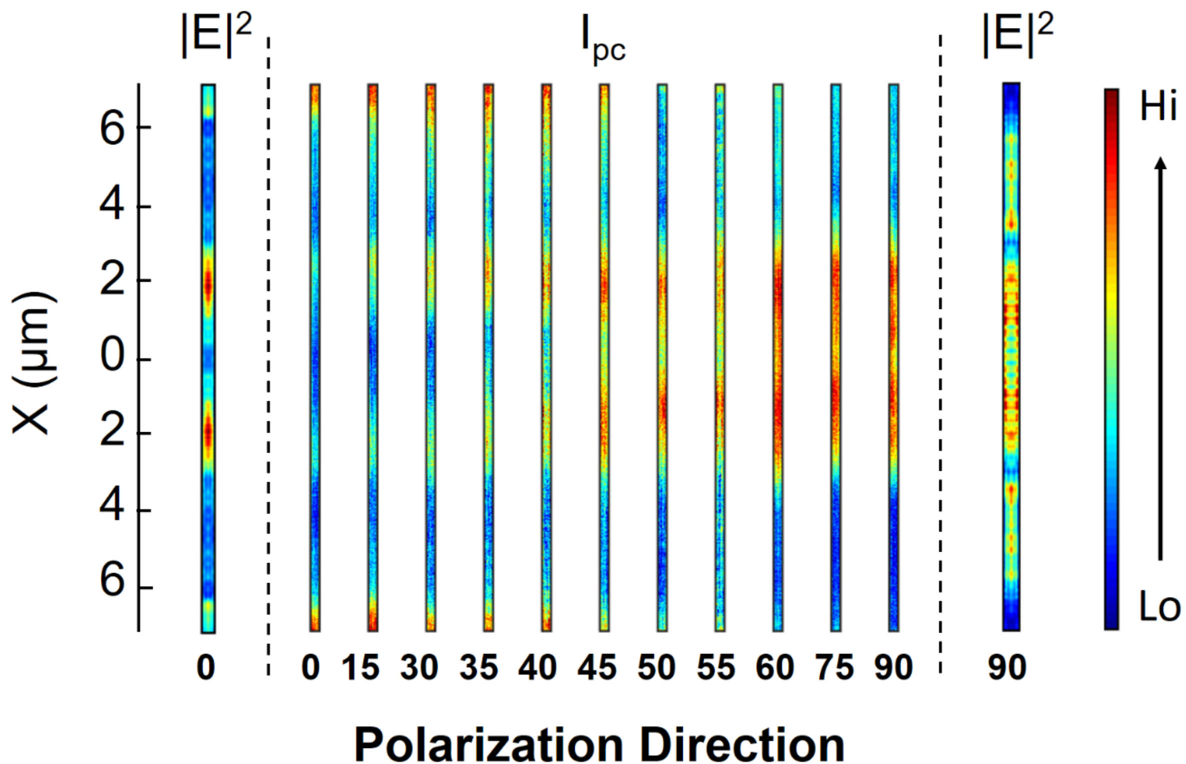

Figure 3.4 *Polarization-dependent scanning photocurrent mappings and corresponding FDTD simulations.Photocurrent images under 650 nm illumination with different polarization directions (middle panel) and the electric field intensity mapping calculated by FDTD simulations for 660 nm illumination when the incident light polarization follows the x direction (left) and y direction (right), respectively Reproduced with permission from ref.[119], with permission from John Wiley and Sons*

3.5 Wavelength-dependent photocurrent mapping

Moreover, we performed wavelength-dependent scanning photocurrent measurements of our device under illumination with laser wavelengths ranging from 620 to 760 nm. The 15 μm-long scanning line covers the entire air-hole array of the waveguide as shown by a green dashed line in Figure 3.3d. In order to keep the number of incident photons equal among different wavelengths, the scanning photocurrent mapping is normalized by Planck–Einstein relation, $n = E/h\nu$. As illustrated in Figure 3.5a and 3.5b, the photocurrent signals present strong wavelength and polarization dependence. Under 620 nm illumination, the photocurrent signals maximize at both the edgeand the center regions of the air-hole array when the incident laser polarizes along the x direction. As the wavelength of the incident laser increases to 680 nm, the central photocurrent peak splits into two peaks which gradually move to the two edges of the air-hole array. Similar photocurrent patterns are observed when the wavelength varies from 680 to 760 nm. For the laser polarization along the y direction, when excited by photons with a wavelength of 620 nm, photocurrent peaks are observed in both edge and central regions, but the central peak is wider and stronger than the edge ones. When the wavelength of the incident laser increases, the photocurrent signals at the two edges become negligible, while the central peak broadens and finally splits into two peaks near $x = \pm 5$ μm at 670 nm. When the wavelength increases, the photocurrent signals maximize again in the central region at 680 nm and two broad and strong photocurrent peaks are detected in the regions near $x = \pm 5$ μm at 730 nm. When the laser wavelength varies from 730 to 760 nm, photocurrent valleys are observed and split from the center to the two edges.

To better understand the different light-scattering patterns while the wavelength and polarization direction of the incident light change, we calculated the electric field intensity of the

silicon waveguide as a function of wavelength along the scanning line by FDTD simulations (Figure 3.5c and Figure 3.5d). After blue shifting the simulation results by 10 nm, the calculated electric field intensity dispersions are in good agreement with the measured photocurrent patterns. In particular, photocurrent signals exhibit the same trend when the strongest electric field peak moves from the center to the two edges. The small offset and slight differences in detailed features of the measured photocurrent and simulated electric filed likely result from fabrication imperfections of the photonic structures, the native oxide layer between BP and silicon, and PMMA layer thickness variation.

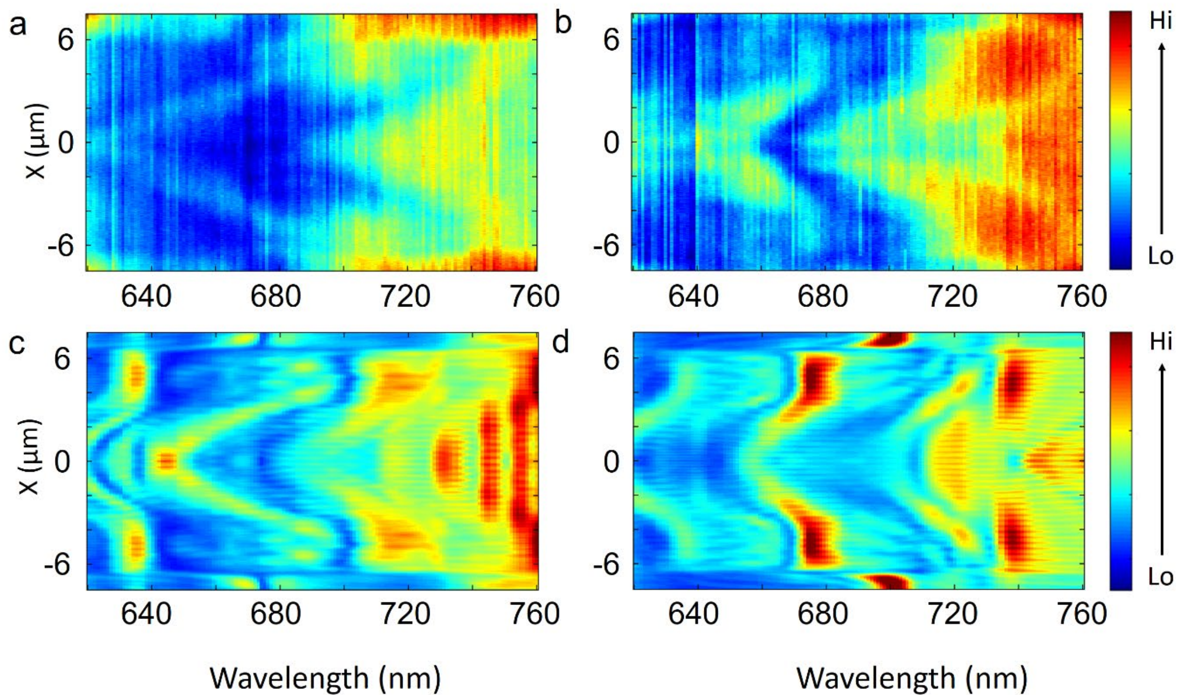

Figure 3.5 *Wavelength-dependent scanning photocurrent mappings and corresponding FDTD simulations.Wavelength-dependent scanning photocurrent images for wavelengths varying from 620 to 760 nm when the incident laser polarizes along (a) x and (b) y direction, respectively. The laser scanning position is indicated by the green dashed line in Figure 3.3d. The FDTD simulated electric field intensity along the same section of the waveguide as a function of wavelength from 620 to 760 nm when the incident laser polarization follows the (c) x and (d) y direction, respectively. Reproduced with permission from ref.[119], with permission from John Wiley and Sons*

In comparison with the experimental data, FDTD simulation results provide a more quantitative analysis of the light-scattering patterns. These patterns suggest that the light-intensity distribution is strongly wavelength- and polarization-dependent owing to the significant modification of the resonant and scattering modes by the waveguide. When the incident laser wavelength and polarization vary, a series of optical modes can be detected by the BP photodetector through scanning photocurrent measurements. However, when the incident laser wavelength goes to the near infrared range, it is difficult to observe small features predicted by FDTD simulations in the photocurrent mapping since the size of the diffraction-limited laser spot becomes much larger than that of the air holes. Furthermore, the relatively wide bandwidth of our laser beam (ranging from 5 to 10 nm) also leads to some differences between the simulated and experimental results, where the small pattern transitions predicted in the simulation are overshadowed in the photocurrent measurements. Despite these limitations, our scanning reflection and photocurrent measurements have clearly demonstrated that the integrated BP photodetector can efficiently map the light-scattering patterns of the silicon waveguide, providing a practical method to directly measure the optical modes of waveguides in supplement to numerical simulations. Moreover, by optimizing the geometric parameters of the waveguide, such as the size and number of the circular air holes, 2D material based optoelectronics with enhanced photocurrent responses at a certain designed wavelength or position can be achieved.

3.6 Photocurrent generation mechanism

Based on all results above, it's now essential to understand the photocurrent generation in the BP - silicon waveguide system. We first considered the two photothermal effects, which are described in Chapter 1.4. Within the area we detected (BP in contact with the silicon), the BP channel is uniform, as a result, the Seebeck coefficient difference is negligible so that the

photocurrent generation form PVE can be neglected. We then move to PBE, where $I_{PBE} = \Delta G \cdot V_{ds}$. The ΔG is extract from the Figure 3.6a to be positive, therefore, the polarity of I_{PBE} is expected to be the same as that of the drain-source current and the I_{PBE} should scale linearly with V_{ds}. However, as shown in Figure 3.6b, the photocurrent response I_{pc} does not scale linearly with V_{ds}, suggesting that the PBE may be not dominant. Interestingly, we found that when the incident photon energy is below the silicon bandgap, there is no photocurrent response observed in the area on top of the waveguide (Figure 3.6c), suggesting that the photocurrent signals are close related to the silicon absorption.

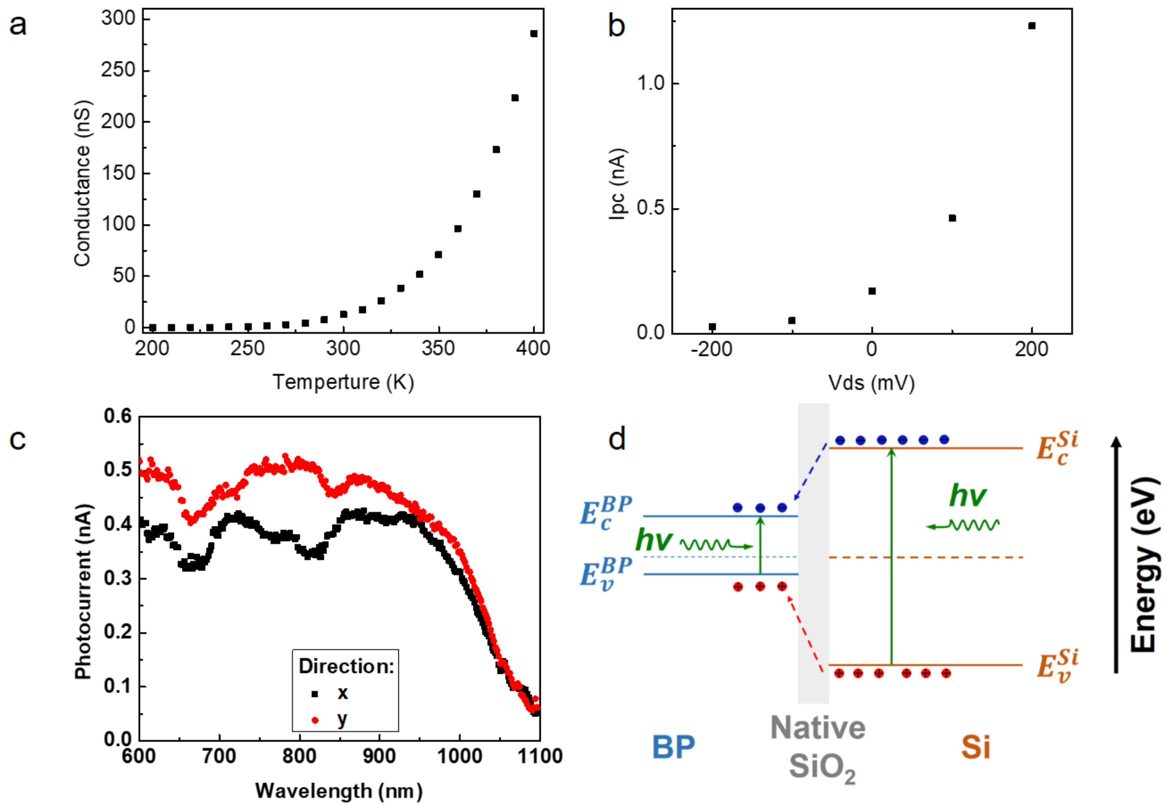

Figure 3.6 *Photocurrent generation mechanisms: electron/hole injection from silicon to BP. (a) Conductance of BP device as a function of temperature. (b) Photocurrent response of BP as a function of drain-source bias. Photoresponse of BP at the center of the silicon waveguide as a function of the incident laser wavelength. The incident laser is polarized along the x (black squares) and y (red circles) directions, respectively. (d) Schematic diagram illustration of the photo-excited EHPs injection from the silicon waveguide to the BP photodetector. Reproduced with permission from ref.[119], with permission from John Wiley and Sons*

As illustrated in Figure 3.6d, when the waveguide integrated BP device is excited by laser with a photon energy larger than the bandgap of silicon, the electrons in the valence bands of both silicon and BP can be excited to their conduction bands. Since the bandgap of BP (0.3 eV) is much smaller than that of silicon (1.1 eV), the valence (conduction) band of BP is much higher (lower) than that of silicon as a result of the Fermi level alignment. Therefore, the photo-excited EHPs can penetrate through the native oxide layer on the silicon surface, inject into BP, and consequently induce photocurrent signals in the BP photodetector.[65, 120] The density of photo-excited EHPs depends on the silicon absorption I_{ab}, which is proportional to the energy flux and is related to its respective electric field intensity through the time-averaged Poynting vector: $I_{pc} \sim I_{ab} \sim \langle S \rangle \sim |E|^2$. Here the photo current response from BP itself is negligible since the light absorption of BP is significantly limited by its innate thinness.

3.7 Conclusion

In summary, we fabricate a few-layer BP photodetector on top of a nanostructured silicon waveguide. In comparison with the numerical simulation, the scanning photocurrent mapping visually reveals the light-scattering patterns of the waveguide. We also study the optical properties of the waveguide under different laser polarizations. A photocurrent pattern transition is observed with various laser polarizations, which is in good agreement with the simulated light-scattering patterns of the waveguide. Additionally, wavelength-dependent scanning photocurrent measurements are performed along the waveguide under laser illumination ranging from visible to near infrared region. The measured photocurrent signals show a pattern similar to the light-scattering patterns predicted by FDTD simulations. Our fundamental studies provide a new approach for investigating the optical properties of photonic structures which are sensitive to the

wavelength and polarization direction of incident light. By adjusting the geometric parameters of photonic structures, 2D material based optoelectronic devices with enhancement or depression at a specific wavelength and polarization can be easily designed and tested to meet the requirements of various applications.

3.8 Methods

Device Fabrication

The photonic structures were fabricated on SOI wafers with a 3 μm thick buried oxide layer (SOITEC). The thickness of the silicon device layer was 220 nm. The wafers were cleaved and coated with a 300 nm ZEP520A photoresist (6000 rpm for 45 s). Electron-beam lithography was performed using a JEOL 9300F tool at 100 kV and 400 C cm^{-2}. Following exposure, the samples were developed in xylene for 30 s and rinsed thoroughly with isopropyl alcohol. The photoresist pattern was then transferred into the silicon layer by reactive ion etching (Oxford PlasmaLab 100) using $C_4F_8/SF_6/Ar$ gases to completely etch the exposed portion of the silicon layer. Few-layer BP flakes were produced by mechanical exfoliation of their bulk crystals on the Polydimethylsiloxane (PDMS) stamp. Thin BP flakes were then identified and characterized by optical microscopy. After that, a selected BP thin flake on the PDMS stamp was placed on top of the silicon waveguide using a home-built transfer stage. BP photodetector devices were fabricated using standard electron-beam lithography and subsequent electron-beam deposition of 5 nm of Ti covered by 40 nm of Au. Finally, the device was coated by 200 nm PMMA to protect BP from degradation.

FDTD Simulations

The numerical simulations were carried out with 3D FDTD analysis using Lumerical FDTD (Lumerical Solutions Inc.). A 10 nm BP layer was placed on top of a nanostructured silicon

waveguide with air holes. The refractive index of BP was chosen to be 2.4.[121] A finer mesh region was defined with a 2.5 nm mesh grid for the BP layer to resolve its 10 nm thickness. The PMMA thickness was defined with a thickness of 200 nm with refractive index n = 1.47. A plane wave light source was defined 2 μm above the photonic structure. A field profile monitor was defined at the interface between silicon and BP. A reflection monitor was placed 0.5 μm above the source to collect back the reflected light

Chapter 4 Tunneling Effect between Crossed van der Waals $Ta_2Pt_3Se_8$ and $Ta_2Pd_3Se_8$ Nanoribbon Junctions

4.1 $Ta_2Pt_3Se_8$ and $Ta_2Pd_3Se_8$

$Ta_2Pd_3Se_8$ (TPdS) and $Ta_2Pt_3Se_8$ (TPtS), which belongs to isostructure group of $M_2X_3Se_8$ (M = Ta or Nb; X = Ni, Pd, or Pt), are frist reported by Keszler et. Al. As shown in Figure 4.1a, (note here, TPdS is taken as an example), TPd/PtS fundamental molecular ribbon (along the c-axis) consists of Ta-centered edge-sharing Se trigonal prisms that are jointed at the ribbon midline and capped at the two sides by Pd/Pt atoms.[122, 123] The binding between the edge-terminating Pd atoms and trans-Se, which is demonstrated to be weak vdW binding in the following studies, provides the force to bond chains to each other. High-quality needle-like bulk TPd/PtS crystals can be synthesized using a chemical vapor transport (CVT) method with an average length was about 1 cm (Figure 4.1 b inset: optical image) and can be further separated easily into microscopically thin wires if pressed between two microscope slides (Figure 4.1 b: SEM image). The spatial distribution of charge density simulation further studies the crystal structure of TPd/PtS as shown in Figure 4.1c. The inter-chain bonding shows an energy of 0.34 eV/atom, which is 17 times smaller than the average intra-chain bonding with an energy is about 5.7 eV/atom. The weak vdW inter-chain bonding offers an opportunity to obtain 1D or quasi 1D vdW nanowires/nanoribbons directly via mechanical exfoliation.

Previous studies have demonstrated TPd/PtS nanowire-based FET with mobility around 80 $cm^2 V^{-1} s^{-1}$, ON/OFF ratio above 10^4 and current capacity comparable to silicon nanowires.[124] TPd/PtS show semiconducting properties with layer dependent bandgap from indirect 0.53 eV in multiribbon to direct 1.04 eV in a single ribbon. More attractively, TPdS nanoribbons appear to be

n-type semiconductors, while TPtS nanoribbons show *p*-type behaviors, enabling to form a crossed *p-n* junction by stacking them together. Furthermore, two atomically-thin quasi-1D semiconductors are bonded by vdW force with nanoscale confinement. Therefore, interlayer transition and many novel electrical and optoelectronic properties are expected to happen.

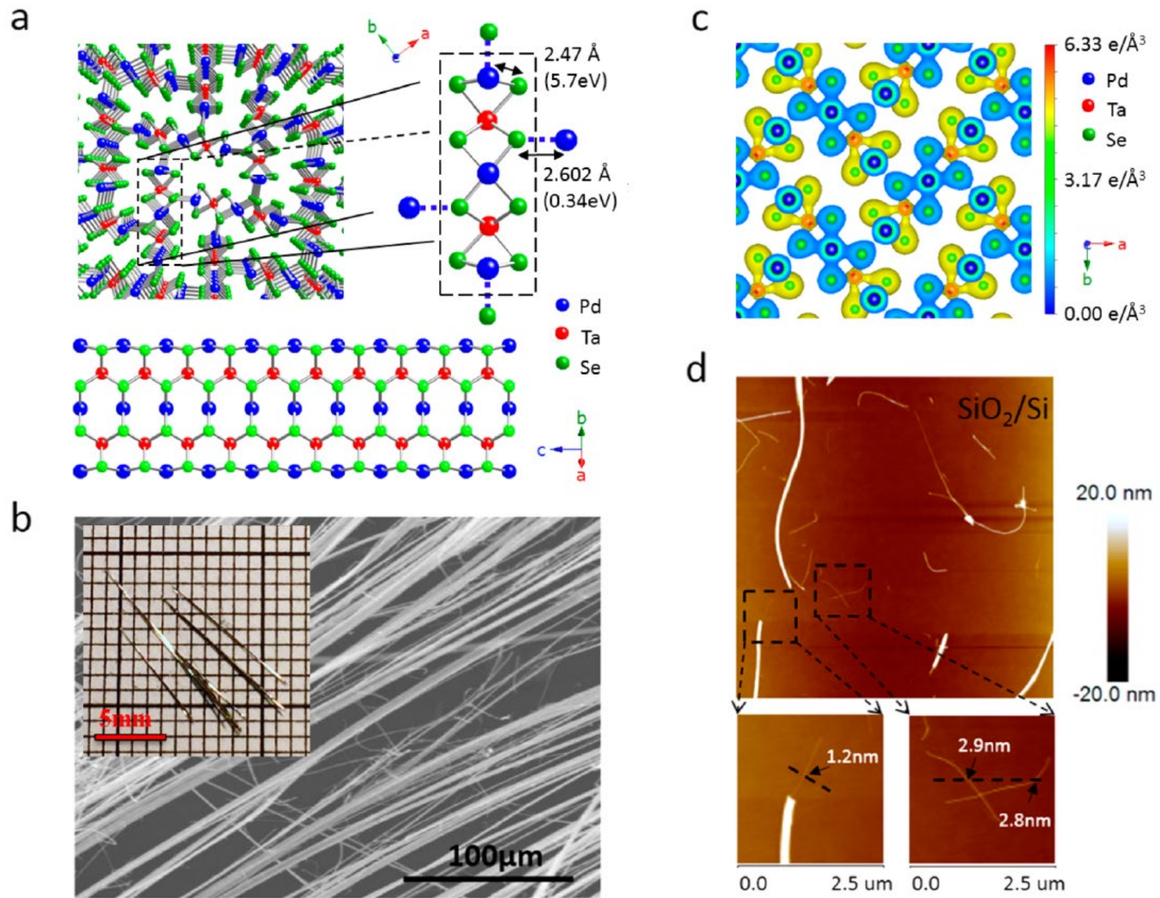

Figure 4.1 *TPdS: crystal structure, SEM and AFM images. (a) TPdS crystal structure. Top left: perspective view of bulk TPdS projected along the c-axis. Top right: cross section view of a single ribbon (inside the dashed rectangle). The length and bonding energy for intra (solid line) and inter (blue dashed line) bonds are 2.47 Å/5.7 eV and 2.602 Å/0.34 eV, respectively. Bottom: top view of a single ribbon that extends along the c direction. (b) Scanning electron microscope image of the bulk crystal. The inset shows the as-grown needle-like single crystals. (c) Isosurface map (set at 0.05 e/Å3) of the simulated spatial distribution of charge density (001 surface), the positions of Pd, Ta, and Se atoms are indicated by blue, red, and green spheres, respectively. (d) AFM images of TPdS nanowires prepared by micromechanical exfoliation. Extremely thin nanowires (1.2, 2.8, and 2.9 nm) can be found in two highlighted regions. Reproduced with permission from ref.[124], with permission from American Chemical Society*

4.2 Low-dimensional material transfer methods

For the most basic low-dimensional vdW material FET, the thin flakes or wires can be directly cleaved on to a SiO_2/Si, followed by EBL and metallization to provide electrical connection. This method is straightforward but has disadvantages: first, the flakes/wires that are sensitive to the environment can easily degrade. Also, SiO_2 not an ideal substrate due to its charged surface states, impurities, optical phonons and surface roughness. Using another thin vdW material film as a protection layer or substrate is a promising solution to above problems, which can provide ultra-clean and ultra-smooth encapsulation with minimal damages to the target flakes/wires. Adding either a protection layer or a substrate involves transfer. Here, the transfer usually means the process of moving one piece of thin flake from one material surface to another material surface. By using the transfer method, research successfully encapsulated graphene with BN and achieved very high quality. Encapsulation is the start but not the limit of the transfer. In the past decades, different transfer methods are widely used to build different kind of low dimensional vdW material based heterostructures or heterojunctions.

Figure 4.2 displays process flows of three widely used transfer methods. To make the case simple, here we take heterostructures consisting of two materials as an example. Heterostructures that involve more materials can be achieved by repeat some steps of the whole process. The process starts from flake 1 on substrate 1 and flake 2 on substrate 2, and the target is that the flake 1 is properly aligned with flake 2 on substrate 2. The process involves three main steps: i: separate flake 1 from substrate 1; ii Align flake 1 to flake 2 on substrate 2 and iii, remove the transfer stamp that is used in step i and ii.

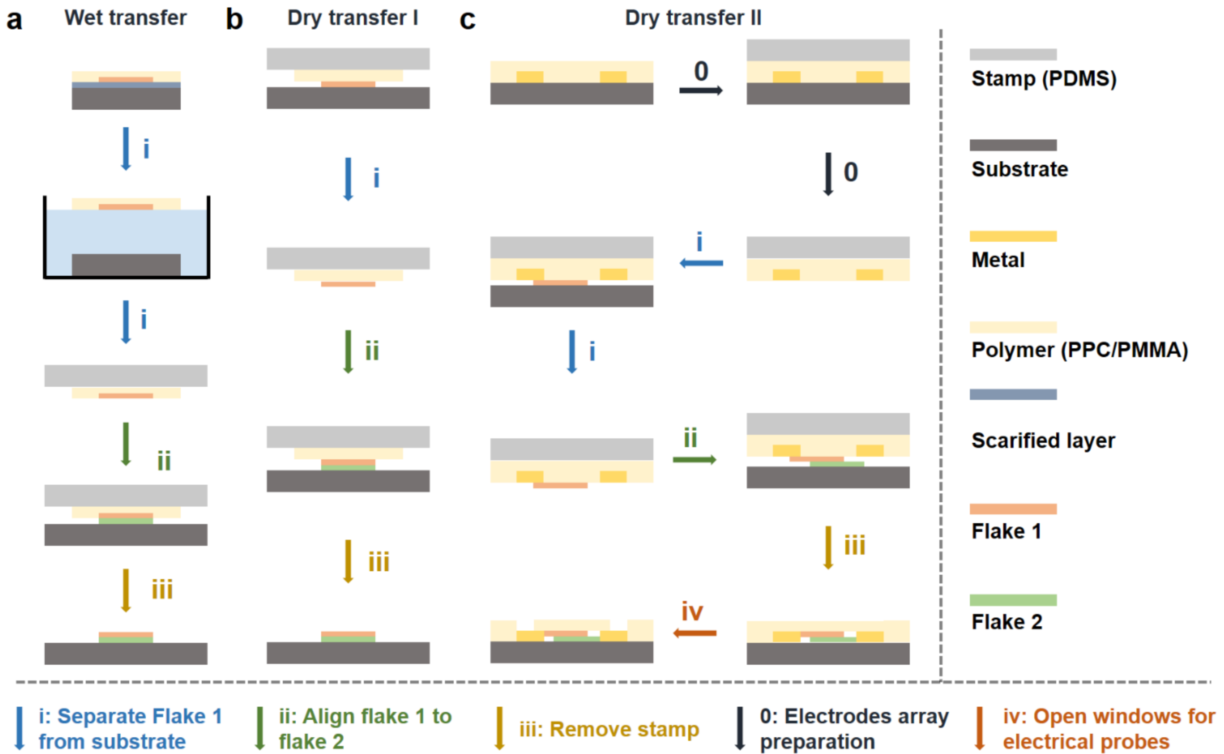

Figure 4.2 *Low dimensional material transfer methords. (a) process flows show (a) wet transfer, (b)dry transfer I and (c)dry transfer II.*

As shown in Figure 4.2a, the wet transfer use chemicals to dissolve scarified layer to separated flake 1 from substrate 1. The scarified layer can be the SiO_2 layer of the standard SiO_2/Si substrate which can be etched by KOH. Or the flake 1 needs to be exfoliated onto a water-soluble tape, which will later be dissolved by water. A Polymer coating is needed on the top to support the flake 1 and help the flake to float on the solution after the scarified layer is removed. Then the flake 1/PMMA structure will be mounted on to a stamp and can be precisely moved by a 3-axis manipulator. The flake 1/PMMA/stamp and flake 2 on substrate 2 are carefully aligned through the optical microscope by moving the stamp via manipulator. Further lower the flake 1/PMMA/stamp and make it fully contact with flake 2 on the substrate. Finally heat up the whole stack to make PMMA become very soft and close to melting. At this moment, the manipulator is

moved up slowly and the portion of PMMA touching the substate can separate with the stamp and stay on the substrate. After wet transfer, the PMMA film is rinsed away in acetone and further cleaning can be conducted by annealing. However, due to the wet process in step i, it is extremely difficult to remove all chemical residues and bubbles and wrinkles may exist at the flake 1/flake 2 interface.

The dry transfer method is then introduced to avoid the chemical contamination of the wet transfer method (Figure 4.2b). A viscose poly-propylene carbonate (PPC) film carried by PDMS stamp is utilized to pick up flake 1 from substate 1. During the pick-up, the portion of PPC film first full contact with flake, and then the stack is heated up to around 40 ^{o}C. Under this temperature, the flake 1 can be picked up by PCC by slowly lifting the stamp. Alignment and contact are then conducted between flake 1/PPC/stamp and flake 2 on substrate 2. Finally, raising the temperature to around 90 ^{o}C to soften the PPC, make it remain on the substrate 2 while removing the PDMS stamp. The PPC is then removed in chloroform to leave the flake 1/flake 2 stack on the substrate. Although, chloroform is used in the last step, the flake 1/flake 2 interface should be clean without contamination. Moreover, the pick-up process can be just repeated to build multilayer heterostructures and a BN layer can be first picked up to then protect the whole stack underneath from chemical contamination (chloroform and other chemicals used in metallization).

For most heterostructure devices, the metallization which provides electrical connections is usually the last step of the device fabrication, and involves EBL followed by metal deposition. Recently, researchers propose a new approach for metallization. As shown in Figure 4.2c, metal electrodes are pre-fabricated on bare silicon substrate using standard EBL and E-beam deposition and lift-off process. Then the metal electrodes can be released from the substrate by coating a PMMA layer and peeling off the PMMA layer with the help of a PDMS stamp. The

electrodes/PMMA/PDMS then can be physically laminated onto the target flakes/wires or used to pick up flake 1 and then align to flake 2. After removing the PDMS stamp, PMMA on top of the contact pads is removed using EBL and development processes, leaving the exposed metal pads for further electrical connection.

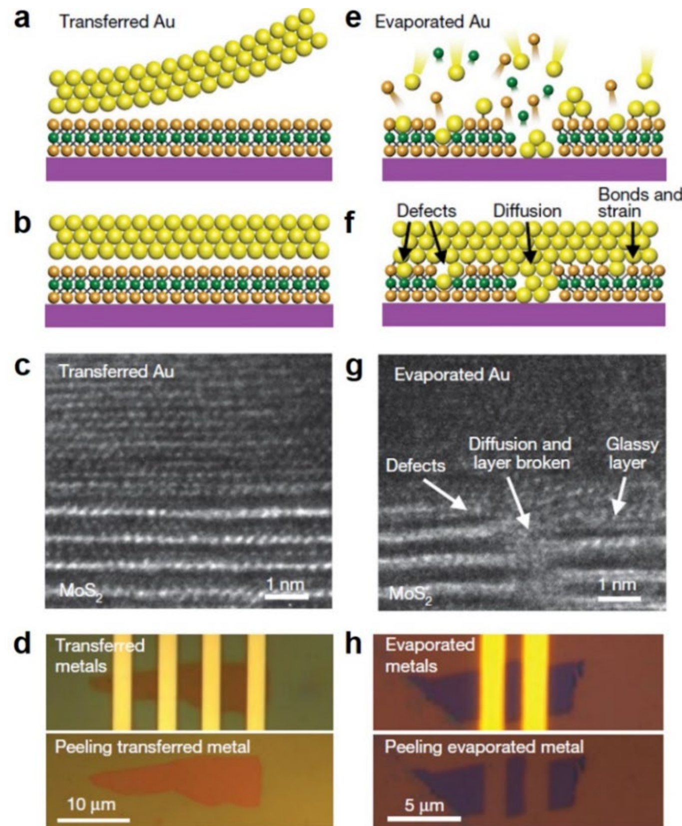

Figure 4.3 *Comparasion between transferred metals and evaporated metals. (a)-(c), Cross-sectional schematics and TEM images of the transferred Au electrode on top of MoS_2, with atomically sharp and clean metal-semiconductor interfaces. d, Optical image of the MoS_2 device with transferred electrodes (upper) and with the transferred electrodes mechanically released (lower). The underlying MoS_2 layer retains its original shape after physical integration and separation of the Au thin-film electrodes, indicating that the transferred metal–semiconductor interface is free of direct chemical bonding. (e)-(f), Cross-sectional schematics and TEM images of conventional electron-beam-deposited Au electrodes on top of MoS2, where the bombardment of the MoS_2 surface by high-energy Au atoms and clusters creates considerable damage to the MoS_2 surface, producing a glassy layer with apparent defects, interface diffusion, chemical bonding and atomic disorder. h, Optical image of a MoS_2 flake with deposited electrodes (upper) and with the deposited electrodes mechanical released (lower), where the underlying MoS_2 surface is destroyed while removing the deposited electrodes, suggesting direct chemical bonding and strong metal–semiconductor interaction in deposited junctions. Reproduced with permission from ref.[125], with permission from American Chemical Society*

As illustrated in Figure 4.3, the physical transfer of pre-fabricated metal electrodes offers a gentle, 'low-energy' materials integration strategy without conventional aggressive fabrication processes such as lithography or deposition, to prevent the creation of defects, residues, strains and the associated defect-induced gap states on a dangling-bond-free 2D semiconductor surface. Both TEM images (Figure 4.3c and g), and optical image (Figure 4.3d and h) showing a MoS_2 flake with metal contacts then be separated mechanically further demonstrate that this method can achieve weak vdW interaction at the interface without damage to underlying semiconductor, allowing Schottky barrier height of a MS junction approaches the Schottky–Mott limit.

4.3 *p-n* junction between $Ta_2Pt_3Se_8$ and $Ta_2Pd_3Se_8$ nanoribbons

We fabricated nanoscale *PN* junctions between *p*-type TPtS and *n*-type TPdS nanoribbons via the vdW transfer technique. Figure 4.4a illustrates the schematic diagram of a typical heterojunction, consisting of a TPdS nanoribbon that is perpendicularly stacked on top of a TPtS nanoribbon and four metal electrodes that are connected to both ends of two nanoribbons, respectively. Here ultrathin TPtS/TPdS nanoribbons were mechanically exfoliated on top of the degenerately-doped Si substrate covered with a 280-nm-thick thermal SiO_2 layer. Optical microscopy was used to identify thin TPtS/TPdS nanoribbons, which with thicknesses less than 50 nm were selected. In order to avoid Fermi-level pinning and chemical disorder at metal-nanoribbon interfaces, a vdW transfer technique was adapted from a previous report to build TPtS-TPdS heterojunctions.[125] Briefly, gold electrodes were first prepared on a silicon substrate and then mechanically released from the substrate by a PMMA layer and a PDMS stamp. Next, the released metal electrodes were carefully aligned and placed atop a TPdS nanoribbon under an optical microscope. The TPdS nanoribbon was then picked up by lifting the PDMS stamp slowly. After that, the PDMS-PMMA-metal-TPdS stack was perpendicularly aligned and physically

laminated on top of a TPtS nanoribbon, subsequently followed by heating and lifting the PDMS stamp. As a result, a PMMA-metal-TPdS-TPtS stack with clean metal-nanoribbon and nanoribbon-nanoribbon interfaces was placed on the SiO_2/Si substrate. Finally, a standard electron-beam lithography process was conducted to remove the PMMA atop contact pads, providing exposed metal pads for future electrical and optoelectronic measurements. The inset of Figure 4.4a presents an optical image of a typical TPtS-TPdS heterojunction. Back-gate voltages were applied to the nanoribbons through a 280 nm SiO_2 layer. Both electrical and optoelectronic properties of the device were characterized in a Janis ST-500 Microscopy Cryostat under high vacuum ($\sim 10^{-6}$ Torr).

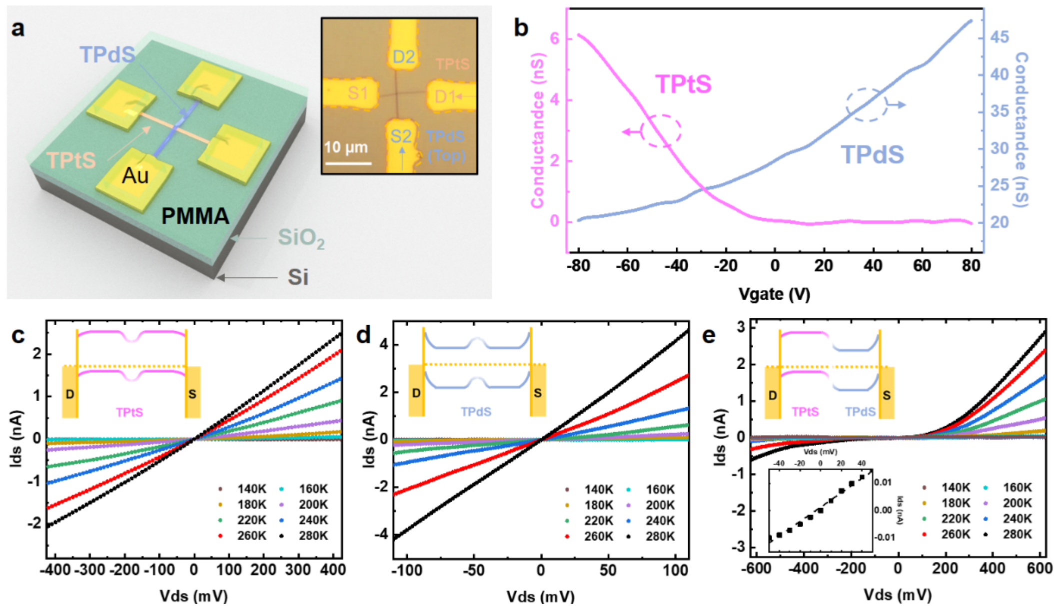

Figure 4.4 *Schematic and electronic characteristics of the TPtS-TPdS junction. (a) A schematic diagram of a nanoscale crossed p-n junction between perpendicularly stacked TPtS and TPdS nanoribbons. Inset: optical micrograph of a typical device. S and D indicate source and drain electrodes, respectively. The gold dashed lines mark the edges of metal electrodes. (b) Gate-dependent characteristics for TPtS and TPdS nanoribbons based FETs.* I_{ds}*-*V_{ds} *characteristics and band diagrams of (c) the TPtS nanoribbon with a gate voltage of -80 V and (d) the TPdS nanoribbon with a gate voltage of 80 V at various temperatures. (e)* I_{ds}*-*V_{ds} *characteristics of the TPtS-TPdS junction with a gate voltage of -80 V at various temperatures. Inset shows low-bias region and its linear fitting.*

Figure 4.4b displays the gate-dependent transport characteristics of individual nanoribbons, where TPdS and TPtS nanoribbons show *n*-type and *p*-type behaviors, respectively. For this typical device, the TPdS nanoribbon exhibits higher electrical conductance than that of the TPtS one, which is likely related to their thicknesses. The TPdS nanoribbon is expected to be relatively thick, since its color is darker than that of the TPtS nanoribbon in the optical image (Figure 4.4a, inset). Moreover, the *I-V* characteristics shows that both TPdS and TPtS nanoribbons possess nearly linear output curves at various temperatures (Figure 4.4c and 4.4d), suggesting ohmic contacts are formed between nanoribbons and metal electrodes. Furthermore, an increase in the conductance is observed for both nanoribbons when the temperature rises from 140 K to 280 K, which is likely due to their semiconductor nature.[126] As illustrated in Figure 4.4e, the *I-V* characteristics of the TPtS-TPdS junction is subsequently investigated. Non-linear rectifying behaviors are observed at various temperatures, suggesting that a *PN* junction is formed at the TPtS-TPdS interface.

4.4 Tunneling effect

TPtS and TPdS share similar indirect band gap around 0.53 eV, while TPtS shows *p*-type and TPdS shows *n*-type behaviors. Once they contact with each other, TPtS is expected to bends downward while TPdS bends upward to align their Fermi levels, resulting in a built-in junction barrier between them as shown in Figure 1e top inset. Forward biases can reduce the barrier and lead to current flow. Under -80 V gate, where TPtS start to turn on and TPdS is going to become off state. The junction potential can be roughly estimated to be around 180 meV to 265 meV, which matches the V intercept (230 meV) of the large-bias linear region of the junction output *I-V* curve under positive bias. Reverse biases increase the barrier but the small depletion region allows tunneling transmission occurs through the barrier and leads to a measurable current flow that increases with increasing reverse bias.

To further illustrate the details, we focus on the transmissions at the TPtS-TPdS interface. The band bending causes depletion regions for two nanoribbons. Therefore, the electrical transmission from one nanoribbon to another, involves two transmissions through the two depletion regions, in addition to the transmission between the two vdW force bonded nanoribbons. According to the previous reported tunneling transmission study about the vdW force bonded carbon nanotube, the transmission probability (T_d) for tunneling through the depletion region, can estimated form the transmission probability ($T_S \approx T_d^2$) along the ribbon, where the depletion region needs to be transmitted twice (inset of Figure 4.4c and 4.4d).[127] T_S can be calculated with the conductance of each ribbon: $T_S = G/(4e^2/h)$ (where e is the electron charge and h is Planck's constant). Similarly, the transmission possibility between TPtS-TPdS junction can also be calculated from the junction conductance at low-bias linear region (Vds < ±50 mV) (Figure 4.4e bottom inset). On the other hand, as we mentioned in previous discussion, the transmission possibility between TPtS-TPdS junction $T_{TPtS\text{-}TPdS}$ can be given by $T_{TPtS\text{-}TPdS} \approx T_{d_TPtS} \cdot T_j \cdot T_{d_TPdS}$. As a result, the transmission possibility between the two vdW force bonded nanoribbons, T_j, can be estimated to be around 0.025 (for another device, Tj is 0.059), which is similar to the reported transmission possibility for the vdW force bonded carbon nanotube (Tj ~ 0.02 to 0.06).[127]

The tunneling transmission between the two vdW force bonded nanoribbons can be interpreted as interlayer recombination between majority carriers of TPtS and TPdS, which can be described by Shockley-Read-Hall (SRH) recombination (inelastic tunneling of majority carriers into trap states in the gap) and Langevin recombination (Coulomb interaction). The increasing interlayer recombination rate at higher forward biases, and the band bending along each nanoribbon under reverse biases lead to the non-linear *I-V* characteristics.

4.5 Polarization-dependent photoresponse

Aside from the electrical transport measurements, the optoelectronic properties of nanoribbons and their heterojunctions were investigated using scanning photocurrent microscopy. Figure 4.5a shows a photocurrent image of the *p*-type TPtS nanoribbon, where the nanoribbon and metal electrodes are outlined by orange and yellow dashed lines, respectively. Strong photocurrent responses are observed at the nanoribbon-metal interfaces, where potential barriers are formed due to Fermi level alignment, leading to built-in electric fields that separate EHPs. The red/blue color corresponds to positive/negative current, where positive current indicates the current flows from the drain to source electrode. For the *p*-type TPtS nanoribbon, since the electronic energies are lower near the contacts than in the middle of the nanoribbon, electrons will flow from the middle channel to electrodes (Figure 4.4c inset), resulting in a positive/negative current flow at the drain/source electrode. When a drain-source bias of 5V is applied, the intensity of the positive photocurrent response at the drain electrode is strongly enhanced. We have also found that the photocurrent response of the TPtS nanoribbon is anisotropic. As shown in Figure 4.5b, the photocurrent signals are maximized when the incident light is polarized along the TPtS nanoribbon direction (or 0°). The direction of the polarization is defined as shown in Figure 4.5a, where 0° and 90° denote the directions parallel to the TPtS and TPdS nanoribbons, respectively. The polarized effect likely arises from the unique chain-like structure of TPtS nanoribbons, which gives the materials their quasi-1D properties. As a result, a smaller part of the incident light is expected to be coupled into the nanoribbons for the cross-polarized light, leading to high anisotropy rations in optical absorption, as reported in other 1D or quasi-1D structures.(48, 49, 59-62) The anisotropic photoresponse of TPtS nanoribbons opens another degree of freedom in development of future polarized optoelectronics.

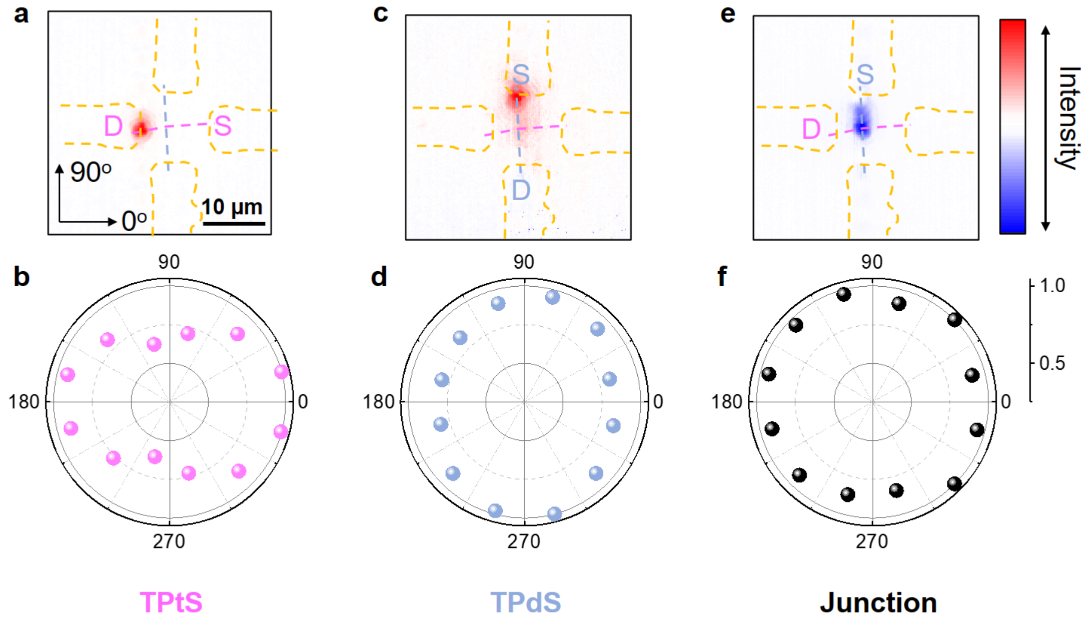

Figure 4.5 *polarization-dependent photoresponse of the TPtS-TPdS junction.Scanning photocurrent images of (a) the TPtS FET (+5V bias), (c) the TPdS FET (+1V bias), and (e) the TPtS-TPdS junction (+5V bias), respectively. Normalized photocurrent intensities as a function of the incident light polarization direction for (b) the TPtS FET, (d) the TPdS FET, and (f) the TPtS-TPdS heterojunction, respectively.*

Similarly, an opposite polarity of photocurrent responses is observed for the *n*-type TPdS nanoribbon at the nanoribbon-metal interfaces (Figure 4.5c), where the electronic energies are higher near the contacts than in the middle of the nanoribbon (Figure 4.4d inset), leading to a flow of electrons from the electrodes to the middle channel or negative/positive photocurrent signals near the drain/source electrode. As we expected, the maximum photocurrent response of the TPdS nanoribbon occurs for the light polarization direction parallel to the nanoribbon (90 oC) (Figure 4.5d). Furthermore, we explore the optoelectronic properties of the TPtS-TPdS *PN* junction. As shown in Figure 4.5e, the majority of photocurrent signals are detected in the overlap region between TPdS and TPtS nanoribbons, where the *PN* junction induced built-in electric field can efficiently separate the photo-excited EHPs to generate photocurrent responses (Figure 4.4e top

inset). Interestingly, the photocurrent signals observed at the TPtS-TPdS junction show nearly isotropic behavior (Figure 4.5f), suggesting both nanoribbons contribute to the photocurrent generation in the junction region. The entire TPtS-TPdS system provides an idea to achieve light detection at a controllable polarized photodetection.

4.6 Bias-dependent photoresponse

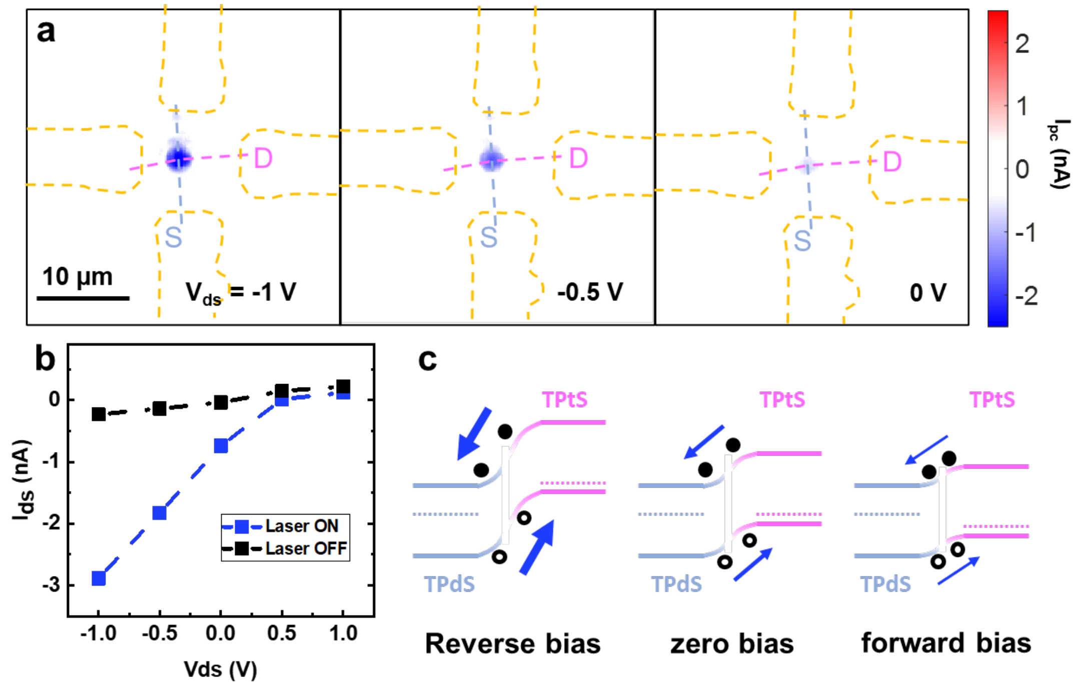

Figure 4.6 *Bias-dependent photocurrent of the TPtS-TPdS junction.(a) Scanning photocurrent images of the TPtS-TPdS junction under different drain-source biases. (b)* I_{ds} *when the drain-source voltage sweeps from -1 V to 1 V with a step of 0.5 V in dark and with laser shine on the junction area. (c) Band diagrams for the TPtS-TPdS junction under different biases.*

To further explore the photocurrent generation mechanisms at the TPtS-TPdS junction, we performed bias-dependent scanning photocurrent measurements under V_{bg} = -80 V (Figure 4.6a and 4.6b). At the zero bias, negative photocurrent signals are detected in the junction region, which is consistent to the negative short circuit current for a conventional *PN* junction via PVE as shown

in Figure 4.6c middle. If a reverse bias is applied (V_{ds} = -1V) that raises the total electrostatic potential and thus facilitate the separation of the photo-excited EHPs. Therefore, the photo-excited carries are quickly separated and then collected before recombined at the interlayer, leading to enhanced photocurrent signals (Figure 4.6c left). On the other hand, the forward bias can partially cancel the built-in electric field or reduce the total electrostatic potential, making it difficult to separate the photo-excited EHPs (Figure 4.6c right). Under this circumstance, interlayer recombination may compete with photo-excited carries separation/collection, leading to negligible photocurrent. This further confirms that the photocurrent response at the TPtS-TPdS junction is mainly attributed to the PVE.

4.7 Photoresponse spectrum for nanowire with various thickness

By varying the wavelength of the incident light, we further explored the spectral response of TPtS and TPdS nanoribbons. Figure 4.7 shows the measured normalized photocurrent signals as a function of the light wavelength (P = 80 μW) for TPtS/TPdS nanoribbons with different thicknesses. We could roughly estimate the bandgaps of nanoribbons by extracting the cut-off wavelength of photoresposivity. A thinner TPtS nanoribbon that shows relatively light color under an optical microscope (Figure 4.7a) tends to have a larger band gap of 1.08 eV (1150 nm), while the thicker one (Figure 4.7b) owns a band gap of 0.99 eV (1250 nm). Similarly, the bandgaps for TPdS nanoribbons are 1.03 eV (1200 nm) and 0.92 eV (1350 nm), respectively. This is in good agreement with the previous electronic band structure calculations, which predict that the bandgaps of TPtS/TPdS are thickness-dependent and there is a transition from 1.038 eV in a single-layer structure to 0.525 eV in bulk material.[124] More accurate measurements of the nanoribbon thickness/width and other bandgap characteristics are required in the future to pin down the relationship between the bandgap and size of TPtS/TPdS nanoribbons.

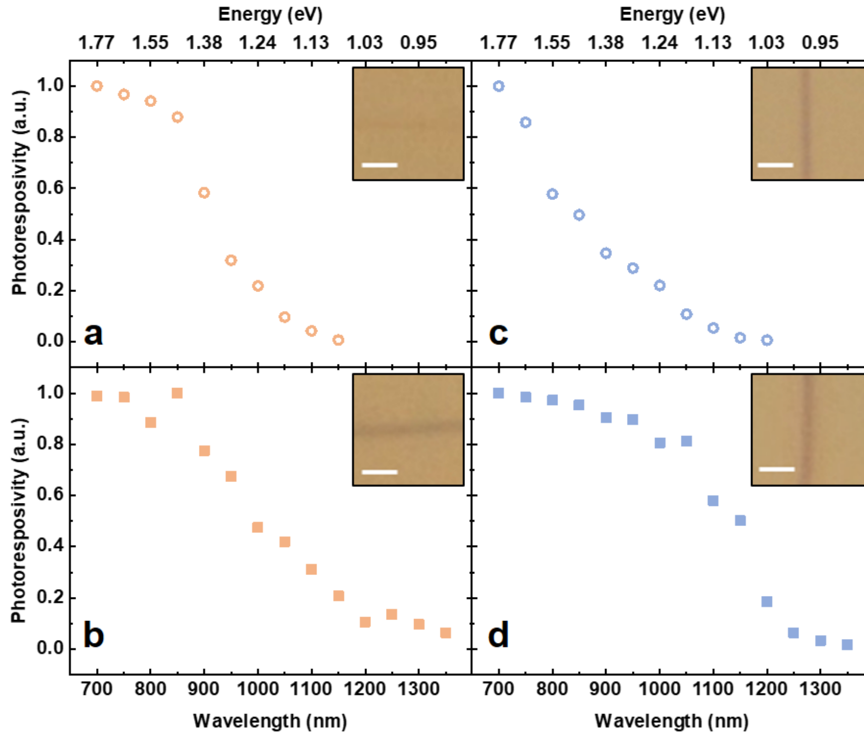

Figure 4.7 *Photoresponse spectrum for nanowire with various thickness. (a) Photocurrent signals measured as a function of incident laser wavelength for TPtS (a and b) and TPdS (c and d) nanoribbons with different thicknesses. Inset: optical images of nanoribbons.*

4.8 Conclusion

In summary, we report nanoscale *p-n* junctions between perpendicularly stacked *p*-type TPtS and *n*-type TPdS nanoribbons. *p*/*n*-type gate-dependency and asymmetric nonlinear output behaviors are successfully demonstrated for the TPtS/TPdS nanoribbons and their heterojunctions, respectively. Following examination illuminates tunneling effect between the crossed vdW nanoribbons junction with transmission possibility around 0.025. Moreover, isotropic photocurrent signals are observed at the nanoscale TPtS-TPdS heterojunction, while TPtS/TPdS nanoribbons exhibit polarized photoresponses, suggesting that the photocurrent signals at the heterojunctions are likely attributed to photo-excited carriers in both TPtS and TPdS nanoribbons. Bias-dependent

photocurrent measurements further demonstrate that the photocurrent generation at the TPtS-TPdS *p-n* junction primarily stems from the PVE, which is similar to conventional *pn* junctions. With the assistance of the photoresponse spectra of TPtS/TPdS nanoribbons, their bandgaps can be estimated to be around 0.9 eV to 1.1 eV and depend on their thickness, consistent to previous theoretical predications. These studies not only offer a way to build nanoscale junctions, but also provide fundamental understandings on the electrionic and optoelectronic properties of vdW nanoribbons and their heterojunctions, opening up new avenues for engineering future anisotropic electronics and optoelectronics.

Chapter 5 Laser Induced Charge Density Wave Melting in Suspended $NbSe_3$ Nanowires

5.1 Charge density wave in $NbSe_3$

$NbSe_3$ belongs to TMTC, where covalently bonded molecular chains are assembled together via vdW force to form quasi-1D crystal structures.[128-131] This restricted dimensionality enables periodic distortion of the lattice in $NbSe_3$ when the temperature drops below a critical value (T_{CDW}), which develops a wave-like variation of the free electron density.[132] This static modulation of conduction electrons is known as charge density waves (CDWs). The monoclinic room-temperature structure of $NbSe_3$ is depicted in Figure 5.1a top inset. Three types of metallic chains are included in the $NbSe_3$ unit cell. The type-III chains are responsible for the first CDW with wavevector q1 (0, 0.243 ± 0.005, 0) below T_{CDW1} = 145 K, and the type-I chains contribute to the second modulation with wavevector q2 (0.5, 0.263 ± 0.005, 0.5) below T_{CDW2} = 59 K, whereas the type-II chains remain metallic at all temperatures.[131, 133-135]

5.2 Raman spectrum and resistance characteristics of $NbSe_3$

$NbSe_3$ nanowires were prepared from bulk crystals using ultrasonic cleaving. Even though the bonding energies along b and c directions in $NbSe_3$ are comparable, the Nb-Se bonds formed along the c direction vary significantly in the bond length (2.73−2.95 Å), which results in an easy cleavage. Raman spectrum is used to identify $NbSe_3$ as shown in Figure 5.1b. $NbSe_3$ layer crystal in the monoclinic phase, which haves space group $P2_1/m$ (C_{2h}^2, No. 11), possesses two Raman active modes: Ag and Bg.[136] Within the range from 45 cm^{-1} to 300 cm^{-1}: Raman peaks at 86.84 cm^{-1}, 113.36 cm^{-1}, 143.25 cm^{-1}, 155.30 cm^{-1}, 163.02 cm^{-1}, 180.86 cm^{-1}, 187.61 cm^{-1}, 217.01 cm^{-1}

and 242.57 cm^{-1} are detected and attributed to A_g mode, and B_g oscillation causes peaks at 53.58 cm^{-1} and 121.56 cm^{-1}.

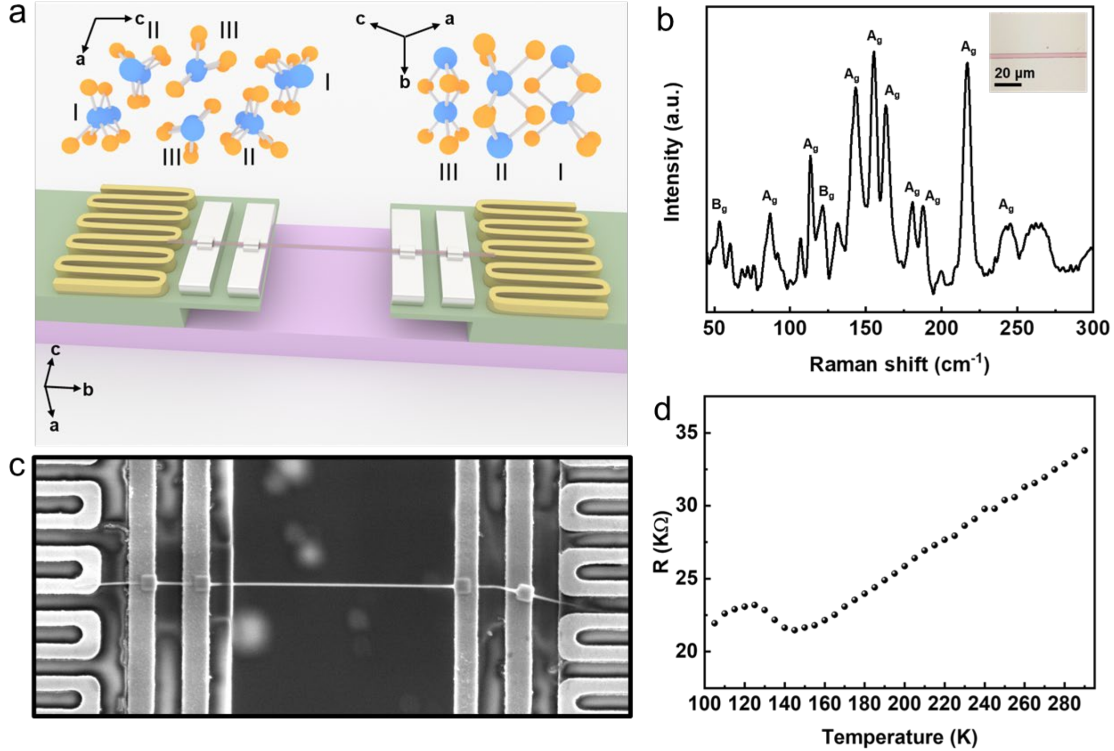

Figure 5.1 *Crystal structure, Raman spectrum, and resistance characteristics of $NbSe_3$. (a) A 3D schematic illustrating the layout of a suspended $NbSe_3$ device. Inset: crystal structure of $NbSe_3$: Left: stacking of the prisms along the b-axis; Right: projection of the crystal structure perpendicular to the b-axis. (b) Unpolarized Raman spectrum of layered $NbSe_3$. (c) SEM micrograph showing the top view of a final device. (d) Electrical resistance of a $NbSe_3$ nanowire in the temperature range of 120–295K.*

The 3D layout of the final device is shown in Figure 5.1a. A nanowire is placed between two suspended SiN_x membranes with integrated Pt heaters/resistance thermometers and extra electrodes. Figure 5.1c shows a top view SEM image of a typical device, identifying a nanowire with length ~ 8 µm. The electrical resistance R of a $NbSe_3$ nanowire is then measured with the standard 4-probe method to examine the CDW behaviors. During the electrical resistance measurement, to exclude the effects from CDW sliding, we set the electric field to be much smaller

than the measured depinning threshold electric field of the $NbSe_3$ nanowire with the same cross-sectional area. Note that in this report, we mainly focus on T_{CDW1}, therefore, a temperature range from 110 K to 295 K is presented. At temperatures above 145 K, R decreases as the temperature reduces, indicating a metallic behavior. However, at 145 K, the R increases abruptly reaches maxima at ~ 120-130K. The amplitudes of the peaks for on T_{CDW1} is 5% of the room-temperature resistance, in good agreement with those reported for $NbSe_3$ nanowire.[129, 137]

5.3 Anisotropic photocurrent along the nanowire

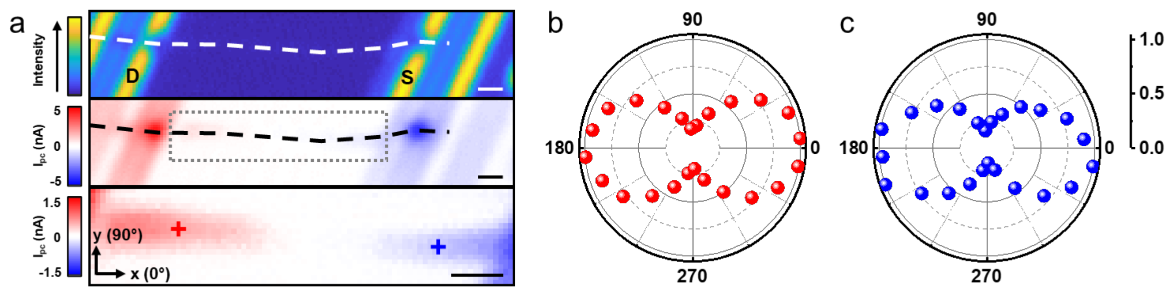

Figure 5.2 *Anisotropic photocurrent of the $NbSe_3$ nanowire. (a) Scanning reflection mapping (top panel) and scanning photocurrent mapping (middle panel) of a suspended $NbSe_3$ device (650 nm illumination, measured between D and S electrodes). Bottom panel: the zoom-in image of dotted boxed region in the middle panel. (b) and (c): Normalized photocurrent intensities on the $NbSe_3$ wire as a function of incident light polarization angle. Their positions are marked by red and blue '+' in the bottom panel of (a).*

Scanning photocurrent microscopy is utilized to investigate the optoelectronic behaviors of the suspended $NbSe_3$ nanowire. Figure 5.2a top and middle panels show reflection and photocurrent images of a suspended $NbSe_3$ nanowire with D_h = 29.0 nm, where the position of the nanowire is outlined by white or black dashed lines, respectively. Note here that the photocurrent signals are collected between inner electrodes. Strong photocurrent responses are observed at the nanowire-Pt interfaces, which may be attributed to the PTE considering the Seebeck coefficient difference between the nanowire channel and the Pt electrodes. Photocurrent signals can also be

detected along the nanowire and clearly displayed in the zoomed image. Further polarization-dependent photocurrent measurements reveal that the maximum photoresponse occurs when the incident laser is polarized parallel to the wire, as illustrated in Figure 5.2b and 5.2c. This anisotropic behavior is similar to previously reported anisotropic in-plane electrical and optical properties of TMTCs, which is caused by the reduced symmetry in the crystal structure.[24]

5.4 Laser induced CDW melting

To further understand the laser-nanowire interactions, especially whether the laser can affect the CDW properties of the $NbSe_3$ nanowire, temperature-dependent photoresponse is subsequently investigated. The laser is fixed to one position on the nanowire (almost the center and slightly to the source side of the wire), while the temperature varies from 115 K to 170 K. Note here electronic and optoelectronic properties of the device were characterized in a Janis ST-500 Microscopy Cryostat under high vacuum (∼10−6 Torr). Both photoconductivity and photovoltage are recorded as functions of temperature. As displayed in Figure 5.3a, under the illumination of 650 nm laser, T_{CDW1} shifts from 145 K to a lower temperature. The change of T_{CDW1}, Δ_{TCDW1} varies from 7.55 K under the illumination of laser with 2.5 μW power, increases to 12.31 K for 5 μW and finally, under 10 μW laser, the T_{CDW1} becomes difficult to be identified within the measurement range. The T_{CDW1} shift might be explained by the locally heat up under laser illumination.

Interestingly, the laser also causes the R at the T_{CDW1} to rise, and furthermore, we also found that the abrupt R increase from T_{CDW1} to 120-130K becomes smooth and even nearly flat when the laser power is lifted. This change leads to an attenuation of the CDW effect, which matches the CDW melting or CDW gap closure that is reported in many literatures. Especially,

one previous report shows that for weak light perturbation, the CDW is still partially present, while large light fluence can completely suppress the CDW.[138, 139]

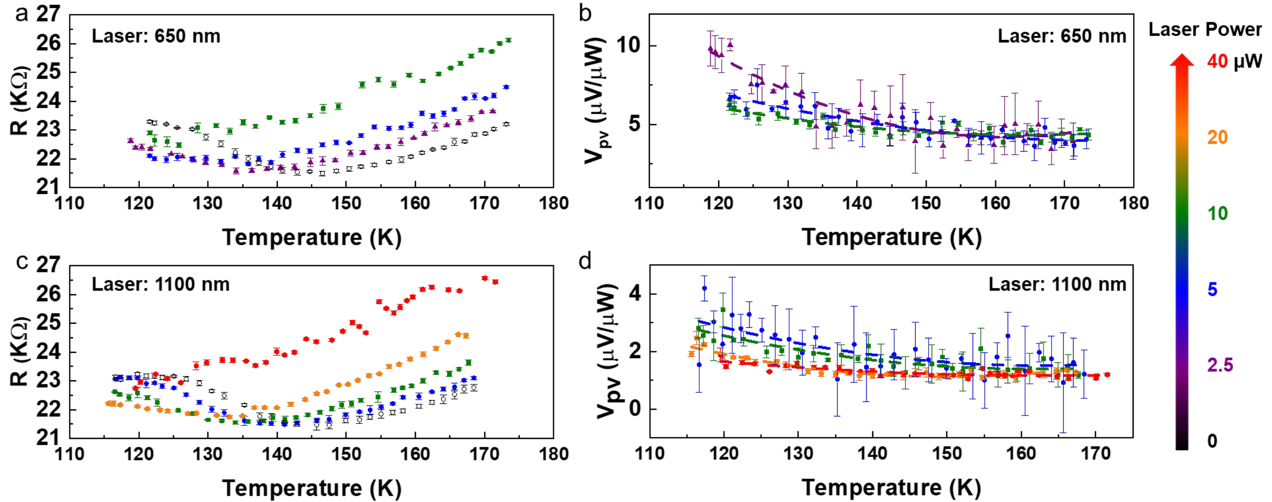

Figure 5.3 *Temperature-dependent photoconductivity and photovoltage of the $NbSe_3$ nanowire. (a) Photoconductivity and (b) photovoltage as functions of temperature with laser power from 2.5 µW to 10 µW under 650 nm laser illumination. (c) Photoconductivity and (d) photovoltage as functions of temperature with laser power from 5 µW to 40 µW under 1110 nm laser illumination.*

Furthermore, the incident laser also induces detectable photovoltage, even without external bias. As displayed in Figure 5.3b, the photovoltage is proportional to laser power and stays almost constant for temperature above T_{CDW1}. However, for temperature below T_{CDW1}, where the CDW phase transition happens, the photovoltage tends to rise and its dependence on laser power becomes complex.

To further understand this phenomenon, temperature-dependent conductivities measurements are conducted under various laser power but with wavelength 1100 nm. Similar results are observed but the nanowire exhibit a less sensitive response to laser at the longer wavelength. Much stronger illumination is needed for 1100 nm laser to achieve the same CDW melting effect.

Inspired by previous studies where the Rothwarf-Taylor (R-T) model is applied to analyze the photoexcitation dynamics in the CDW materials, we adapt the method to further investigate our results and their underlying mechanism.[138] As illustrated in figure 5.4a and 5.4b, the incident laser excites electrons and holes n_e in the material, followed by rapidly scattering of these particles with themselves, selectively coupled phonons (SCPs), and the thermal bath. This kinetic energy relaxation process ends up in quasiparticles (QPs) n_q, states near the Fermi energy as the following equation describes:

$$\frac{dn_e}{dt} = S(t) - \frac{n_e}{\tau_e} - \frac{n_e}{\tau_{ep}} - \frac{n_e}{\tau_{th}} \qquad 1$$

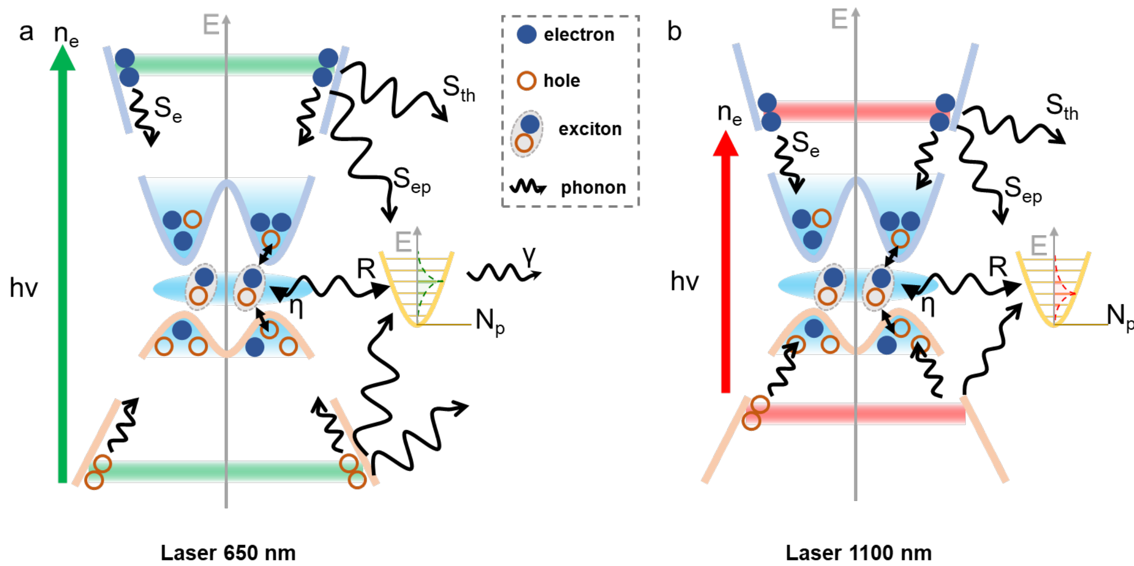

Figure 5.4 *Photoexcitation processes. sketch of processes for photoexcitation of (a) 650 nm and (b) 1100 nm laser. the main scattering processes: hot electrons and hot holes with other carriers,* τ_e^{-1}*, selectively coupled phonons,* τ_{ep}^{-1}*, and the thermal bath,* τ_{th}^{-1}*. R: the recombination rate of two QPs, generating an SCP.* η*: the breaking rate of an exciton with an SCP, generating two QPs.* γ*: the anharmonic phonon-phonon scattering with the thermal bath.*

where S(t) is the injection rate of hot free carriers by the laser. At the same time, scattering of two QPs with an SCP occurs with a recombination rate R. Also, an exciton breaks into generating two QPs with an SCP at a rate. Finally, the γ notes the rate of anharmonic phonon-phonon scattering with the thermal bath. Those processes can also be described:

$$\frac{dn_p}{dt} = \frac{n_e}{\tau_e} + \eta N_p - 2Rn_T n_q - R{n_q}^2 \quad 2$$

$$\frac{dN_p}{dt} = \frac{n_e}{\tau_{ep}} - \frac{\eta N_p}{2} + Rn_T n_q + \frac{R{n_q}^2}{2} - \gamma N_p \quad 3$$

where n_T denotes the density of thermally excited QPs. The QPs near the Fermi energy that probably contributes to the CDW gap closure and its amount n_q, is directly related to n_e.

For 1100 nm and 650 nm illumination with equal power, 1100 nm laser possesses a larger population of the photon ($n_{photon} = \frac{P\lambda}{hc}$, h is the Plank constant and c is the speed of light), which indicates larger n_e. However, on the other hand, the diffraction limit of the focused laser and the absorption spectrum need also to be considered and examined. The beam waist w of a focused laser can be estimated by $w = \frac{\lambda}{\pi NA}$, which is 345 nm and 584 nm for 650 nm and 1100 nm laser, leading to a lower power density for 1100 nm laser when compared to 650 nm laser with same laser power. Since the cross area for the nanowire is much smaller than the diameter 2w of the focused laser, the laser power that reaches the nanowire needs to be further determined by the nanowire dimension and the power density. Therefore, for the 650 nm and 1100 nm laser with same power, if the photon that reach the nanowire can be entirely absorbed to excites electrons and holes, the electron/hole amount n_e should be the same. However, the absorption spectrum of $NbSe_3$ indicates more absorption for 650 nm than 1100 nm, which results in n_e under 650 nm is larger

than the n_e under 1100 nm with the same power.[140] As a result, under the illumination of equal power, 650 nm laser can allow more energy that interacts with the nanowire, leading to more effective CDW melting.

Back to the photovoltage behaviors, we interestingly find that the Seebeck coefficient reported for the $NbSe_3$ nanowire also starts to increase when the temperature goes below T_{CDW1}. Since the laser spot is located slightly to the source side, the temperature rise on the nanowire can make the temperature of the source electrode slightly higher than the drain electrode. Since the Seebeck coefficient change from -15 μV/K at 120K to -10 μV/K around T_{CDW1},[129] 1K difference between the source and drain electrodes can cause a photo-thermoelectric effect (PTE) induced voltage change from -15 μV at 120K to -10 μV around T_{CDW1}, considering $\Delta V_{PTE} = (S_{NbSe_3} - S_{Pt})\Delta T$(S is the Seebeck coefficient). Moreover, with large laser flux, the CDW is further suppressed, which then lower the rate γ of the anharmonic phonon-phonon scattering with the thermal bath.[138] As a result, the temperature rise per μW may decrease as the laser power increases. This behavior probably can provide an explanation for figure 5.3b and 5.3d, where strong laser presents relatively lower photovoltages per μW, especially in the CDW range.

Chapter 6 Summary and outlook

6.1 Summary

Researchers never stop their effort to achieve electronics and optoelectronics with improved performances. Low-dimensional vdW materials allow dimensions down to the atomic scale but still maintain the crystal structure, exhibiting potential for future electronics scaling down. Their atomic dimension, on the other hand, combined with their great mechanical properties, making them promising candidates for flexible/foldable thin film devices, and enabling them to be integrated with other planer platforms. The confinement in dimension also makes the observation of many quantum effects become possible, and at the same time yield numerous novel properties that can benefit for electronics and optoelectronics. My Ph.D. research focuses on optoelectronics characteristics of novel low-dimension material and low-dimensional material with novel device structures. Although all my work may cover only an extremely small portion of the entire low-dimension material field, the fascinating properties I observed reflect some of their most exciting potential in future applications.

In Chapter 2, a high performance WSe_2 based photodetectors is first demonstrated by achieving ohmic contacts with 2D/2D contact structure. Outstanding electrical transport behaviors with a field-effect hole mobility of ~300 $cm^2 \cdot V^{-1} \cdot s^{-1}$ are achieved, leading to a high photoresponsivity of ~ 600 mA/W and high detectivity up to ~10^{13} with a high external quantum efficiency up to 100% and a response time (both rise and decay times) shorter than 8 μs. Chapter 3 presents a few-layer BP photodetector on top of a nanostructured silicon waveguide that can visualize the light-scattering patterns of the waveguide by scanning photocurrent mapping. Hot electron injection from the silicon waveguide to the BP channel is demonstrated to play an

important role in the detection. From Chapter 4, I further reduce the dimension of vdW materials and successfully demonstrate tunneling effect between TPtS and TPdS nanoribbons. Finally, in Chapter 5, CDW melting effect induced by the laser is observed in suspended $NbSe_3$ nanowires.

6.2 Challenges and Outlook

Many challenges still existed for low-dimensional vdW material, especially for practical applications, which go to large scales and under ambient environments. However, I do believe low-dimensional vdW material reserve advantages over traditional 3D materials, especially for easy integration with other platforms and detections down to atomic scales. Below I propose some potentially interesting directions.

2D photonic crystal integrated 2D material based photodetectors

Photonic crystals are analogous to crystals where the unit structure is periodically duplicated.[102, 141] When the periodicity in these structures approaches the wavelength of light, a photonic bandgap (PBG), in which the light propagation is forbidden, will appear. The arrangement, materials, structural symmetry and lattice parameters determine the bandwidth and the frequency of the PBG. The geometry of 2D photonic crystals makes it easy to planarized themselves to be integrated with 2D material based photodetectors. Like other photonic structures discussed in Chapter 3, the integration of a 2D photonic crystal with a 2D material based photodetector may provide an approach to manipulate the light absorption in 2D materials in a controllable way. Furthermore, a pre-designed break in periodicity will introduce a localized mode and thus led to confinement of light, which makes it possible to achieve light-matter manipulations in a certain location as designed.[141] Photonic crystals with pre-designed break have been reported in several previous literatures, in which photonic crystals are integrated with 2D materials

optoelectronics to achieve enhanced light-matter interactions and improved modulation performances.[107, 108, 142, 143]

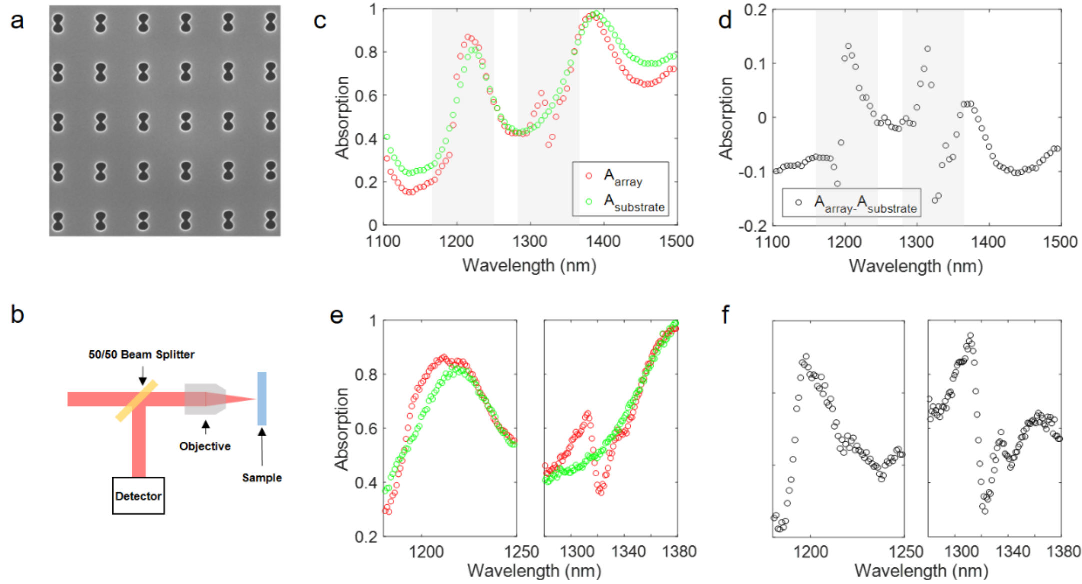

Figure 6.1 *Absorption spectrum of a 2D photonic crystal with bowtie unit cell. (a) SEM image of the 2D photonic crystal based on a bowtie unit cell. (b) A schematic diagram of the experimental setup for light absorption spectra measurement. (c)Experimentally measured absorption of the total absorption (red circles) and silicon substrate absorption (green circles), respectively, and subtraction of silicon substrate absorption from the total absorption (black circles) (d). Finer measurements are conducted with results shown in (e)and (f), which present zoom-in details for the shadowed area in (c) and (d).*

Our preliminary experimental results, as displayed in Figure 6.1, the 2D photonic crystal is designed is based on a bowtie unit cell. [144] Absorption measurements present two asymmetric line-shape resonances (shadowed areas) within the wavelength range from 1100 to 1500 nm. Those resonances show similarity to the Fano resonance, which is related to the interference between Mie scattering (as a continuum state from each unit cell) and Bragg scattering (as a discrete state from the 2D array) and shows an asymmetric profile of a narrow band in the spectrum.[145-147]

Detail mechanisms can be investigated with the assistance of the FTDT simulations. Then, a 2D TMDCs or BP based photodetector (depending on where the resonances locate) on the top of the 2D photonic crystal. The absorption spectra measurement will be conducted right after the fabrication to identify the resonance properties. Optoelectronic characteristics will be subsequently conducted for this photonic crystal-2D material system. Furthermore, a pre-designed break in the 2D photonic crystal can also be introduced and the scanning photocurrent measurements can give a straightforward way to investigate the light-matter interactions locally.

SWNT based detection platform for DNA

The π-electron interfaces are ubiquitous and the interactions between π-electron interfaces happen all the time in our nature.[148-152] These non-covalent bindings play fundamental and essential roles in various disciplines, but a full understanding of these interactions is still unavailable. The main reason here may be the small dimension of many biomolecules (for example, 2 nm in diameter for a DNA molecule), which requires experimental detection down to single molecule level. SWNT possesses a typical diameter of 1-2 nm, which is comparable to the diameter of a DNA. SWNT has also been demonstrated to show outstanding electrical and optoelectrical behaviors and enormous tensile strength. All those properties make it a great candidate for detecting the interactions of π-electron interfaces between a DNA molecule and a CNT via multiform ways.

Another challenge for detecting interactions between π-electron interfaces rises for the difficulty to control biomolecule with high precision. Optical tweezers offer a solution in this respect. Optical tweezers are devices that use a highly focused laser beam to provide a force to manipulate objects ranging in size from 10 nm to over 100 mm. The physical principles behind optical trapping are relatively simple and straightforward: the field gradients near the focus of a

laser beam which give rise to a trapping force towards the point of highest intensity formed. In the vicinity of this focus, the optical trap shows a linear "Hookean" spring behavior. As a result, the forces applied on an object proportional to its displacement from the center of the trap.[153, 154]

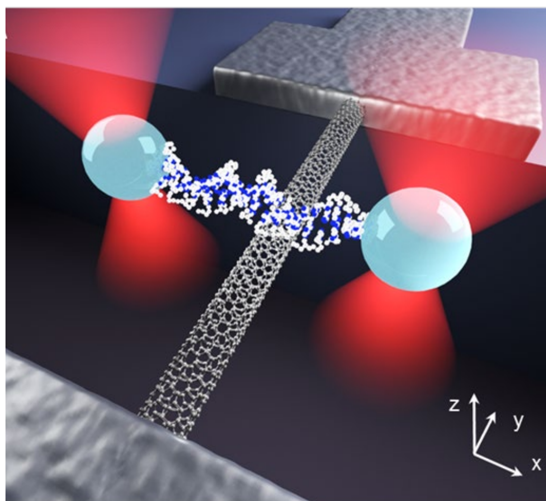

Figure 6.2 *Schematic of a SWNT transistor combined with dual-trap optical tweezers.*

Here, we report a detection platform that combines a suspended SWNT transistor with dual-trap optical tweezers to explore interactions of π-electron interfaces between SWNT and DNA. The entire detection platform is illustrated as shown in Figure 6.2. Force detection with sub-piconewton level can be achieved via position sensitive detector (PSD) and video image analysis (VIA). At the same time, current signals and the photocurrents signals that go through the SWNT transistor can be detected during the interactions to provide additional information to decode the interactions of π-electron interfaces.

A SWNT was grown via CVD to bridge the source/drain Pt contacts to form a SWNT transistor. Note that the CNT device is sealed in a home-made microfluidic and can be modulated via electrolyte gate.[155, 156] Furthermore, one more laser is combined to the platform for 3D scanning photocurrent microscopy (additional movement along z direction to the scanning

photocurrent microscopy described in Chapter 1). The photocurrent signals can be recorded at different 3D positions, making it possible to reconstruct the 3D morphology of the CNT, helping us to visualize the interaction between the CNT and DNA.

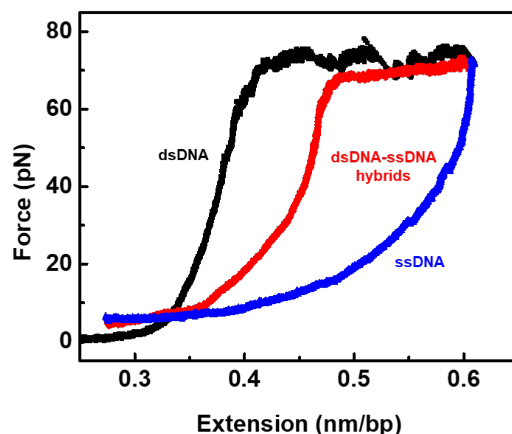

Figure 6.3 *Overstretching dsDNA to dsDNA-ssDNA hybrid to ssDNA.Force-extension curves of a dsDNA, an ssDNA-dsDNA hybrid and ssDNA.*

By separating the optical traps along x direction, the dsDNA can be overstretched to form a dsDNA/single-stranded DNA (ssDNA) hybrid structure as shown in Figure 6.3.[148] As a result, we can study the force or current signal difference when the CNT interacts with dsDNA or ssDNA. Furthermore, in previous literatures, the binding energies for the four base types with graphite/CNTs are predicted to be different: guanine (G) > adenine (A) > thymine (T) > cytosine (C).[157-159] With the assistance of the detection platform, we are expected to directly detect the bind force difference and also how the current signal changes when the CNT interacts with different base types. Here, we note that, optical tweezers can offer higher force resolution but much slower data collection rates with an extremely low loading rate in comparison with AFM probes, enabling the binding rupture occurs in a near-equilibrium regime. therefore, it will become possible to decode DNA sequence by reading either the force or current signals. Furthermore, we can

replace the CNT with 2D graphene to allow longer DNA sequence for one interaction. On the other hand, we can also monitor the binding force and current signal change when the electrochemical environment is controlled by various external voltages, and thus learn how the electrochemical environment changes the interaction between the π-electron interfaces.

APPENDIX Instructions for Transfer

SiO_2/Si chip preparation

1. Spin coat photoresist (Shipley 1800 series) and soft bake at 90 ºC to protect SiO_2/Si wafer.
2. Dicing into small chips.
3. Soak in Acetone (5 min) and IPA (5 min) to remove photoresist, dry with nitrogen.
4. Soak in nanostrip at 60 ºC for at least 1 hour, rinse with running DI water for at least 30s, dry with nitrogen.
5. Check chip with AFM. Scan 20μm square, should show no particle, roughness ±500pm.

Metal electrode fabrication and release

1. Fabricate 50-nm-thick metal electrodes array with on a Si wafer using standard photolithography, high-vacuum electron-beam evaporation, followed by lift off process.
2. Spin coat photoresist (Shipley 1800 series) and soft bake at 90 ºC to protect the wafer
3. Dicing into small chips.
4. Soak in Acetone (5 min) and IPA (5 min) to remove photoresist, dry with nitrogen.
5. Place the chip (with metal electrodes) in a sealed HMDS chamber at 120 °C for 2-30 mins and then spin coat it with 2-10 μm thick PMMA polymer, bake at 180 °C for 2 mins
6. Mount PDMS stamp on glass slide, face down and full contact with the chip (with metal electrodes and covered by PMMA layer).
7. Quick release and metal/PMMA will stay on the PDMS stamp.

Pick up and transfer

1. Pick up: face the metal/PMMA side of PDMS stamp to the target sample on substrate, align the sample with electrodes, fully contact, rise temperature to around 25-30 ºC, slowly lift the PDMS stamp to pick up the sample.
2. Transfer: face the metal/PMMA side of PDMS stamp to the target sample on substrate, align the sample with electrodes, fully contact, rise temperature to around 60-70 ºC, slowly lift the PDMS stamp to leave the PMMA film stay on the substrate.

Window opening

1. Standard EBL on the PMMA layer (dose may vary depending on the thickness of PMMA layer), followed by rinse with developer.

References

1. Geim, A.K. and K.S. Novoselov, *The rise of graphene.* Nat Mater, 2007. **6**(3): p. 183-191.
2. Cai, M., et al., *Methods of graphite exfoliation.* Journal of Materials Chemistry, 2012. **22**(48): p. 24992-25002.
3. Castellanos-Gomez, A.J.N.P., *Why all the fuss about 2D semiconductors?* 2016. **10**(4): p. 202.
4. Kane, C.L. and E.J. Mele, *Quantum Spin Hall Effect in Graphene.* Physical Review Letters, 2005. **95**(22): p. 226801.
5. Lee, C., et al., *Measurement of the Elastic Properties and Intrinsic Strength of Monolayer Graphene.* 2008. **321**(5887): p. 385-388.
6. Balandin, A.A., et al., *Superior Thermal Conductivity of Single-Layer Graphene.* Nano Letters, 2008. **8**(3): p. 902-907.
7. Nair, R.R., et al., *Fine Structure Constant Defines Visual Transparency of Graphene.* Science, 2008. **320**(5881): p. 1308-1308.
8. Schwierz, F., *Graphene transistors.* Nature Nanotechnology, 2010. **5**(7): p. 487-496.
9. Balog, R., et al., *Bandgap opening in graphene induced by patterned hydrogen adsorption.* Nature Materials, 2010. **9**(4): p. 315-319.
10. Zhou, S.Y., et al., *Substrate-induced bandgap opening in epitaxial graphene.* Nature Materials, 2007. **6**(10): p. 770-775.
11. Xu, X., et al., *Interfacial engineering in graphene bandgap.* Chemical Society Reviews, 2018. **47**(9): p. 3059-3099.
12. Wang, Q.H., et al., *Electronics and optoelectronics of two-dimensional transition metal dichalcogenides.* Nat Nano, 2012. **7**(11): p. 699-712.
13. Mak, K.F. and J. Shan, *Photonics and optoelectronics of 2D semiconductor transition metal dichalcogenides.* Nat Photon, 2016. **10**(4): p. 216-226.
14. Stefano, L., F. Babak, and T. Emanuel, *Field-effect transistors and intrinsic mobility in ultra-thin $MoSe_2$ layers.* Applied Physics Letters, 2012. **101**(22): p. 223104.
15. Ross, J.S., et al., *Electrically tunable excitonic light-emitting diodes based on monolayer WSe_2 p-n junctions.* Nat Nano, 2014. **9**(4): p. 268-272.
16. RadisavljevicB, et al., *Single-layer MoS_2 transistors.* Nat Nano, 2011. **6**(3): p. 147-150.
17. Yin, Z., et al., *Single-Layer MoS_2 Phototransistors.* ACS Nano, 2012. **6**(1): p. 74-80.
18. Zeng, H., et al., *Valley polarization in MoS_2 monolayers by optical pumping.* Nat Nano, 2012. **7**(8): p. 490-493.
19. Jones, A.M., et al., *Optical generation of excitonic valley coherence in monolayer WSe_2.* Nat Nano, 2013. **8**(9): p. 634-638.
20. Xia, F., H. Wang, and Y. Jia, *Rediscovering black phosphorus as an anisotropic layered material for optoelectronics and electronics.* 2014. **5**: p. 4458.
21. Li, L., et al., *Black phosphorus field-effect transistors.* Nat Nano, 2014. **9**(5): p. 372-377.
22. Tran, V., et al., *Layer-controlled band gap and anisotropic excitons in few-layer black phosphorus.* Physical Review B, 2014. **89**(23): p. 235319.
23. Ajayan, P., P. Kim, and K. Banerjee, *Two-dimensional van der Waals materials.* Physics Today, 2016. **69**(9): p. 39-44.

24. Island, J.O., et al., *Electronics and optoelectronics of quasi-1D layered transition metal trichalcogenides.* 2D Materials, 2017. **4**(2): p. 022003.
25. Heremans, J.P., R.J. Cava, and N. Samarth, *Tetradymites as thermoelectrics and topological insulators.* Nature Reviews Materials, 2017. **2**: p. 17049.
26. Xiong, Y., et al., *From 2D Framework to Quasi-1D Nanomaterial: Preparation, Characterization, and Formation Mechanism of Cu_3SnS_4 Nanorods.* Inorganic Chemistry, 2002. **41**(11): p. 2953-2959.
27. Liu, H.-J. and Y.-C. Zhu, *Synthesis and characterization of ternary chalcogenide ZnCdS 1D nanostructures.* Materials Letters, 2008. **62**(2): p. 255-257.
28. Sato, T., et al., *Direct Evidence for the Dirac-Cone Topological Surface States in the Ternary Chalcogenide $TlBiSe_2$.* Physical Review Letters, 2010. **105**(13): p. 136802.
29. Dai, J. and X.C. Zeng, *Titanium trisulfide monolayer: theoretical prediction of a new direct-gap semiconductor with high and anisotropic carrier mobility.* Angew Chem Int Ed Engl, 2015. **54**(26): p. 7572-6.
30. Jin, Y., X. Li, and J. Yang, *Single layer of MX_3 (M = Ti, Zr; X = S, Se, Te): a new platform for nano-electronics and optics.* Physical Chemistry Chemical Physics, 2015. **17**(28): p. 18665-18669.
31. Island, J.O., et al., *Titanium trisulfide (TiS_3): a 2D semiconductor with quasi-1D optical and electronic properties.* Scientific Reports, 2016. **6**: p. 22214.
32. Lipatov, A., et al., *Few-layered titanium trisulfide (TiS_3) field-effect transistors.* Nanoscale, 2015. **7**(29): p. 12291-12296.
33. Geremew, A., et al., *Current Carrying Capacity of Quasi-1D $ZrTe_3$ van Der Waals Nanoribbons.* IEEE Electron Device Letters, 2018. **39**(5): p. 735-738.
34. Liu, G., et al., *Low-Frequency Electronic Noise in Quasi-1D $TaSe_3$ van der Waals Nanowires.* Nano Letters, 2017. **17**(1): p. 377-383.
35. Stolyarov, M.A., et al., *Breakdown current density in h-BN-capped quasi-1D $TaSe_3$ metallic nanowires: prospects of interconnect applications.* Nanoscale, 2016. **8**(34): p. 15774-15782.
36. Eda, G. and S.A. Maier, *Two-Dimensional Crystals: Managing Light for Optoelectronics.* ACS Nano, 2013. **7**(7): p. 5660-5665.
37. Freitag, M., et al., *Photoconductivity of biased graphene.* Nat Photon, 2013. **7**(1): p. 53-59.
38. Gan, X., et al., *Chip-integrated ultrafast graphene photodetector with high responsivity.* Nat Photon, 2013. **7**(11): p. 883-887.
39. Xia, F., et al., *Two-dimensional material nanophotonics.* Nature Photonics, 2014. **8**(12): p. 899-907.
40. Geim, A.K. and I.V. Grigorieva, *Van der Waals heterostructures.* Nature, 2013. **499**(7459): p. 419-425.
41. Withers, F., et al., *Light-emitting diodes by band-structure engineering in van der Waals heterostructures.* Nature Materials, 2015. **14**: p. 301.
42. Liu, Y., et al., *Van der Waals heterostructures and devices.* Nature Reviews Materials, 2016. **1**: p. 16042.
43. Fang, H., et al., *Strong interlayer coupling in van der Waals heterostructures built from single-layer chalcogenides.* 2014. **111**(17): p. 6198-6202.
44. Deng, Y., et al., *Black Phosphorus–Monolayer MoS_2 van der Waals Heterojunction p–n Diode.* ACS Nano, 2014. **8**(8): p. 8292-8299.

45. Hong, T., et al., *Anisotropic photocurrent response at black phosphorus-MoS_2 p-n heterojunctions.* Nanoscale, 2015. **7**(44): p. 18537-18541.
46. Dean, C.R., et al., *Boron nitride substrates for high-quality graphene electronics.* Nat Nano, 2010. **5**(10): p. 722-726.
47. Wang, L., et al., *One-Dimensional Electrical Contact to a Two-Dimensional Material.* Science, 2013. **342**(6158): p. 614-617.
48. Youngblood, N., et al., *Waveguide-integrated black phosphorus photodetector with high responsivity and low dark current.* Nat Photon, 2015. **9**(4): p. 247-252.
49. Zhang, B.Y., et al., *Broadband high photoresponse from pure monolayer graphene photodetector.* 2013. **4**: p. 1811.
50. Xia, F., et al., *Ultrafast graphene photodetector.* Nat Nano, 2009. **4**(12): p. 839-843.
51. Lopez-Sanchez, O., et al., *Ultrasensitive photodetectors based on monolayer MoS_2.* Nat Nano, 2013. **8**(7): p. 497-501.
52. Zhaoqiang, Z., et al., *Flexible, transparent and ultra-broadband photodetector based on large-area WSe_2 film for wearable devices.* Nanotechnology, 2016. **27**(22): p. 225501.
53. Park, J., Y.H. Ahn, and C. Ruiz-Vargas, *Imaging of Photocurrent Generation and Collection in Single-Layer Graphene.* Nano Letters, 2009. **9**(5): p. 1742-1746.
54. Xia, F., et al., *Photocurrent Imaging and Efficient Photon Detection in a Graphene Transistor.* Nano Letters, 2009. **9**(3): p. 1039-1044.
55. Wang, T. and Y.-Q. Xu, *Photonic Structure-Integrated Two-Dimensional Material Optoelectronics.* 2016. **5**(4): p. 93.
56. Nolas, G.S., J. Sharp, and J. Goldsmid, *Thermoelectrics: basic principles and new materials developments*. Vol. 45. 2013: Springer Science & Business Media.
57. Cutler, M. and N.F. Mott, *Observation of Anderson Localization in an Electron Gas.* Physical Review, 1969. **181**(3): p. 1336-1340.
58. Xu, X., et al., *Photo-Thermoelectric Effect at a Graphene Interface Junction.* Nano Letters, 2010. **10**(2): p. 562-566.
59. Grosse, K.L., et al., *Nanoscale Joule heating, Peltier cooling and current crowding at graphene-metal contacts.* Nat Nano, 2011. **6**(5): p. 287-290.
60. Wu, J., et al., *Large Thermoelectricity via Variable Range Hopping in Chemical Vapor Deposition Grown Single-Layer MoS_2.* Nano Letters, 2014. **14**(5): p. 2730-2734.
61. Low, T., et al., *Origin of photoresponse in black phosphorus phototransistors.* Physical Review B, 2014. **90**(8): p. 081408.
62. Flores, E., et al., *Thermoelectric power of bulk black-phosphorus.* Applied Physics Letters, 2015. **106**(2): p. 022102.
63. Engel, M., M. Steiner, and P. Avouris, *Black Phosphorus Photodetector for Multispectral, High-Resolution Imaging.* Nano Letters, 2014. **14**(11): p. 6414-6417.
64. Tsen, A.W., et al., *Imaging the electrical conductance of individual carbon nanotubes with photothermal current microscopy.* Nat Nano, 2009. **4**(2): p. 108-113.
65. Hong, T., et al., *Plasmonic Hot Electron Induced Photocurrent Response at MoS_2–Metal Junctions.* ACS Nano, 2015. **9**(5): p. 5357-5363.
66. Gong, X., et al., *High-Detectivity Polymer Photodetectors with Spectral Response from 300 nm to 1450 nm.* Science, 2009. **325**(5948): p. 1665-1667.
67. Buscema, M., et al., *Photocurrent generation with two-dimensional van der Waals semiconductors.* Chemical Society Reviews, 2015. **44**(11): p. 3691-3718.

68. Konstantatos, G., *Current status and technological prospect of photodetectors based on two-dimensional materials.* Nature Communications, 2018. **9**(1): p. 5266.
69. Muller, R.S., et al., *Device electronics for integrated circuits.* 1986: p. 140-164.
70. Choi, W., et al., *High-Detectivity Multilayer MoS2 Phototransistors with Spectral Response from Ultraviolet to Infrared.* Advanced Materials, 2012. **24**(43): p. 5832-5836.
71. Yi, Y., et al., *A study of lateral Schottky contacts in WSe_2 and MoS_2 field effect transistors using scanning photocurrent microscopy.* Nanoscale, 2015. **7**(38): p. 15711-15718.
72. Li, H.-M., et al., *Metal-Semiconductor Barrier Modulation for High Photoresponse in Transition Metal Dichalcogenide Field Effect Transistors.* Scientific Reports, 2014. **4**: p. 4041.
73. Allain, A., et al., *Electrical contacts to two-dimensional semiconductors.* Nat Mater, 2015. **14**(12): p. 1195-1205.
74. Zhang, W., et al., *Role of Metal Contacts in High-Performance Phototransistors Based on WSe_2 Monolayers.* ACS Nano, 2014. **8**(8): p. 8653-8661.
75. Pradhan, N.R., et al., *High Photoresponsivity and Short Photoresponse Times in Few-Layered WSe_2 Transistors.* Acs Applied Materials & Interfaces, 2015. **7**(22): p. 12080-12088.
76. Chuang, H.-J., et al., *Low-Resistance 2D/2D Ohmic Contacts: A Universal Approach to High-Performance WSe_2, MoS_2, and $MoSe_2$ Transistors.* Nano Letters, 2016. **16**(3): p. 1896-1902.
77. Wang, T., et al., *High-Performance WSe_2 Phototransistors with 2D/2D Ohmic Contacts.* Nano Letters, 2018. **18**(5): p. 2766-2771.
78. Ding, Y., et al., *First principles study of structural, vibrational and electronic properties of graphene-like MX_2 (M=Mo, Nb, W, Ta; X=S, Se, Te) monolayers.* Physica B: Condensed Matter, 2011. **406**(11): p. 2254-2260.
79. Kam, K.K. and B.A. Parkinson, *Detailed photocurrent spectroscopy of the semiconducting group VIB transition metal dichalcogenides.* The Journal of Physical Chemistry, 1982. **86**(4): p. 463-467.
80. He, K., et al., *Tightly Bound Excitons in Monolayer WSe_2.* Physical Review Letters, 2014. **113**(2): p. 026803.
81. Wang, G., et al., *Giant Enhancement of the Optical Second-Harmonic Emission of WSe_2 Monolayers by Laser Excitation at Exciton Resonances.* Physical Review Letters, 2015. **114**(9): p. 097403.
82. Wang, H.N., C.J. Zhang, and F. Rana, *Surface Recombination Limited Lifetimes of Photoexcited Carriers in Few-Layer Transition Metal Dichalcogenide MoS_2.* Nano Letters, 2015. **15**(12): p. 8204-8210.
83. Palummo, M., M. Bernardi, and J.C. Grossman, *Exciton Radiative Lifetimes in Two-Dimensional Transition Metal Dichalcogenides.* Nano Letters, 2015. **15**(5): p. 2794-2800.
84. Hsu, W.-T., et al., *Optically initialized robust valley-polarized holes in monolayer WSe_2.* Nature Communications, 2015. **6**(1): p. 8963.
85. Ahn, Y., J. Dunning, and J. Park, *Scanning Photocurrent Imaging and Electronic Band Studies in Silicon Nanowire Field Effect Transistors.* Nano Letters, 2005. **5**(7): p. 1367-1370.
86. Hong, T., et al., *Polarized photocurrent response in black phosphorus field-effect transistors.* Nanoscale, 2014. **6**(15): p. 8978-8983.

87. Zhang, W.J., et al., *High-Gain Phototransistors Based on a CVD MoS_2 Monolayer.* Advanced Materials, 2013. **25**(25): p. 3456-3461.
88. Baugher, B.W.H., et al., *Optoelectronic devices based on electrically tunable p-n diodes in a monolayer dichalcogenide.* Nat Nano, 2014. **9**(4): p. 262-267.
89. Wojtas, J., J. Mikolajczyk, and Z. Bielecki, *Aspects of the Application of Cavity Enhanced Spectroscopy to Nitrogen Oxides Detection.* Sensors, 2013. **13**(6): p. 7570.
90. Chang, Y.-H., et al., *Monolayer $MoSe_2$ Grown by Chemical Vapor Deposition for Fast Photodetection.* ACS Nano, 2014. **8**(8): p. 8582-8590.
91. Perea-López, N., et al., *Photosensor Device Based on Few-Layered WS_2 Films.* Advanced Functional Materials, 2013. **23**(44): p. 5511-5517.
92. Groenendijk, D.J., et al., *Photovoltaic and Photothermoelectric Effect in a Double-Gated WSe_2 Device.* Nano Letters, 2014. **14**(10): p. 5846-5852.
93. Bass, M., *Handbook of Optics: Devices, Measurements, and Properties*. 1994: McGraw-Hill Professoinal. 1568.
94. Liu, H., et al., *Phosphorene: An Unexplored 2D Semiconductor with a High Hole Mobility.* ACS Nano, 2014. **8**(4): p. 4033-4041.
95. Yuan, H., et al., *Polarization-sensitive broadband photodetector using a black phosphorus vertical p–n junction.* Nat Nano, 2015. **10**(8): p. 707-713.
96. Buscema, M., et al., *Fast and Broadband Photoresponse of Few-Layer Black Phosphorus Field-Effect Transistors.* Nano Letters, 2014. **14**(6): p. 3347-3352.
97. Qiao, J., et al., *High-mobility transport anisotropy and linear dichroism in few-layer black phosphorus.* 2014. **5**: p. 4475.
98. Takao, Y. and A. Morita, *Electronic structure of black phosphorus: Tight binding approach.* Physica B+C, 1981. **105**(1): p. 93-98.
99. Akahama, Y., S. Endo, and S.-i. Narita, *Electrical Properties of Black Phosphorus Single Crystals.* Journal of the Physical Society of Japan, 1983. **52**(6): p. 2148-2155.
100. Liu, H., et al., *Semiconducting black phosphorus: synthesis, transport properties and electronic applications.* Chemical Society Reviews, 2015. **44**(9): p. 2732-2743.
101. Cai, Y., G. Zhang, and Y.-W. Zhang, *Layer-dependent Band Alignment and Work Function of Few-Layer Phosphorene.* 2014. **4**: p. 6677.
102. Koenderink, A.F., A. Alù, and A. Polman, *Nanophotonics: Shrinking light-based technology.* Science, 2015. **348**(6234): p. 516-521.
103. Bao, Q. and K.P. Loh, *Graphene Photonics, Plasmonics, and Broadband Optoelectronic Devices.* ACS Nano, 2012. **6**(5): p. 3677-3694.
104. Grigorenko, A.N., M. Polini, and K.S. Novoselov, *Graphene plasmonics.* Nat Photon, 2012. **6**(11): p. 749-758.
105. Ding, Y., et al., *Effective Electro-Optical Modulation with High Extinction Ratio by a Graphene–Silicon Microring Resonator.* Nano Letters, 2015. **15**(7): p. 4393-4400.
106. Liu, M., et al., *A graphene-based broadband optical modulator.* Nature, 2011. **474**(7349): p. 64-67.
107. Gan, X., et al., *High-Contrast Electrooptic Modulation of a Photonic Crystal Nanocavity by Electrical Gating of Graphene.* Nano Letters, 2013. **13**(2): p. 691-696.
108. Majumdar, A., et al., *Electrical Control of Silicon Photonic Crystal Cavity by Graphene.* Nano Letters, 2013. **13**(2): p. 515-518.
109. Wang, W., et al., *Hot Electron-Based Near-Infrared Photodetection Using Bilayer MoS_2.* Nano Letters, 2015. **15**(11): p. 7440-7444.

110. Liu, Y., et al., *Plasmon resonance enhanced multicolour photodetection by graphene.* 2011. **2**: p. 579.
111. Echtermeyer, T.J., et al., *Strong plasmonic enhancement of photovoltage in graphene.* 2011. **2**: p. 458.
112. Pospischil, A., et al., *CMOS-compatible graphene photodetector covering all optical communication bands.* Nat Photon, 2013. **7**(11): p. 892-896.
113. Wang, X., et al., *High-responsivity graphene/silicon-heterostructure waveguide photodetectors.* Nat Photon, 2013. **7**(11): p. 888-891.
114. Liu, W., et al., *Strong Exciton–Plasmon Coupling in MoS_2 Coupled with Plasmonic Lattice.* Nano Letters, 2016. **16**(2): p. 1262-1269.
115. Lee, B., et al., *Fano Resonance and Spectrally Modified Photoluminescence Enhancement in Monolayer MoS_2 Integrated with Plasmonic Nanoantenna Array.* Nano Letters, 2015. **15**(5): p. 3646-3653.
116. Sobhani, A., et al., *Enhancing the photocurrent and photoluminescence of single crystal monolayer MoS_2 with resonant plasmonic nanoshells.* Applied Physics Letters, 2014. **104**(3): p. 031112.
117. Butun, S., S. Tongay, and K. Aydin, *Enhanced Light Emission from Large-Area Monolayer MoS_2 Using Plasmonic Nanodisc Arrays.* Nano Letters, 2015. **15**(4): p. 2700-2704.
118. Kim, S., et al., *Electronically tunable extraordinary optical transmission in graphene plasmonic ribbons coupled to subwavelength metallic slit arrays.* Nature Communications, 2016. **7**: p. 12323.
119. Wang, T., et al., *Visualizing Light Scattering in Silicon Waveguides with Black Phosphorus Photodetectors.* 2016. **28**(33): p. 7162-7166.
120. Brongersma, M.L., N.J. Halas, and P. Nordlander, *Plasmon-induced hot carrier science and technology.* Nat Nano, 2015. **10**(1): p. 25-34.
121. Lev, I.B., *Semiconductor Materials*. 1996: CRC Press. 496.
122. Keszler, D.A., et al., *New ternary and quaternary transition-metal selenides: Syntheses and characterization.* Journal of Solid State Chemistry, 1985. **57**(1): p. 68-81.
123. Keszler, D.A. and J.A. Ibers, *A new structural type in ternary chalcogenide chemistry: Structure and properties of $Nb_2Pd_3Se_8$.* Journal of Solid State Chemistry, 1984. **52**(1): p. 73-79.
124. Liu, X., et al., *Direct Fabrication of Functional Ultrathin Single-Crystal Nanowires from Quasi-One-Dimensional van der Waals Crystals.* Nano Letters, 2016. **16**(10): p. 6188-6195.
125. Liu, Y., et al., *Approaching the Schottky–Mott limit in van der Waals metal–semiconductor junctions.* Nature, 2018. **557**(7707): p. 696-700.
126. Singh, A. and U. Philipose, *Understanding the Mechanisms that Affect the Quality of Electrochemically Grown Semiconducting Nanowires*. 2018.
127. Fuhrer, M.S., et al., *Crossed Nanotube Junctions.* 2000. **288**(5465): p. 494-497.
128. Hor, Y.S., et al., *Nanowires and Nanoribbons of Charge-Density-Wave Conductor NbSe3.* Nano Letters, 2005. **5**(2): p. 397-401.
129. Yang, L., et al., *Distinct Signatures of Electron–Phonon Coupling Observed in the Lattice Thermal Conductivity of NbSe3 Nanowires.* Nano Letters, 2019. **19**(1): p. 415-421.
130. Stabile, A.A., et al., *Synthesis, characterization, and finite size effects on electrical transport of nanoribbons of the charge density wave conductor NbSe3.* Nanotechnology, 2011. **22**(48): p. 485201.

131. Chaussy, J., et al., *Phase transitions in NbSe3.* Solid State Communications, 1976. **20**(8): p. 759-763.
132. Bhadeshia, H.K.D.H. and C.M. Wayman, *9 - Phase Transformations: Nondiffusive*, in *Physical Metallurgy (Fifth Edition)*, D.E. Laughlin and K. Hono, Editors. 2014, Elsevier: Oxford. p. 1021-1072.
133. Fleming, R.M., D.E. Moncton, and D.B. McWhan, *X-ray scattering and electric field studies of the sliding mode conductor* $NbSe_3$*.* Physical Review B, 1978. **18**(10): p. 5560-5563.
134. Moudden, A.H., et al., q^1 *charge-density wave in* $NbSe_3$*.* Physical Review Letters, 1990. **65**(2): p. 223-226.
135. van Smaalen, S., et al., *Determination of the structural distortions corresponding to the* q^1*- and* q^2*-type modulations in niobium triselenide* $NbSe_3$*.* Physical Review B, 1992. **45**(6): p. 3103-3106.
136. Chen, H., et al., *Angle-/temperature-dependence of Raman scattering in layered NbSe3 crystal.* 2017. **7**(9): p. 095316.
137. McCarten, J., et al., *Charge-density-wave pinning and finite-size effects in* $NbSe_3$*.* Physical Review B, 1992. **46**(8): p. 4456-4482.
138. Hedayat, H., et al., *Excitonic and lattice contributions to the charge density wave in 1T-*$TiSe_2$ *revealed by a phonon bottleneck.* Physical Review Research, 2019. **1**(2): p. 023029.
139. Chávez-Cervantes, M., et al., *Charge Density Wave Melting in One-Dimensional Wires with Femtosecond Subgap Excitation.* Physical Review Letters, 2019. **123**(3): p. 036405.
140. Perucchi, A., L. Degiorgi, and R.E. Thorne, *Optical investigation of the charge-density-wave phase transitions in* $NbSe_3$*.* Physical Review B, 2004. **69**(19): p. 195114.
141. Joannopoulos, J.D., et al., *Photonic crystals: molding the flow of light*. 2011: Princeton university press.
142. Gan, X., et al., *Strong Enhancement of Light–Matter Interaction in Graphene Coupled to a Photonic Crystal Nanocavity.* Nano Letters, 2012. **12**(11): p. 5626-5631.
143. Wu, S., et al., *Monolayer semiconductor nanocavity lasers with ultralow thresholds.* Nature, 2015. **520**(7545): p. 69-72.
144. Hu, S. and S.M. Weiss, *Design of Photonic Crystal Cavities for Extreme Light Concentration.* ACS Photonics, 2016. **3**(9): p. 1647-1653.
145. Rybin, M.V., et al., *Fano Resonance between Mie and Bragg Scattering in Photonic Crystals.* Physical Review Letters, 2009. **103**(2): p. 023901.
146. Zhou, W., et al., *Progress in 2D photonic crystal Fano resonance photonics.* Progress in Quantum Electronics, 2014. **38**(1): p. 1-74.
147. Luk'yanchuk, B., et al., *The Fano resonance in plasmonic nanostructures and metamaterials.* Nat Mater, 2010. **9**(9): p. 707-715.
148. Zheng, M., et al., *Structure-Based Carbon Nanotube Sorting by Sequence-Dependent DNA Assembly.* Science, 2003. **302**(5650): p. 1545-1548.
149. Zheng, M., et al., *DNA-assisted dispersion and separation of carbon nanotubes.* Nat Mater, 2003. **2**(5): p. 338-342.
150. Harvey, J.D., et al., *A carbon nanotube reporter of microRNA hybridization events in vivo.* 2017. **1**: p. 0041.
151. Coleman, J.N., et al., *Two-Dimensional Nanosheets Produced by Liquid Exfoliation of Layered Materials.* Science, 2011. **331**(6017): p. 568-571.

152. Podzorov, V., *[pi]-Electron systems: Building molecules for a function.* Nat Mater, 2010. **9**(8): p. 616-617.
153. Moffitt, J.R., et al., *Recent Advances in Optical Tweezers.* Annual Review of Biochemistry, 2008. **77**(1): p. 205-228.
154. Novotny, L., R.X. Bian, and X.S. Xie, *Theory of Nanometric Optical Tweezers.* Physical Review Letters, 1997. **79**(4): p. 645-648.
155. Ohno, Y., et al., *Electrolyte-Gated Graphene Field-Effect Transistors for Detecting pH and Protein Adsorption.* Nano Letters, 2009. **9**(9): p. 3318-3322.
156. Chen, F., et al., *Electrochemical Gate-Controlled Charge Transport in Graphene in Ionic Liquid and Aqueous Solution.* Journal of the American Chemical Society, 2009. **131**(29): p. 9908-9909.
157. Gowtham, S., et al., *First-principles study of physisorption of nucleic acid bases on small-diameter carbon nanotubes.* Nanotechnology, 2008. **19**(12): p. 125701.
158. Johnson, R.R., A.T.C. Johnson, and M.L. Klein, *The Nature of DNA-Base–Carbon-Nanotube Interactions.* Small, 2010. **6**(1): p. 31-34.
159. Shankar, A., J. Mittal, and A. Jagota, *Binding between DNA and Carbon Nanotubes Strongly Depends upon Sequence and Chirality.* Langmuir, 2014. **30**(11): p. 3176-3183.